Hydrophobic coatings for offshore PV modules

Impact of precipitation from seawater on the protective glass

Karoline Sjøen Andersen

Thesis for the degree of Master of Science in
Material Science for Energy and Nanotechnology
60 credits

Department of Chemistry
Faculty of Mathematics and Natural Sciences

UNIVERSITY OF OSLO

May 15th, 2020

“Everything is temporary”

- Unknown

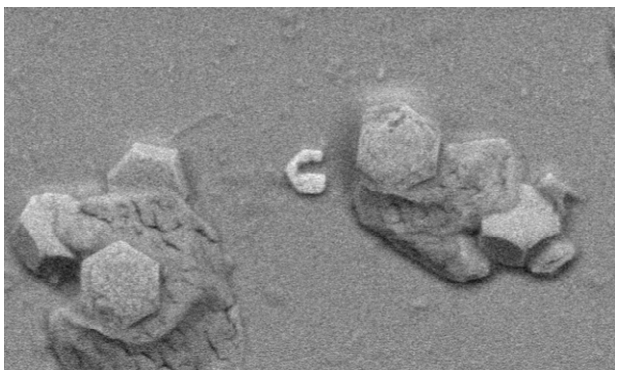

2020

Hydrophobic coatings for offshore PV modules, impact of precipitates from seawater on the protective glass

Karoline Sjøen Andersen

http://www.duo.uio.no/

Printed at: The University Print Centre (Reprosentralen), University of Oslo

Abstract

Photovoltaic panels (PV) are commonly inhibited from reaching a higher efficiency by shading, caused by dust particles covering the PV panels' surfaces. When placing PV panels offshore, the greatest source of contamination will instead be seawater precipitates which may lead to a similar shading effect. The present study aimed to contribute to the development of solar-driven, low maintenance, offshore fish pens through obtaining a transparent and self-cleaning coating for the glass surfaces protecting the panels to reach higher operating efficiency.

This is attempted through hydrophobic coatings obtained using roughened and non-roughened glass substrates coated with Trichloro(*1H,1H,2H,2H*-perfluorooctyl)silane (TCPFOS) or Octadecafluorodecahydronapthalene (ODFDHN) by evaporation, spin coating or by casting knife. Characterization was mainly done through sessile drop contact angle measurements by an optical tensiometer and transmission measurements through a spectrophotometer.

Independent of coating material and method, the surfaces are hydrophobic with contact angles in the range of 100-110° and 93-108° with seawater and de-ionized water, respectively. Unpolished samples generally have slightly higher contact angles than the roughened, and there is no distinct trend between the two coating materials. None of the materials or roughening methods cause more than a 1.5% decrease in the transmission in the range of 400-1100 nm. The study shows that a range of soluble compounds still precipitates from seawater on the hydrophobic surfaces depending on temperature, RH, and presence of dissolved organic matter (DOM). By interacting with the incoming irradiation through several mechanisms, the precipitates decrease the transmission by up to 30% throughout the range 400-1100 nm. The only insoluble compounds present after thoroughly rinsing the surfaces with de-ionized water are $CaSO_4$ in the form of dihydrate and α-hemihydrate, and organic deposits, all in amounts and sizes invisible to the eye.

Transparent and hydrophobic surfaces on glass substrates are achieved by all methods investigated in this study, using TCPFOS and ODFDHN. However, seawater precipitates still adhere to the surfaces, causing substantial transmission losses. New knowledge of precipitations from saltwater is obtained and is of use for further investigation of the problem and new solutions. Future work should include the investigation of superhydrophobic surfaces for this purpose.

Preface

This thesis is a compulsory part of the MENA master program and the result of work done at the research group FASE, at the Department of Chemistry at the University of Oslo. The thesis is written in collaboration with UNITECH Energy Group AS and linked to the company's development project Salmo Solar. I would like to thank my supervisors Profs. Truls Norby and Sabrina Satori, Drs. Athanasios Chatzitakis, and Tony Oosterkamp for all the help they have provided during the work with this thesis. I would also like to thank owner Bernt Hellesøe and CEO Gunnar Birkeland a lot for welcoming me to write my thesis at UNITECH's office in Haugesund. Being a part of UNITECH's team for two years, I have been given the opportunity to gain huge amounts of experience and considerable extension of my network. Thank you for believing in me and for throwing me into deep water, making sure I managed to swim properly and grow as a person. All help with mechanics and kind support from Rune Strandenes at the facilities at Eldøyane are also much appreciated. Thanks to PhD. Henrik H. Sønsteby for doing the AFM measurements and to Vardafjell High School for letting me use their chemistry lab for salinity experiments. Thank you, Young-Ae for letting me stay in your room at Kringsjå any time I was in Oslo a few days for mandatory lectures or exams. Also, big thanks to Erik Skaar and Ulrikke Sofie Vestad for arranging a room for me at Blindern Studenterhjem when I needed a place to stay in the exam periods. Thank you so much, Magnus Andreassen, for helping me out with small tasks in Oslo that were crucial for my planning and progress. I'm also very grateful for your assistance, social company, and creative ideas and solutions at the lab this spring. Thank you! At last, I would like to thank my beloved man Jørgen Grønhaug and best friends I'Danely Rae Guasa Svee and Charlotte Sørenes for always supporting me and encouraging me to reach my full potential. For sticking with me through the demanding process of writing this thesis and making sure my life consisted of more than just studies and work. For my mom, Ruth Sjøen for at an early age teaching me how to work with a structured and goal-focused approach. And for my dad, Henning Flæte Andersen for showing me that following your heart is always an option. Also, big thanks to all others not mentioned by name who have cheered on me along the way!

Karoline St

May 15th, 2020

Table of Contents

1. Abbreviations

AFM	Atomic force microscopy
DOC	Dissolved organic carbon
DOM	Dissolved organic matter
DOP	Dissolved organic phosphate
EDS	Energy dispersive x-ray spectroscopy
et al.	et alia, et alii, et aliae
ODFDHN	Octadecafluorodecahydronapthalene
PV	Photovoltaic
RH	Relative humidity
SEM	Scanning electron microscope
HS	Significant wave height
TCPFOS	Trichloro(1H,1H,2H,2H-fluoroocto)silane
UV	Ultraviolet
UiO	University of Oslo
wt%	Weight percent
XRD	X-ray powder diffraction

2. Introduction

2.1 Background

An increasing number of research and development studies within both academia and industry address the global climate change and FNs sustainability goals [1]. The use of solar energy has greatly increased in the last two decades, in line with research on materials for more efficient performance. The solar radiation reaching the Earth's surface in one minute is approximately equal to the total global energy consumption in one year [2]. Today's commercial PV modules are demanding large surface areas and as the human population approaches 7.8 billion, solar power will, among other things, compete with the need for land for agriculture. Public debates in Norway consider whether wind-power should be developed offshore instead of onshore [3, 4], and the current study is part of a project that examines the possibility of doing the same with solar power.

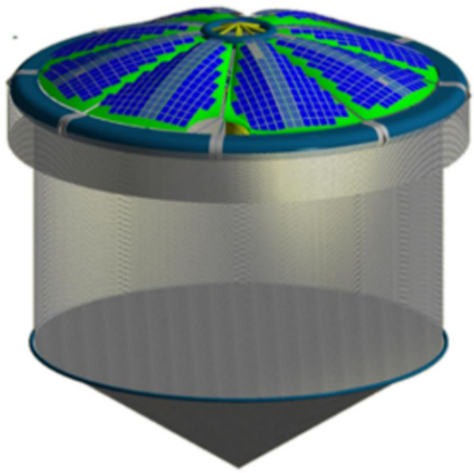

Figure 2.1: An illustration of the Salmo Solar structure, which will be floating offshore with a closed skirt below the sea surface for the fish. The structure's roof is covered with PV panels to be self-sustained with energy. The illustration is reproduced with consent from UNITECH Energy Group AS.

Salmo Solar is a research and development project UNITECH Energy Group AS have been working on since 2017. The heart of the project is a floating dome-structure covered with PV panels (Figure 2.1), firstly to make offshore aquafarms self-sustained with energy and able to operate in offshore waters without diesel aggregate or an expensive cable to shore. Secondly, the structure may also be used for energy generation to shore in rural areas, or as charging stations for

offshore machinery as floating vessels and subsea equipment. The system is designed to operate in offshore conditions, where the conditions prevailing are relentless, with a somewhat constant wind of variable strength and direction, tall waves constantly hitting the unit, rain, and strong currents. In addition to this, the structure will also be exposed to cycles of high humidity as well as droughts, to salts and possibly algae growth and bird droppings. The latter conditions will contribute to a somewhat complex surface chemistry of the PV panels over time that will affect the energy generation in one way or the other. As the structure is closed and placed under such rough conditions, manual treatment/maintenance of dome surface will be demanding and risky and is thereby undesirable.

2.2 Problems and hypotheses

As in the case of land-based photovoltaic (PV) panels, a common problem that requires major maintenance is soiling and shading due to dust particles, which directly decrease the energy generation from the panels [5], as illustrated in Figure 2.2. Partly shading can induce hotspots, which in turn can lead to short circuits, fire, and other permanent damage to the PVs [6]. In other words, shading can both inhibit the power generation and damage the PV cells and are hence to be avoided. Shading due weather phenomena such as clouds, rain, snow, and hail are somewhat unavoidable, but other sources of shading can be reduced or completely removed.

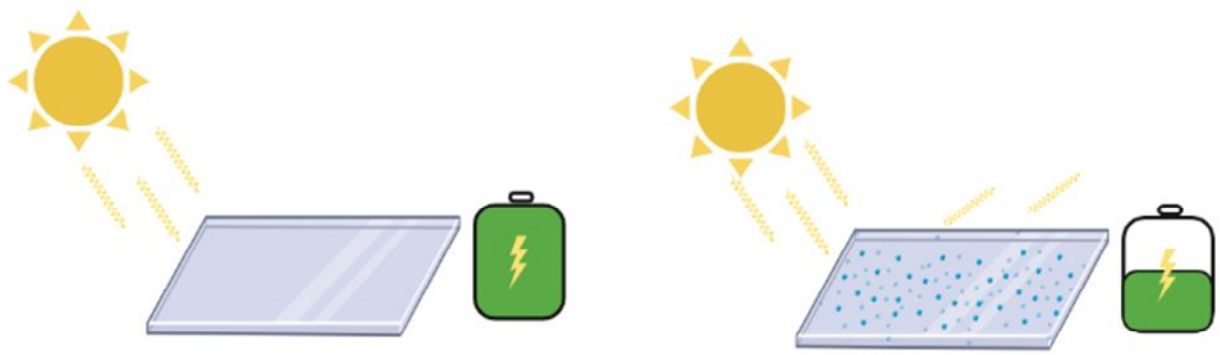

Figure 2.2: Illustration of how soiling and shading of the protective glass on PV panels decrease their energy generation and hence efficiency when operating.

Since seawater consists of approximately 3.5% salts [7], one obvious contamination and a possible source of shading considered in this work is seawater precipitates. Salt deposits on windows after a storm are a common view in coastal areas, which makes it highly likely to become an issue for offshore installations as well. How quick salt deposits form on a surface is mostly determined by the evaporation rate of water, hence the weather conditions, for instance wind speed and direction, relative humidity (RH). What happens when a wave smoothly splashes over a glass surface? One might observe spots with concentrated salt deposits or a uniform layer of salt. The latter may function as a form of filter, in terms of causing a uniform transmission loss throughout the radiation spectra. In the case of spots, they may cause total shading of bigger areas and thus lead to short circuits. Salt crystals are however somewhat transparent and might not lead to a direct shading effect, but more of a scattering effect. What kind of effect will that have on the energy generation? Does salt absorb wavelengths in the same spectrum as the PV panels, and thereby function as a "thief" of radiation? As salts are ionic compounds, and thus have different refracting indexes, scattering and/or reflecting effects are to be expected. Further investigations need to be done to study if these effects will be favorable or not for the energy generation.

Since salts tend to dissolve, a scenario of deposits being dissolved by rain and/or seawater and re-deposited should be considered. Due to different solubility products, one may obtain a buildup of some compounds over time. One might be able to dissolve some of the compounds hardly soluble in water, by acid; however, it might damage a potential coating or contribute to an increase in other deposits. The environmental impact of rinsing with acid must also be considered, as well as the cost and logistics of supplying an storing such chemicals offshore. Seawater usually contains a handful of different ions, who all have unique characteristics. In other words, "salts" are only an overall issue that might break down to one or two ions/compounds being the source of the dominant shading effect. An example is Mg^{2+} if $Mg(OH)_2$ proves to be the dominant compound deposited on the coated surfaces after exposure to both seawater and rinsing by rainwater.

Birds and bird droppings should also be considered as potential causes of shading [8]. Depending on the location and local conditions, this may be a smaller or bigger issue. Relatively simple measures can be taken to make sure birds do not sit at the surface, but bird-droppings is somewhat harder to prevent. The main constituents of bird feces are urea, ammonium, uric acid and urates, where the uric acid and mostly urates are hardly soluble in water at ambient

temperatures and may hence stick to the surface of the PV panels protective glass and cause a long-term shading effect [9].

Algae might also cause shading if the conditions allow them to grow on the glass surface in the first place. Algae need nutrients, light, and moisture to do photosynthesis and survive, as they consist of 70-90% water [10]. Depending on the site-specific conditions, the surface will be exposed to different types of algae spores through seawater splashes and possibly also raindrops. Humid conditions are necessary for the algae to survive on the surface, and depending on growth rate and weather conditions, the algal population will die, remain constant, or expand. As neither algae nor bird droppings as of today are reported as common problems offshore, the contamination source of seawater will be in focus.

Another question is how water itself will affect energy generation in terms of shading, both as rain droplets and seawater waves and/or splashes. It can arguably be considered a source of shading, as it covers the surface. Water is, as salt, transparent, so it probably will not give a 100% shading effect, but some. Furthermore, water has a refractive index that may be favorable for energy generation at certain points of the day. Depending on whether it is rain- or seawater, it will contain organic and/or inorganic components which may react on the surface by either help dissolving deposits or by transforming them into other compounds.

A mechanical washing system is a possible solution to the listed issues and it is being used in some solar parks onshore today [11]. However, such a solution would require energy to produce fresh water offshore as well as for a pumping system, and mechanical maintenance from time to time. Commercial detergents also tend to contain substances harmful for ecosystems like corals [12, 13] and should be avoided. Passive cleaning agents (coating) are thus considered the best possible solution, as they do not need continuous maintenance, and are applied before structure assembly. The glass surface coating must be transparent, to ensure transmittance and optimal PV energy generation. It should also withstand the harsh conditions offshore and have a high durability/lifetime.

So-called self-cleaning surfaces are available on the market today. The surfaces are coated with either a hydrophilic, hydrophobic, and/or photocatalytic material. Hydrophilic surfaces make the water spread out on the surface as a thin film, while hydrophobic surfaces prevent this from happening by increasing the contact angle, with the drops getting a smaller contact surface and

hence roll off more easily. The most common material used for self-cleaning today is TiO_2 which in some forms have both photocatalytic and hydrophobic properties [14-16]. The photocatalytic effect works fairly well on organic contaminants, using energy from UV-light to split molecular bonds until the organic molecules are easily washed away by the rain or disappear upon evaporation [17]. TiO_2 could in other words be suitable for handling both algae and partly bird droppings. The method is however not fully capable of handling the inorganic salt deposits, as they cannot be broken down to feasible molecules in the same manner. In addition, hydrophilic surfaces may cause enhanced salt precipitation as they spread the water out, and thus accelerate water evaporation. Oppositely, hydrophobic surfaces may prevent deposits from forming in the first place, by repelling the water before it evaporates and compounds precipitate.

Developing a coating that can withstand both organic and inorganic contamination will have positive both economic and environmental positive consequences. The latter, in terms of increased renewable energy generation both on- and offshore. Money otherwise spent on maintenance and manual cleaning will also be spared, as well as savings in terms of an increased efficiency and lifetime of the PV-system. Such a coating could be useful for other applications as well, such as self-cleaning windows for buildings in coastal areas, and windows on floating vessels. It may also exert the same abilities when applied on substrates other than glass and may hence also be used as a corrosive inhibitor on metal in coastal areas.

2.3 Aim and scope of study

The aim and main objective of this study are to obtain a hydrophobic self-cleaning coating for glass surfaces which inhibits both organic and inorganic contaminants from forming. Such a coating will highly contribute to the vision of developing low maintenance offshore fish pens powered by PV-panels. More specifically, the surface coating should at a minimum satisfy the requirements listed below, the coating being:

- Transparent, hence lead to a minimum decrease in transmission
- Hydrophobic, with a contact angle of more than 90° with water
- Self-cleaning in humid and saline conditions
- Non-harmful to the environment

- Highly durable, especially under marine conditions

The present study takes as a starting point the methodology described by Maharjan et al. [18], who proposed an easy and effective method for coating glass with a hydrophobic self-cleaning nano-coating that withstand saline exposure using TCPFOS. Coating with ODFDHN will be done to compare and to understand the differences in surface energy and the resulting hydrophobicity and transparency using different methods and coating materials. ODFDHN is a fluorocarbon that is commonly used in medicine due to its hydrophobicity and immiscibility with aqueous solutions which makes it easy to recycle and reoxygenate [19].

There are several sub-objectives listed below, which will all contribute in achieving the main objective and vision by increasing the knowledge and understanding of different areas:

- Understand the effect of temperature and RH in the coating process
- Understand the correlation between roughening the surface and measured contact angles
- Identify the critical elements in a successful coating process
- Identify common seawater precipitates, both soluble and insoluble
- Understand in which manner precipitation occurs on hydrophobic surfaces relative to hydrophilic surfaces
- Understand key factors and mechanisms for precipitation of insoluble compounds from seawater
- Conclude whether the method giving hydrophobic and transparent coatings are scalable for industrial applications

The main problem investigated is seawater precipitates soiling and shading the surface of PV-panels and hence negatively affecting the energy generation and hence efficiency. No commercial solution is available for inorganic contaminants, as the solutions are commonly based on photocatalytic decomposition of organic contaminants. Based on the hypotheses that photocatalysis does not cope with inorganic deposits, and hydrophilicity increases the evaporation rate and enhances the precipitation from seawater, focus in this study will be on hydrophobic coatings. The main hypothesis is that a hydrophobic coating can decrease the formation of seawater precipitates by simply repelling the water, making it roll off the tilted surface before precipitation occurs.

To obtain a coating giving the best results, different materials, surface roughening- and coating methods will be investigated and compared to each other. As hydrophobicity is the main effect considered in the thesis, contact angle measurements of water and seawater will be important to characterize the coatings. Transmission measurements will be done to investigate the transmission loss caused by the coating and/or sample roughening, but also losses due to possible seawater deposits on the surfaces after exposure. To identify and get a better understanding of the precipitates, EDS analyses will be performed. Figure 2.3 illustrates the practical workflow of the study.

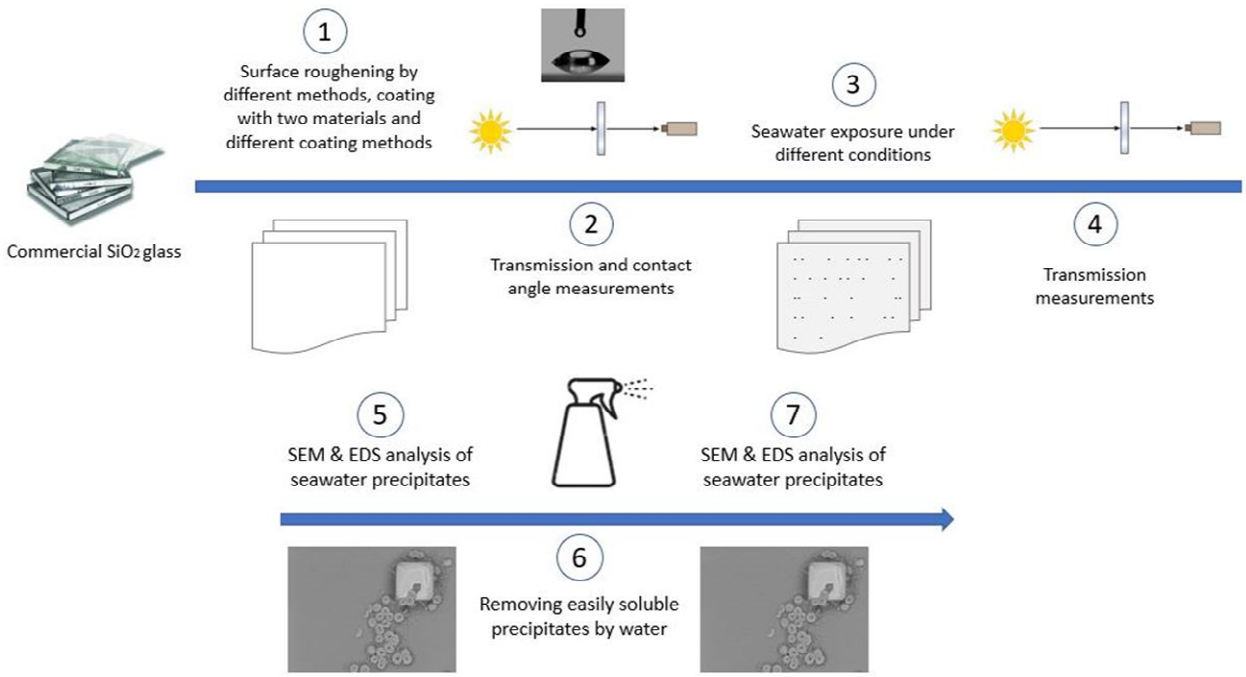

Figure 2.3: A graphical overview of the workflow intended in this study.

3. Theory and literature

3.1 Basic principles of photovoltaic cells and shading

A detailed explanation of the function of a PV cell is beyond the scope of this thesis. Here, only the general principles will be outlined. A PV cell consists of a junction, often of negatively and positively doped semiconducting material such as silicon. Doping is done to obtain excess electrons on one side, and lack of electrons (excess of holes) on the other, creating a potential difference in the cell. When the cell is absorbing light with an energy similar or greater than the bandgap, electrons move from the valence band to the conduction band and thus are free to move. Connecting a circuit between the positive and negative layers will lead to free electrons from the negative to the positive side to neutralize the potential difference. Moving electrons are synonymous with electrical current, which is considered the most convenient and versatile form of energy. Figure 3.1 presents the main components of a PV cell system and how they relate to one another.

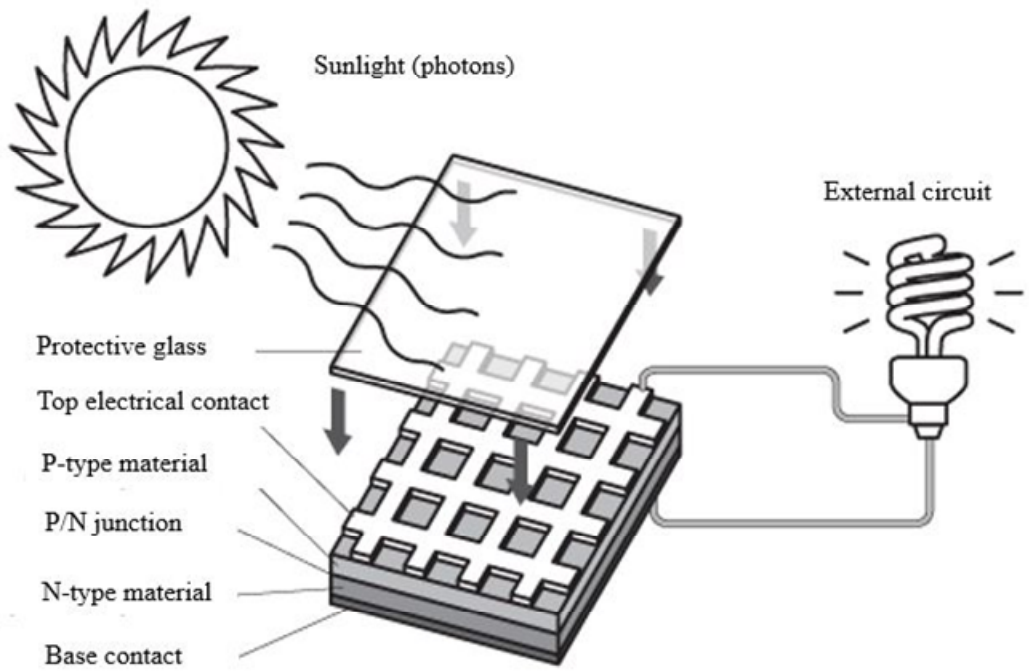

Figure 3.1: A sketch of a simplified photovoltaic cell system and its components, adapted from [20].

The generation of electricity is dependent on the quantity and quality of incoming radiation, in terms of angle and wavelength. Doped silicon is widely used to create photovoltaic cells and has a bandgap of 1.11 eV in the temperature range of 0-300K [21], which is equivalent to the energy of radiation with wavelength of 1117nm. In other words, light with this amount of energy or more can excite electrons to the conduction band and thereby induce a current. Radiation with wavelengths as mentioned is in the infrared part of the electromagnetic spectra, which in theory means all visible light and UV-radiation contain enough energy to generate power in a silicon PV cell. However, very short waves contain enough energy to excite the electrons not only to the conduction but further, making them unavailable for conduction. Thus, PV panels utilize only a small fraction of the UV-radiation reaching them. As described above, incoming radiation directly affects electricity generation. Shading and soiling will decrease incoming radiation due to scattering and absorption and thus cause a decrease in electricity generation [22].

Soiling is a common problem, especially in dry areas like the Sahara desert where sand easily adheres to the panels and builds up due to lack of rain [5]. Soiling effect refers to particulate contamination of the optical surface, which has a significant deteriorating impact on energy yield due to absorption and scattering losses of the incident light [23]. Figure 3.2 illustrates the mechanisms of scattering and absorption as well as other mechanisms that may occur when incident light reaches a surface or a particle.

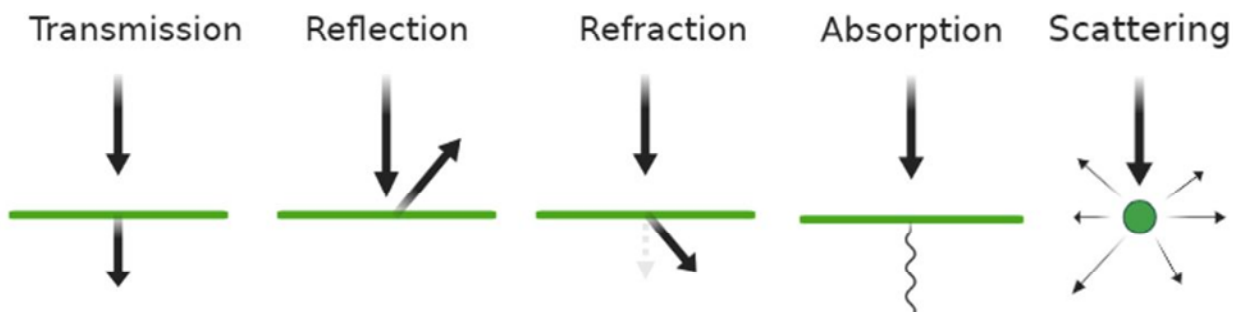

Figure 3.2: Illustration of different mechanisms that may occur when incident light reaches a surface or a particle. From the left: transmission, reflection, refraction, absorption and scattering.

Shading will be a direct effect of the soiling. When shaded, the specific PV cell is forced into reversed bias as the energy from the other cells is dissipated as heat in the shaded one. This

phenomenon can induce hotspots which can lead to short circuits, fire, and permanent damage to the PV-panel [5]. The PV-cells in a PV-panel are connected in series on the back, which means if one cell is shaded, it will dramatically decrease the output of the panel as a whole. To effectively decrease losses caused by this phenomenon, bypass diodes are used to section the panels [6].

High RH promotes the adhesion of dust and the formation of sticky dust layers on the surfaces of PV-modules. High RH also causes more absorption of solar radiation by the enhanced concentration of water vapor in the atmosphere [23]. A study performed in Indonesia 2016 reported a substantial decrease in PV output at rainy and cloudy days with high RH, however without identifying the responsible mechanism being less irradiation or accumulated dust due to high RH [24]. Locations near the ocean often have dense fogs in the morning, reducing the direct normal irradiance (DNI) significantly. High RH may also cause biological growth on the surface. It is commonly observed that wind speed and RH correlate: high windspeed decreases the RH as the wind sweeps away H_2O molecules from the air and hence allowing more molecules to dissipate into the air [23].

3.2 Seawater

Seawater precipitates are expected to have the same, direct inhibiting effect on the power generation as sand and other dust particles. Most precipitates have an inorganic nature which make them hard to decompose. However, salt precipitates have an ionic nature and thus have a variable solubility in water.

Seawater is considered a well-mixed liquid in steady-state and contains about 3.5 wt.% dissolved salts. However, surface water (<100 m) may have elevated or depressed salinity in areas with much evaporation or precipitation, respectively. Na^+ and Cl^- are the dominating ions present in seawater in terms of concentration, followed by a range of other ions [7]. Table 1 gives an overview of common ions present in seawater as mol/kg and relative to the concentration of Cl^- ions. Dissolved organic carbon (DOC) is also present in seawater and greatly varies with spatial distribution. The concentration is highest in surface waters with an average concentration of 60-90 µM, and declines with depth to an average 35-45 µM in deep waters (>1000 m) [25, 26].

Through the marine phosphorous cycle, phosphonate and phosphite are produced by plankton communities in vast quantities both in shallow and deep waters. Phosphate is thus present in seawater as, among other forms, oxidized bioavailable (+5) phosphate compounds and may also participate in precipitation processes [27]. Dissolved organic phosphate (DOP) has an average concentration of 0.1-0.4 µM in surface waters and 0.02-0.15 µM in deep waters, hence small compared to DOC but still enough to play a significant role in some precipitation processes [26-28].

Table 1: An overview of the principal constituents of seawater, adapted from [7].

Principal constituents of seawater		
ion	mol/kg	relative concentration*
Cl^-	0.5405	1.00
Na^+	0.4645	0.8593
Mg^{2+}	0.0526	0.0974
SO_4^{2-}	0.0279	0.0517
Ca^{2+}	0.01022	0.0189
K^+	0.01011	0.0187
CO_3^{2-}	0.0023	0.0043
Br^-	0.00083	0.00154
B^{3+}	0.00041	0.00075
Sr^{2+}	0.00009	0.000165
F^-	0.00007	0.00125
*The relative concentration provides the number of ions of each constituent compared to the number of chloride ions.		

The order of precipitation from seawater is dependent on the solubility of the compounds, thus the one with the lowest solubility precipitates first. However, the order of precipitation is also highly dependent on the concentrations of the different ions present in the seawater as well as factors like RH, temperature, and pH among others [29]. As an example, the solubility of gypsum and gypsum anhydrite in water increases with increasing concentration of sodium chloride in solution [30].

Some seawater precipitates are highly soluble in water, others are semi-soluble, and some are practically insoluble. Table 2 shows the solubility of a range of compounds that may precipitate from seawater under various conditions. Most salts exhibit increased solubility with increased temperature, with exceptions that exhibit retrograde solubility like $CaSO_4$ and $Ca(OH)_2$. Several of the compounds precipitate from seawater are in the form of hydrates, which over time dry to become anhydrates [29]. Examples of highly soluble compounds that may precipitate are NaCl, $Ca(HCO_3)_2$, $MgCl_2$ as well as the hydrates $KMgSO_4Cl{\cdot}3H_2O$ and $KMgCl_3{\cdot}6H_2O$.

Some of the spontaneously formed compounds react violently with water and are thus only present in intermediate stages. An example is CaO which occurs as an intermediate step in spontaneous reactions leading to the insoluble product $Ca(HCO_3)_2$. Reactions for CaO are listed in equations 2-5 below.

$$CaO(s) + H_2O(l) \rightarrow Ca(OH)_2 + energy \quad \text{(Eq.2)}$$

$$Ca(OH)_2\,(aq) + CO_2(g) \rightarrow CaCO_3(s) + H_2O(l) \quad \text{(Eq.3)}$$

$$CO_2(g) + H_2O(l) \rightarrow H_2CO_3(aq) \quad \text{(Eq.4)}$$

$$CaCO_3(s) + H_2CO_3(aq) \rightarrow Ca(HCO_3)_2(aq) \quad \text{(Eq.5)}$$

A practically insoluble compound that may precipitate is $CaCO_3$, with the solubility of 0.69 mg/100mL water at 25°C. Surface seawater is generally supersaturated with $CaCO_3$, but the carbonate hardly precipitates under ambient conditions. Precipitation rate highly depends on the concentration of phosphorous and dissolved organic matter present as well as pH. An increase in pH and/or removal of CO_2 from the water will speed up the precipitation process of $CaCO_3$ [31]. If dissolved organic matter (DOM) is present in the water, it will highly inhibit the precipitation process of $CaCO_3$. As $CaCO_3$ nucleus forms at the surface, it will immediately adsorb DOM which inhibits further growth. As this process is faster than the nucleation process of $CaCO_3$, precipitates of $CaCO_3$ are rarely observed from DOM-rich solutions except in small quantities related to aggregates of organic deposits [28].

Table 2: An overview of some compounds that may precipitate from seawater under different conditions and their solubility and synonym. Adapted from[29, 32-34].

Compound	**Solubility at 25°C (g/100mL)**	**Synonym**
$CaSO_4$	0.205	Gypsum anhydrite
$CaSO_4 \cdot 2H_2O$	0.205	Gypsum
$CaSO_4 \cdot ½\ H_2O$	0.205	Gypsum hemihydrate
$CaCO_3$	0.00066	Calcium carbonate
$Ca(OH)_2$	0.160	Calcium hydroxide
K_2CO_3	111	Potash
$Na_2SO_4 \cdot CaSO_4$	11.87	Glauberite
$KMgSO_4Cl \cdot 3H_2O$	(soluble)	Kainite
$MgSO_4$	35.1	Magnesium sulfate
$MgSO_4 \cdot 7H_2O$	113	Epsomite
$MgSO_4 \cdot H_2O$	35.7	Kieserite
$Mg(OH)_2$	0.00069	Brucite
$MgCO_3$	0.18	Magnesite
$MgCO_3 \cdot 5H_2O$	0.38	Lansfordite
$MgCl_2 \cdot 6H_2O$	56.0	Bischofite
NaCl	36.0	Halite
$NaHCO_3$	10.3	Thermocalite
$SrSO_4$	0.0135	Celestine
$SrCO_3$	0.00034	Strontianite

Since sodium and chlorine ions are the main inorganic components in seawater, the phase diagram of NaCl and H_2O gives an idea of when seawater precipitation occurs. As seen in the phase diagrams given in Figures 3.3 and 3.4, neither NaCl nor $CaCl_2$ precipitate before reaching a concentration of at least 30 wt.%, which is substantially higher than what is present in seawater. Hence, precipitation occurs only after sufficient evaporation.

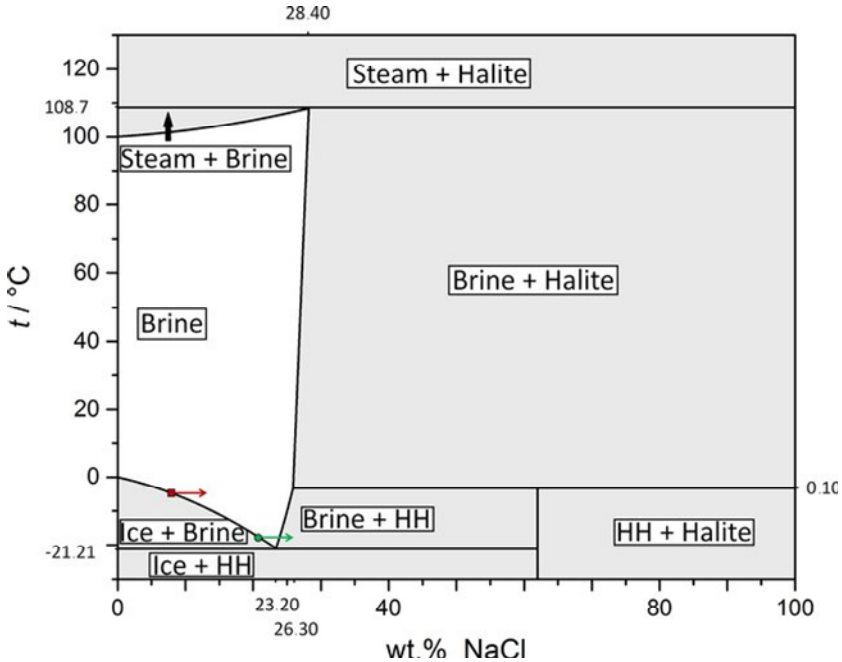

Figure 3.3: Phase diagram of NaCl and H_2O. Reproduced from [35].

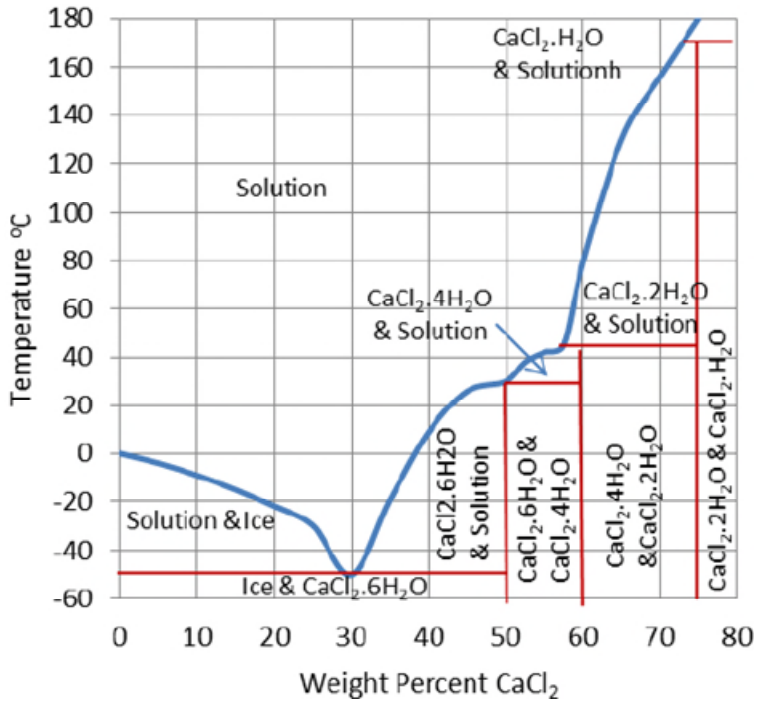

Figure 3.4: Phase diagram of $CaCl_2$ and water, reproduced with consent from [36].

3.3 Surface tension, wetting, photocatalysis, and evaporation

A material's surface energy highly results from the energy difference between bulk- and surface atoms [37]. Atoms in bulk will experience a lower energy state as they are surrounded by atoms on all sides, hence maximizes the number of bonds and lower the overall energy. Surface atoms are "missing" some surrounding atoms and are thus looking for something which can attach to it to decrease their energy [38].

Even though surface atoms have higher energy than bulk, the surface energy highly varies with material as it is a sum of the contributions from several effects. In 1962 Fowkes suggested that the overall surface tension for a given material could be represented by the sum of the intermolecular forces as given in equation 6 below [39].

$$\gamma = \gamma^d + \gamma^p + \gamma^h + \gamma^i + \gamma^{ab} + .. , \quad \text{(Eq.6)}$$

γ^d is dispersion force, γ^p is polar force, γ^h is hydrogen bonding, γ^i is induction force and γ^{ab} is the acid/base force. These are all forces dependent on the specific material, but common for all materials is contribution of dispersion forces. Hence, London dispersion forces are important contributors to a materials surface energy. London dispersion forces are given in equation 7 below, where E_{AB} is the dispersion forces between atom A and B, I_A and I_B the potential of ionization, α^A and α^B the polarization, respectively, and the R denoting the intermolecular distance [40].

$$E_{AB} \approx -\frac{3}{2}\frac{I_A I_B}{I_A + I_B}\frac{\alpha^A \alpha^B}{R^6} \quad \text{(Eq.7)}$$

A group of organic compounds with low surface energy is the fluorocarbons. This is due to fluorine's high electronegativity compared to carbon, inducing a strong dipole, and minimizing the possibilities of polarizing. Fluorocarbons are considered inert and have the lowest calculated surface energy observed. Water has very low solubility in fluorocarbons (approx. 10 ppm) and

vice versa. Fluorocarbons, in general, have a low refractive index and due to low intermolecular attractive forces, they are lipophobic, hydrophobic, and nonpolar [41-43].

A surface can either be hydrophilic or hydrophobic, depending on the contact angle of water. If it is less than 90º it is considered hydrophilic, and more than 90º it is considered hydrophobic. The contact angle increases with increasing salt content in the water, as both the solid-liquid and liquid-vapor surface tensions increase [44]. Figure 3.5 gives an overview of the characteristics of both hydrophilic and hydrophobic surfaces. Considering the extreme cases, a contact angle smaller than 5º is considered superhydrophilic and greater than 150º considered as superhydrophobic. Both extreme cases can be considered as self-cleaning surfaces with anti-fogging function [45]. Hydrophobic coatings serve as passive cleaning agents in terms of decreasing the wettability, hence making water roll off and clean the surface more efficiently. It also decreases the adhesion of dust particles to the surface [23]. Hydrophilic surfaces have high wettability abilities hence, water is spread out as a thin film. This ability is used to prevent fog and other visual disruptive phenomena. Combined with photocatalytic properties, superhydrophilic surfaces are commonly perceived as self-cleaning [14, 45, 46].

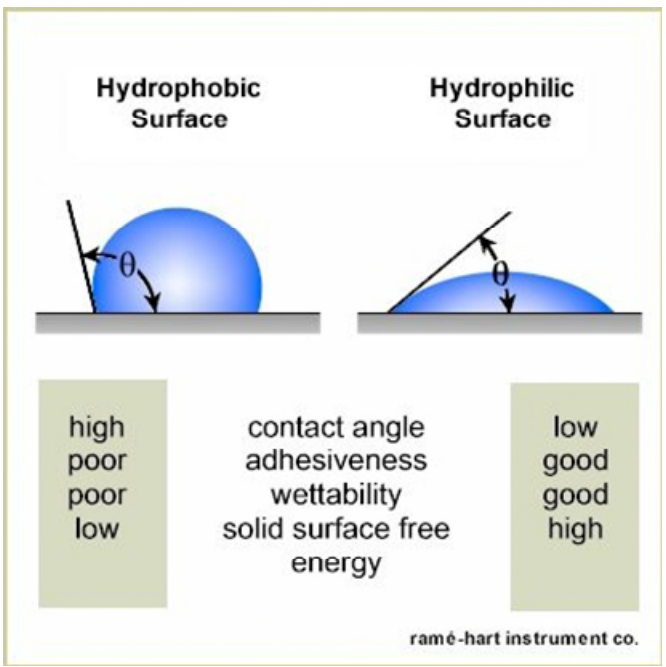

Figure 3.5: Characteristics of hydrophobic and hydrophilic surfaces, reproduced with consent from [47].

The process of evaporation the droplets undergo differs depending on the wetting abilities of the surface it is attached to. Drops on hydrophilic surfaces are self-pinned to the surface through the whole process, while it on hydrophobic surfaces undergoes two distinct stages; first a stage where the contact area is constant and the contact angle decreases, followed by a stage where the opposite situation occur [49-52]. The length of the evaporation process increases with increased contact angle and is thus longest at superhydrophobic surfaces. In 2009, Whan Chin et al. reported that at 20°C and RH of 18%, a 5 µl water droplet on a hydrophobic surface evaporated in 27.5 min while it only took 19 min (31.45% less) for it to evaporate on a hydrophilic surface [51].

If the droplet contains any dispersed solids, they will during the process of evaporation flow towards the edge of the droplet hence leaving a high concentration of deposits at the droplet's edge. This effect is independent of carrier fluid, dispersed solids in the droplet, and substrate [49]. The phenomenon is completely dominating droplets on hydrophilic surfaces, as the contact area stays constant throughout the evaporation process [53]. For hydrophobic surfaces also another phenomenon has been identified. Since the area of contact area decreases nonlinearly with time during the evaporation process, the dispersed solids will both form an inner ring-like deposit as well as tiny spots throughout the contact area [53, 54].

3.4 Recent development in the field of floating PV-modules and self-cleaning surfaces

Research and development of floating PV-technology have been a hot topic among scientists and industry the last two decades or so, which up to date has resulted in demonstrating projects and commercial operating plants in among others France, Japan, Italy, Norway, and Singapore. During this period, PV-technology has developed to become more efficient and cost-competitive compared to other both renewable and fossil energy sources (Figure 3.6). The demand for renewable energy resources and competing interests of area exploitation have also motivated further development of floating solar PV-technology [55]. However, most of today's operating floating units are in still waters; quarry lakes, hydroelectric reservoirs, irrigation ponds, retention basins, and drinking water reservoirs [56]. Still waters enable simplified and cheaper technology in terms of resistance to mechanical stress and corrosion one would have to consider in highly dynamic offshore waters. Most projects also use amorphous silicon thin-film PV panels, which

have a generally lower efficiency compared to panels made by monocrystalline silicon. However, an increased efficiency due to the cooling effect makes the difference less compared to monocrystalline PV-technology [55, 56]. The floating thin-film polycrystalline PV-technology for still waters are by some considered self-cleaning, simply as it operates in the waterline [56]. Several studies highlight the advantage of easy access to water for cleaning, meaning self-cleaning and operation in saline dynamic waters have not yet been subject of focus in these projects. One of the few commercial technologies on the market today, Hydrelio®, advertises easy access for cleaning which means they have not developed a self-cleaning solution. As of land-based PV-panels, a range of different cleaning technologies and methods have been developed [57, 58]. However, the methods require manual labor, electricity to supply drones and automatic washing systems and are thus costly both time and money-wise.

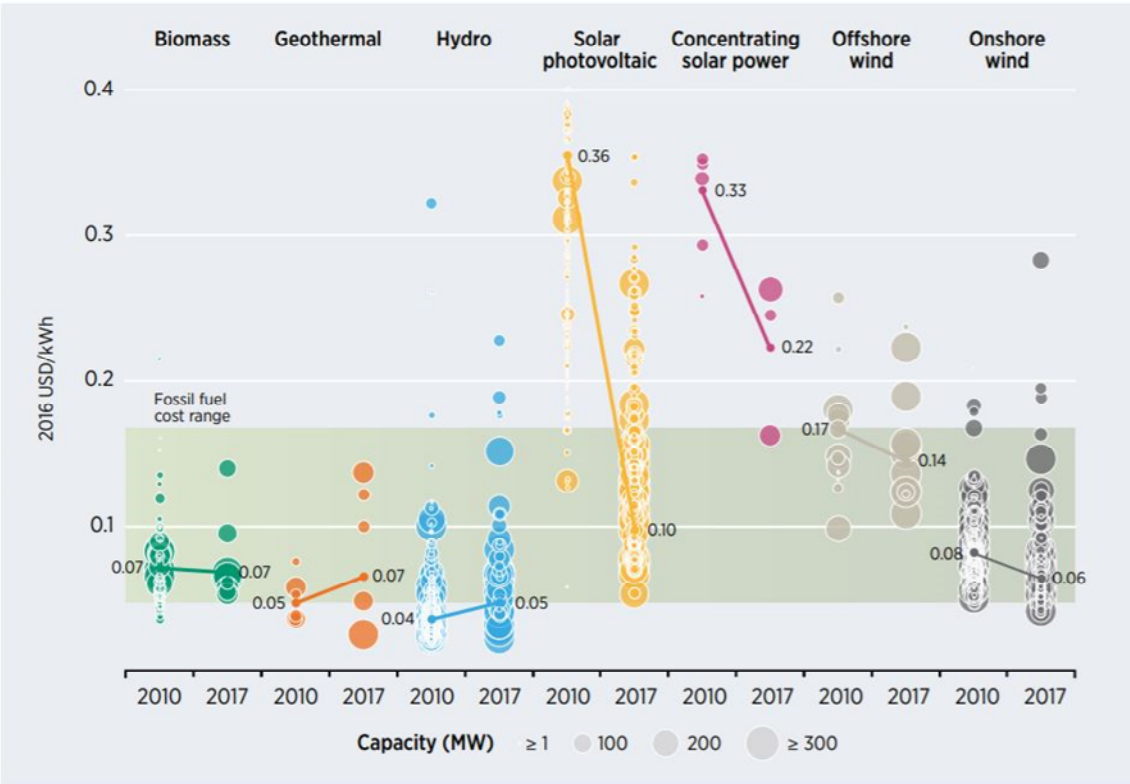

Source: IRENA Renewable Cost Database.

Note: The diameter of the circle represents the size of the project, with its centre the value for the cost of each project on the Y axis. The thick lines are the global weighted average LCOE value for plants commissioned in each year. Real weighted average cost of capital is 7.5% for OECD countries and China and 10% for the rest of the world. The band represents the fossil fuel-fired power generation cost range.

Figure 3.6: The development of global levelized cost of energy (LCOE) from utility-scale renewable power generation technologies from 2010 to 2017. Reproduced from IRENA 2017.

There is done a lot of work on self-cleaning coatings in the last two decades, especially on TiO_2 which is the most common material used in commercial self-cleaning products today [14-16, 59]. TiO_2 has two crystal forms anatase and rutile. Anatase is hydrophobic in the dark, and hydrophilic when exposed to UV-radiation. The rutile form has hydrophobic abilities. Several studies claim that doping TiO_2 by different elements (C, N, F, and others) can change the bandgap and thus make it photocatalytic under visible light as well [14, 60]. As of the photocatalytic properties of TiO_2, used in coatings it causes substantial transmission losses, increasing with shorter wavelengths (Figure 3.7) [61]. As photocatalysis is the key-effect of TiO_2-based self-cleaning commercial products, it will not cope with inorganic compounds as they are hard to decompose [62].

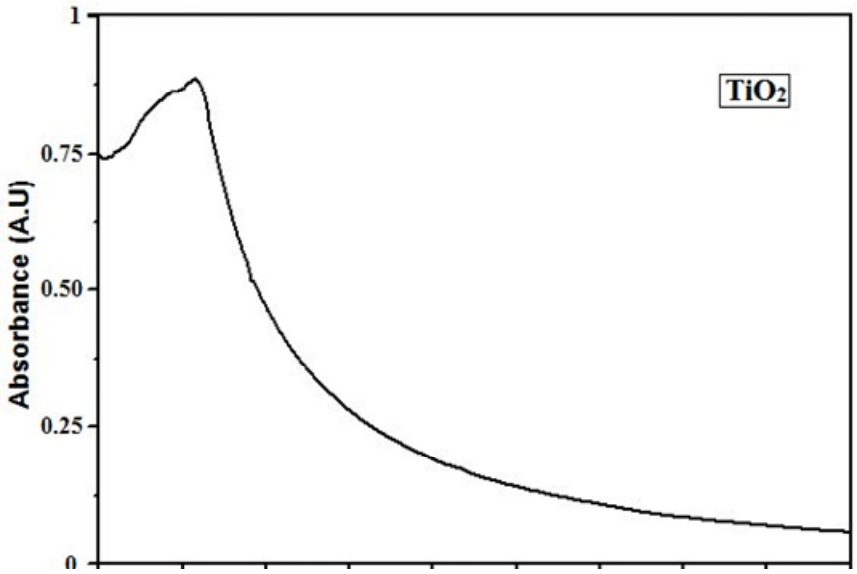

Figure 3.7: The absorption spectra for TiO_2 nanoparticles from green synthesis using hibiscus flower extract the range of 200 – 1000 nm, reproduced from [58].

Superhydrophobic coatings may also exhibit self-cleaning abilities, and can be obtained by a combination of micro and nanostructuring of the surface and lowering the surface energy of the substrate by coating with for example fluoroalkyl silanes [63]. It is also reported superhydrophobic surfaces by multi-step atmospheric pressure plasma treatment on glass substrates and by electrochemical anodization processes [64, 65].

The self-cleaning abilities of superhydrophobic surfaces do not depend entirely on the contact angle of a material, but on the adhesion of the water droplet and hence the critical tilted angle. Several authors have reported that the correlation between a high contact angle and low

critical tilted angle is not evident [63, 66]. Superhydrophobic surfaces are commonly used to protect materials like copper, aluminum, and steel against corrosion when operating in and with seawater [65, 67, 68]. However, no studies about the precipitation of seawater on such surfaces are identified.

Maharjan et al. in 2019 published an article claiming to have obtained a self-cleaning hydrophobic nano-coating for glass by coating it with TCPFOS. The coating is transparent, has a contact angle of 105° ± 1.5°, a critical tilting angle of 14° and is resistant to alkali solution, saline exposure and extreme temperature cycling (-10-60 °C) [18]. The method is divided into two main steps; roughening- and coating the surface. Roughening is done by polishing with 0.1 µm diamond suspension, making microscopic torturous grooves to enhance the adhesion of TCPFOS on the glass surface. The coating is vapor-deposited in a controlled environment with an RH of 16%. Arguing that TCPFOS through hydrolysis and condensation will stick to the glass surface by covalent bonding. The chemical reaction for the hydrolysis is given in equation 8. All reactions happen at the Si-atom, first exchanging Cl-ions with OH groups and then condensates, attaching to the glass surface by O-bindings. A scheme of the chemical process is illustrated in Figure 3.8.

$$\sim SiCl_3(l) + 3H_2O(g) \rightarrow \sim Si(OH)_3(l) + 3HCl\,(g) \qquad \text{(Eq.8)}$$

As TCPFOS has attached to the surface, the coating makes a “new” surface of perfluorocarbons which has a very stable nature due to the strong carbon-fluorine bonds and is considered inert and thus durable.

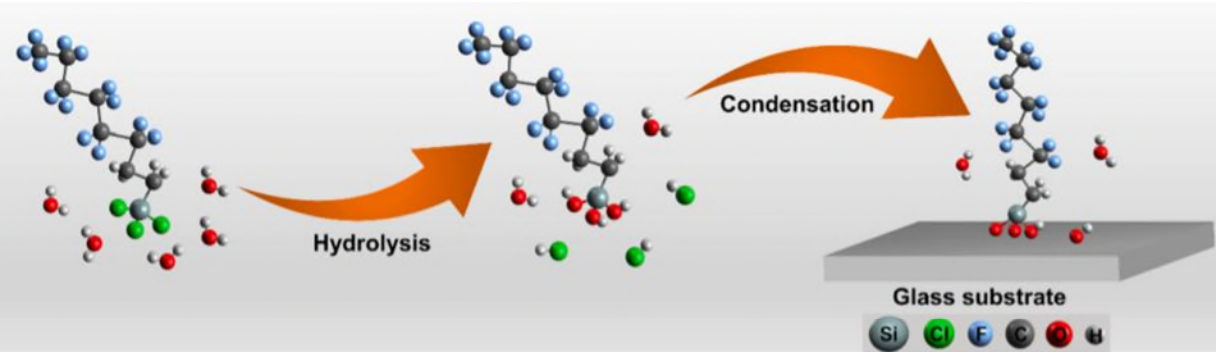

Figure 3.8: Illustration of the chemical process of coating a glass substrate with TCPFOS. Adapted from [18].

3.5 Theory of methods and equipment

3.5.1 Scanning Electron Microscopy

Scanning electron microscopy (SEM) is a piece of equipment for studying the interaction between electron and matter, using a highly energetic beam of electrons. Electron microscopes obtain a higher resolution than their counterpart optical microscopes due to the use of shorter wavelengths. Minimum separation resolvable (d_{min}) by a microscope is given by equation 9, where λ is the wavelength, and θ is the angle of outgoing wave compared to the incident direction.

$$\boldsymbol{d_{min}} = \frac{\lambda}{2sin\theta} \qquad \text{(Eq.9)}$$

Thus, the resolution may be improved by using shorter wavelengths. The wave nature of electrons is described by the De Broglie relation, given in equation 10.

$$\lambda = \frac{h}{p} = \frac{h}{\sqrt{2m_e E_k}} \qquad \text{(Eq.10)}$$

SEM is a highly popular instrument for mapping surfaces of both organic and inorganic compounds. However, prolonged exposure may cause certain organic and biological materials to be damaged, destroyed, or deformed. SEM is operated under vacuum and is thus not suitable for samples containing liquid or gas [69]. SEM is a good instrument for analyzing surface structures, as it gives a visual photo of the surface. By using contrast and shadowing, the photo can be adjusted to human vision and understanding. The basic principle is exposing the sample to a beam of electrons, which in different ways will be reflected to the detector. If the sample is non-conducting, one will achieve a buildup of electrons at the surface and everything will look the same [70]. The most common imaging mode is based on the low-energy (<50 eV) secondary electrons, ejected from the k-shell of the specimen atoms by inelastic scattering interactions [71]. A schematic illustration of an SEM is shown in Figure 3.9.

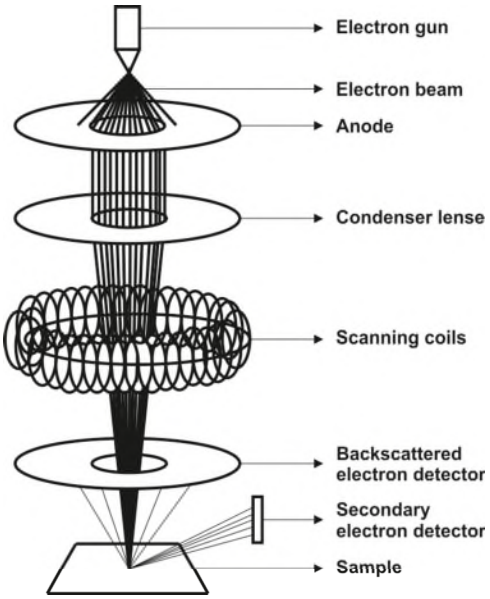

Figure 3.9: Schematic illustration of a typical SEM setup, reproduced from [71].

3.5.2 Atomic Force Microscopy

The field of atomic force microscopy (AFM) was invented by Binning, Quate, and Gerber in 1986, and has made a major impact on science and technology since then [72]. It measures attractive or repulsive forces between the sample surface and the scanning probe tip and hence maps the topography of it. All samples can be analyzed, independent of whether it is conductive or not, and the technique is very delicate and will not damage the sample in any way. Hence, AFM can be used for whatever sample and in different environments; under low temperature, in a vacuum, and in liquid. However, the technique has its drawbacks; only being able to measure height in order of micrometers, slow measurement, and limited scan area. The probe is made of silicon or silicon nitride and has a sharp tip with only a few nanometers in radius which is vulnerable to deformation. The forces are calculated by measuring the cantilever's deflection. Knowing the stiffness of the probe (k), the force (F) can be calculated using Hooke's law given in Eq.11 below where z is the distance bent from the origin [69].

$$F = -kz \qquad \text{(Eq.11)}$$

The sensitivity is dependent on the probe's size and stiffness, with a range of 1 pN – 1nN per nm. To precisely control the sample's position, it is mounted on a piezoelectric stage, and voltage is applied. To control the location of the probe relative to the sample, different methods can be used.

The most common one is using laser light that reflects on the probe's tip and onto a position-sensitive photodiode detector as shown in Figure 3.10 below. There are three main ways to operate an AFM; contact-, constant force- and tapping mode. Whereas the contact mode lets the probe follow the surface intimately and the constant force mode continuously adjusts the distance between the sample and probe to obtain a constant force and thus also a constant deflection of the probe. In tapping mode, a stiff cantilever oscillates near its resonance frequency and intermittently taps the surface, measuring the changes in resonant frequency or amplitude [69]. The latter mode is the most commonly used in ambient conditions and liquid conditions, as it offers improved lateral resolution and is the mode that causes the least damage to the sample.

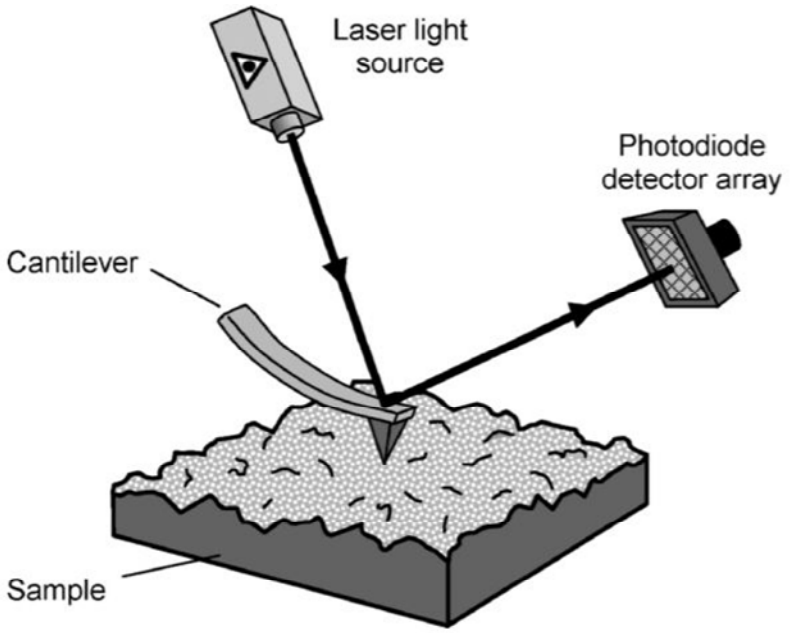

Figure 3.10: Illustration of the principle of AFM. Reproduced from [69], p.268.

3.5.3 Spectrophotometer

A spectrophotometer is an instrument measuring the attenuation of light passing through a sample. The system consists of an energy source, an energy spreader for the choice of wavelength, and an energy detector [73]. Detecting the light passing through a sample relative to a reference, one can easily obtain the transmittance and absorbance. Transmittance is given by the fraction of the relation between them are given in Eq. 12 and 13 below, T denoting transmittance, A absorbance, I_o incoming irradiation and I transmitted light:

$$T = \frac{I}{I_o} \quad \text{(Eq.12)}$$

$$A = -log_{10}(T) \quad \text{(Eq.13)}$$

3.5.4 Optical tensiometer

An optical tensiometer is used to determine different types of contact angles to get information about a surface's wetting abilities. There are different contact angles to be measured, based on three droplet scenarios: sessile drop, dynamic advancing drop, and dynamic receding drop. The latter two are measured using a tilted stage as illustrated in Figure 3.11, denoting the receding and advancing angle with r and a, respectively. A tilted stage was not available for use in this study.

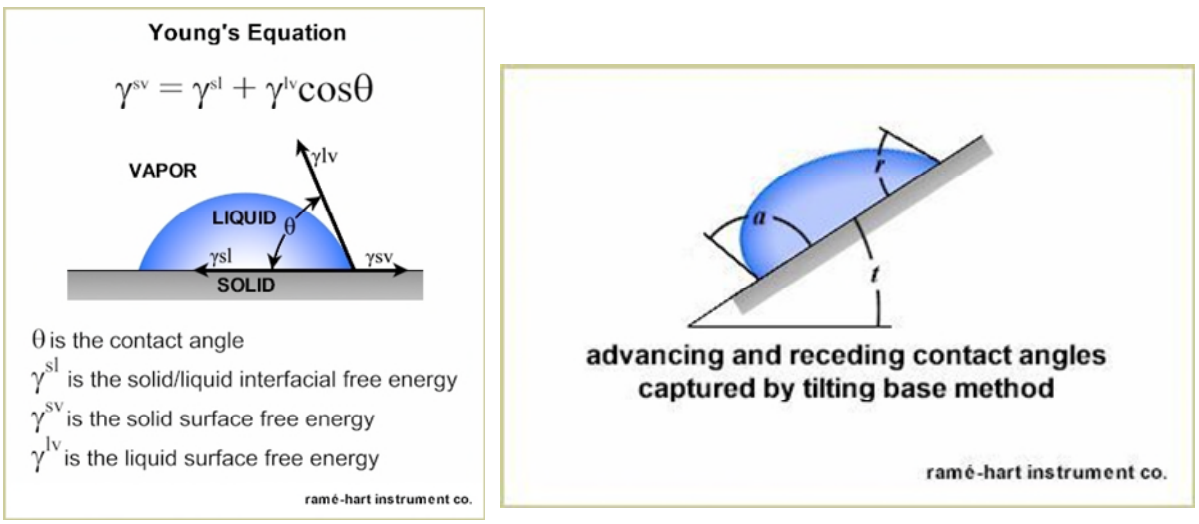

Figure 3.11: Left: Young's equation for calculating the contact angle. Right: Illustration of the scenarios of a droplet on a tilted stage, showing a maximum and minimum thermodynamic receding and advancing contact angles before it slides. Reproduced from Ramé-Hart [47].

3.5.5 Coating by casting

When coating by casting, the material is deposited on the substrate in a liquid state and evaporates to leave a thin film on the substrate. The thickness can range from a monolayer to tens of micrometers, depending on the amount of liquid deposited and the method used. A handful of casting methods are available but casting by knife and spin-coating will be the methods furtherly discussed. When coating with a casting knife, the liquid is manually spread out on the sample by

passing the knife over the surface. Most knives consist of a steel blade resting on two runners to form a precise gap between the blade and the sample which can be adjusted to obtain a specific thickness of the coating [74]. The method is very simple and time-effective but is dependent on a knife scaled for the specific sample and smooth execution and uniform exerted force to obtain a good result. A typical casting knife is illustrated in Figure 3.12.

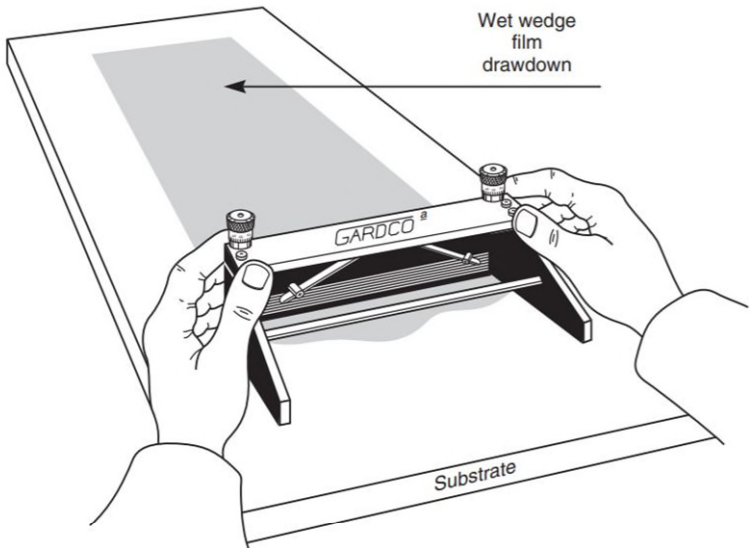

Figure 3.12: Illustration of a typical hand casting knife, reproduced from [74].

Spin-coating is a method of coating with materials in the liquid state at ambient temperature. By mounting the sample on a spinning stage by suction and placing droplets on it, the liquid will spread out evenly on the sample due to the centrifugal force. By adjusting the speed/rpm one can control the thickness and uniformity of the film/coating, provided that the solvent's viscosity is not shear dependent and does not vary across the substrate [69]. The coating process can be divided into four steps as illustrated in Figure 3.13.

1) Deposition: the liquid is placed on the surface in a small volume.
2) Spinning-up: the substrate is spun-up and the centrifugal force makes the liquid flow radially outwards.
3) Spinning-off: spinning the substrate at a constant speed to remove excess liquid. Resistance flow increases with a decrease in thickness of coating/film.
4) Evaporation: primary mechanism of solidification. To be done in a controlled environment, and often in an annealing furnace to speed up the process.

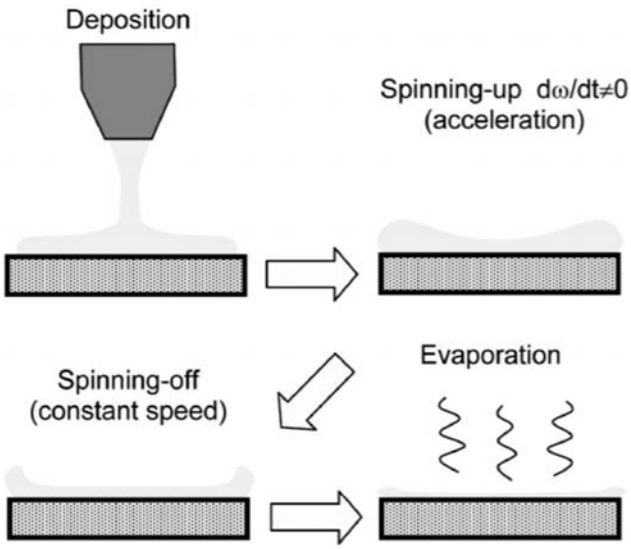

Figure 3.13: Illustration of the four steps of the coating process of spin-coating. Reproduced from [69], p.182.

3.5.6 Coating by evaporation

Coating by evaporation is a physical vapor deposition (PVD) technique with two dominating methods: thermal- and electron beam evaporation whereas only the former will be explained in more detail. The general process is generating a vapor which is then condensed as a solid film on a substrate. The process of thermal evaporation is usually done in a vacuum furnace, where the furnace heats the coating material to vapor and the high vacuum makes sure it reaches the substrate without scattering and reacting with other atoms in the chamber [69]. A general system for thermal evaporation is illustrated in Figure 3.14.

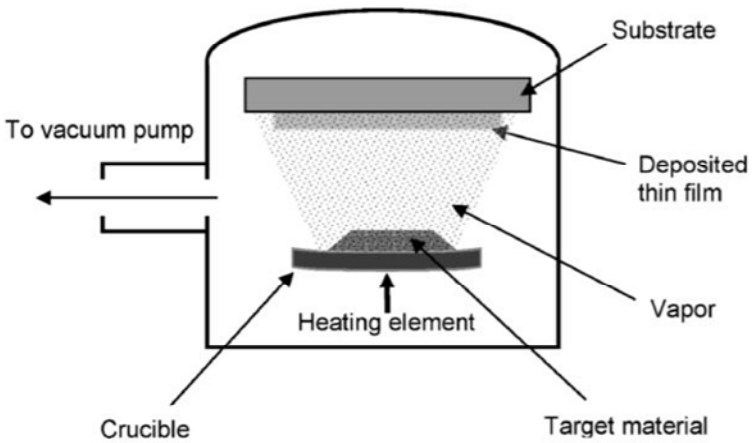

Figure 3.14: Illustration of the setup for coating by evaporation. Reproduced from [69], p.152.

4. Experimental

4.1 Chemicals, equipment, and instrumentation

4.1.1 Chemicals, consumables, and hardware

Coating chemicals; ODFDHN (≥ 94%), a mixture of cis and trans, and TCPFOS (97%) were ordered from Sigma Aldrich and used without further modifications. Commercially, untreated silicon dioxide[1], 6 mm glass in pieces of 5 x 5 cm^2 was provided from offcuts by a local glass distributor (Kalland Glass & Tre AS). The sample size was chosen considering the visibility of salt deposits, but to still be able to analyze samples with available instruments and equipment. Samples were cut manually, so small deviations in size were observed. An exact standard deviation was not calculated, as the sample size is not considered crucial for the final results. The samples could visually be divided into two different shades, one completely transparent and one with a hint of green (see Figure 4.1), even though the distributor claimed all samples were the same type of SiO_2 glass. To keep the number of variables as low as possible, each experiment/treatment was done to samples of the same shade. Dino-Lite AM7515MT8A digital microscope was used to analyze the roughening results.

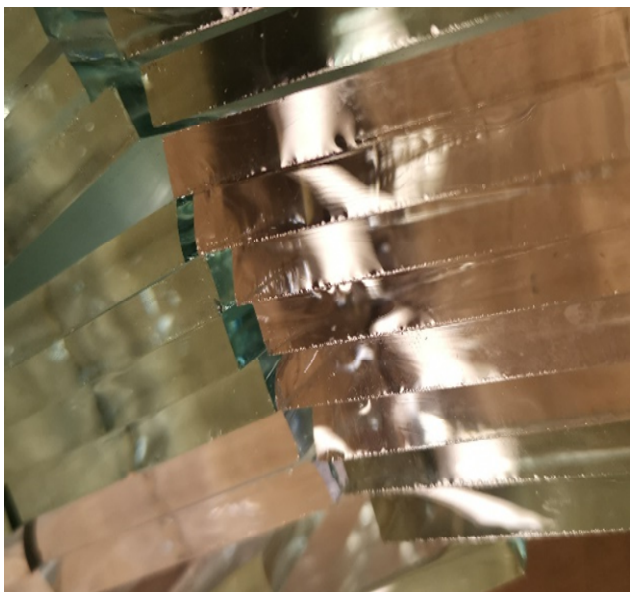

Figure 4.1: Glass samples of two slightly different tones used in the study, referred to as green and standard.

[1] Characterization and analysis done in 5.6 indicates that the glass samples with green shade indeed are lime-soda glass and not pure silicon dioxide (SiO_2) as stated from the distributor.

Hygrometers from Cotech/Clas Ohlson with a given range and uncertainty of 10-100% ± 1% for RH and -10-70°C ± 0.5°C were used for logging when coating by evaporation in the furnace, and when exposing the samples to seawater. For washing the samples, Brandon Ultrasonic cleaner 2200 with Branson general purpose cleaner concentrate was used. Seawater used in this work was gathered by hand at four different locations May 1st, 2019 (shown in Figure 4.2), and stored in plastic bottles in a semi-shaded place indoors. Samples were collected directly in clean plastic bottles that were lowered approximately 15 cm beneath the sea surface. In Bømlo, Kvalsvik, and Aksnes, the samples were collected in exposed areas in terms of waves and thus well-mixed waters. The sample collected from Karmsundet was collected in a somewhat sheltered marina.

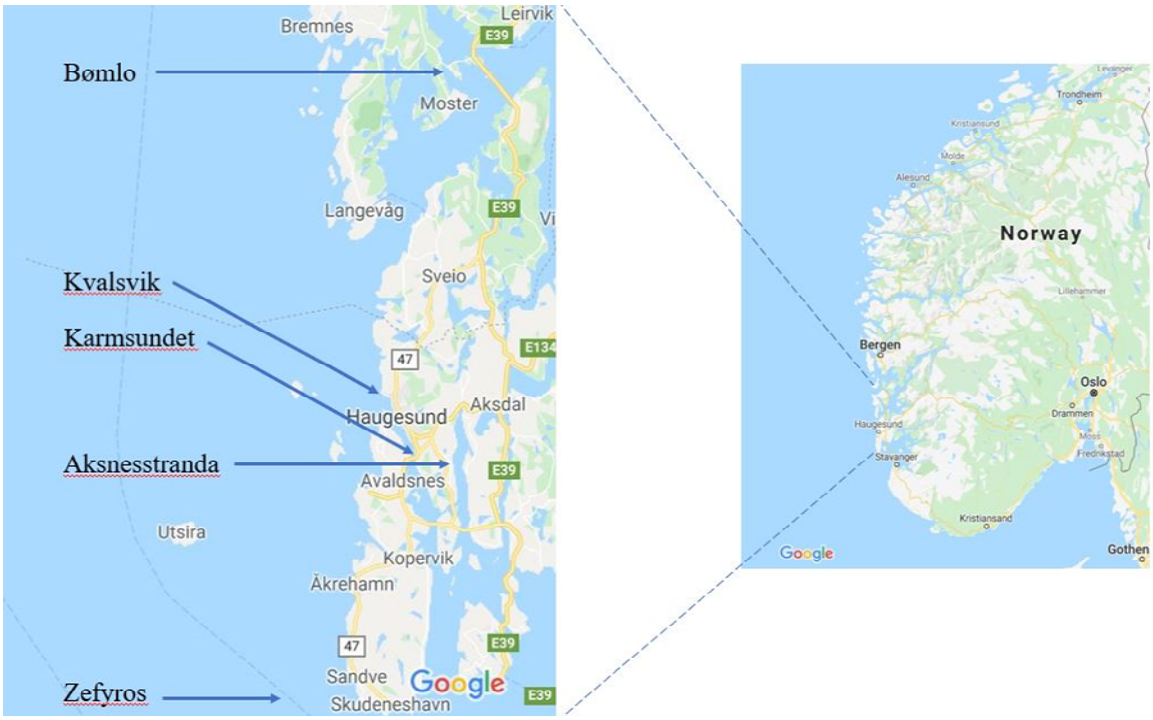

Figure 4.2: The locations of seawater collection and planned location of seawater exposure in offshore conditions (Zefyros). Snapshots from Google Maps.

De-ionized water used in this work was from a Direct-Q® 3 water purifier from Millipore with both de-ionizing and membrane cleaning. Isopropanol (99.99%) was also used for cleaning the surfaces. Aluminum oxide films (0.5, 0.3, 0.1, and 0.05 µm) and 0.1 µm diamond suspension from Struers were used for the delicate polishing methods.

4.1.2 Instrumentation

In this work, the spin coating was performed with a Laurell Spin Coater Model WS-400BZ-&NPP/LITE (REV.MS) mounted in a fume hood. The instrument was connected to a vacuum pump and pressured air (4 atm) to ensure sufficient suction to keep the sample in place and ventilation, respectively. For transmission measurements, a Specord 200 Plus 2010 edition spectrophotometer was used, measuring incoming radiation in the range of 400-1100 nm. Both instruments are shown in figure 4.3. For contact angle measurements, a Biolin Scientific Attension Theta Lite optical tensiometer with a flat horizontal, fixed stage was used. The vacuum furnace used for coating was a VACUtherm from Thermo Scientific. The insides of the furnace measured 30 x 30 x 26 cm^3, which restricted the size of both equipment and samples used when coating by evaporation in the furnace. The two initially installed trays were removed, and all equipment were installed on the bottom surface of the furnace. The furnace was connected to a vacuum pump and could heat up to 200ºC. The latter two instruments are seen in Figure 4.4. HITACHI TM3000 tabletop SEM with an EDS function was used to analyze the precipitates from seawater on the glass surfaces (Figure 4.5). It could not be used for studying the surface structure of the glass samples after roughening due to glass' lacking conductive abilities. Morphological studies (AFM) were performed using a Park Systems XE-70 AFM equipped with a standard NHCR tip. Data were analyzed using the gwyddion 2.43 spm visualization software.

Figure 4.3: Left: Laurell Spin Coater Model WS-400BZ-&NPP/LITE, right Specord 200 Plus 2010 spectrophotometer used in this work. Both images reproduced from the distributors.

Figure 4.4: Left: Biolin Scientific Attention Theta Lite optical tensiometer used for measuring contact angles in this work. Right: VACUtherm furnace from Thermo Scientific used for the coating process by evaporation. The images are reproduced from the distributors.

Figure 4.5: HITACHI TM3000 tabletop SEM used in this work. Image reproduced from the distributor.

4.2 Experimental procedures

4.2.1 Initial experiments: salinity of seawater and tuning of temperature and RH

The salinity of the collected seawater samples was measured by calculating the difference in weight from a predetermined amount of liquid seawater and the completely dry salt crystals after evaporation. The scale used for this experiment was a Mettler AM100 with 0.001 g accuracy, last calibrated in October 2010. Four plastic cups were weighed before being filled with 10 mL of water from one of the four different locations. The samples were left to evaporate on top of a shelf in ambient environments for two weeks. The plastic cups were then weighed again, and the difference was calculated along with the weight percent salt for each seawater sample.

The tuning of temperature versus RH in the VACUtherm furnace from ambient temperature was done. Three hygrometers were placed in the furnace, and both temperature and RH were noted every minute for 23 minutes until the hygrometers displayed approximately 35°C.

4.2.2 Sample preparation; washing, roughening and coating

The full sample collection was made by different combinations of coating material, roughening - and coating methods described below. A full overview of the sample series is given in Table 4, at the end of this section.

The washing procedure was similar for all samples and is therefore explained in detail once and referred to throughout the methodology section. Branson's general-purpose concentrate was mixed with one part soap and two parts tap water. Two samples were cleaned in the same 600 mL glass beaker. The beaker was put in the ultrasonic cleaner for five minutes, without using the heating option. Each sample was removed from the beaker using tweezers and rinsed thoroughly with de-ionized water followed by isopropanol. The samples were then dried one by one using a compressed air gun, before they were marked on the backside and left on the table counter with the marked side down overnight. All samples were marked by engraving three letters/numbers in a corner on the backside. F denoting fine abrasive, G, coarse abrasive and U, unpolished. Pilk 1 and 2 are samples sent by Pilkington Norway AS for reference.

All samples had their edges ground for safety reasons to avoid sharp edges. This was done partly by hand polishing on a polishing paper, and partly on an automatically rotating polishing

machine with same size polishing paper. This was done for HSE-reasons only, hence, reproductivity was not in focus. Prior to the delicate polishing, all samples were roughened with a coarse diamond abrasive to create micro/nanoscale tortuous grooves on the surface. This was done using a 5.0 µm polishing cloth on an automatically rotating polishing machine at 170 rpm. Each sample was polished for three minutes before turned 90º and polished three more minutes to get grooves in both directions. After polishing, they were washed according to the washing procedure described above.

For the delicate polishing, three different methods were used. The initial method was polishing by an automatically rotating machine with 0.1 µm diamond suspension on a synthetic velvet polishing cloth (both from Struers), 150 rpm for three minutes (as described in [18]). Due to the big sample surfaces and fluffy polishing cloth, the samples were hard to hold manually without sticking to the polishing cloth. A costume-made sample holder was made to ease the work (Figure 4.6). The second polishing method was using the 0.1 µm diamond suspension and a polishing cloth, polishing with circular motions by hand. Each sample was polished with 450 circular movements, and the application of three drops of suspension every 100 rounds. The third method was using diamond polishing paper of four different sizes, polishing by hand with the help of the sample holder (Figure 4.6). Struers' polishing papers of 0.5, 0.3, 0.1, and 0.05 µm diamonds were used. The four papers were glued to a clean glass surface by ReMount™ glue from 3M as shown in Figure 4.7. Each sample was polished for 30 seconds on each paper with random motion, starting with the roughest paper going down to the finest. After polishing, the samples were washed as described in the washing procedure.

Table 3: Overview of polished samples grouped by polishing method used.

Sample series name	Polishing method
F1, F2	Fine abrasive with diamond suspension and polishing cloth
F4, F5, F6	Fine abrasive with polishing papers
G3	Only coarse abrasive

Figure 4.6: The sample holder for polishing, which was custom-made for this study. It is made to hold the 5 x 5 cm^2 glass samples in place when polishing their surfaces.

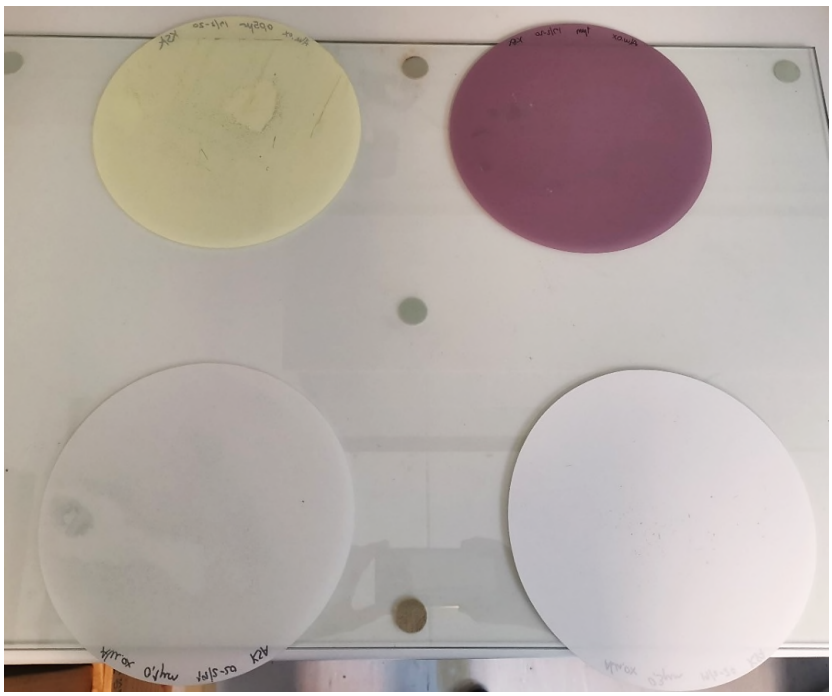

Figure 4.7: Polishing papers from Struers glued to a glass plate as described in the third polishing method. Starting in the upper right corner, going clockwise, from coarsest to finest grains.

4.2.3 Coating methods

Coating by vapor in the vacuum furnace was only done using TCPFOS as coating liquid. A sample series of three samples were coated simultaneously, set up as shown in Figure 4.8. The samples were marked by carving with L, M, or H. The sample closest to coating liquid was marked with L,

the sample furthest away from the coating liquid was marked H and the one in the middle was marked with M. The coating process was executed in the VACUtherm furnace at room temperature and three hygrometers were placed in the oven (Figure 4.8). A block of copper (3 x 7 x 7 cm^3) was used as a heat source to evaporate the coating material (TCPOS). The block was together with a petri dish heated on a hotplate for 20 minutes at 200°C before being placed into the oven. The amount of TCPFOS inserted into the petri dish was varied in the range of 0.15-0.25 mL and the furnace was closed for 20 minutes. Both temperature and RH were noted from the three hygrometers every 10 minutes.

Coating by casting knife was done for both coating materials and was executed in a fume hood. An amount of 0.25-1 mL of the coating liquid was inserted on one of the sample edges and spread as uniformly as possible with the casting knife to cover the whole surface. The samples were left to dry in the fume hood at ambient temperatures overnight. The casting knife used was cleaned thoroughly by isopropanol and left in the fume hood overnight as well.

Spin coating was done in two steps; step one rotating the sample at 500 rpm for one minute and step two rotating it at 1000 rpm for one minute. All samples had one droplet of coating liquid applied before each step and were then put in the fume hood or vacuum furnace for drying.

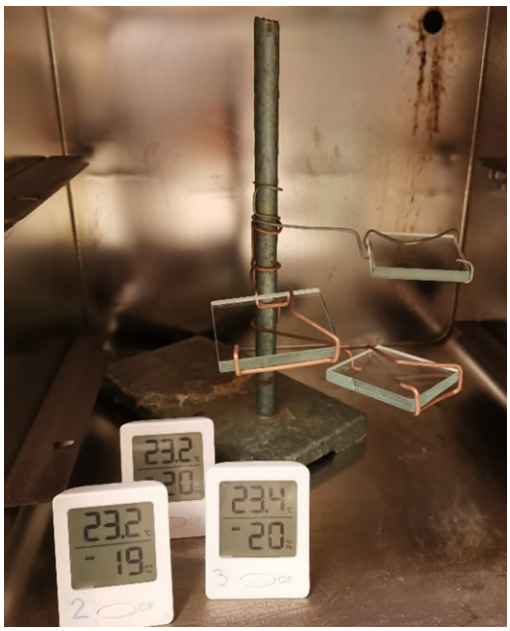

Figure 4.8: The setup in the furnace with a custom-made sample holder and three sensors showing temperature and RH. The sample at the lowest place is marked with “L”, the highest “H” and the one in-between “M”. Samples are held in place by copper wire twisted around the stand.

4.2.4 Seawater exposure setup

All samples were divided into groups of samples marked with L[2], M or H, respectively. The latter two groups were placed in separate 10 L plastic boxes from Clas Ohlson and tilted approximately 15 degrees. This was done using custom built racks from Meccano® (see Figure 4.9). Two untreated reference samples of green shade were placed in both boxes. In addition, the reference sample Pilk 2 was placed in the same box as the samples marked with "M". For the exposure-experiments seawater collected from Aksnes beach March 11th, 2020 was used. Rainwater used was collected in an open glass container from Haugesund in the period March 4th-11th 2020. The plastic boxes were placed on a countertop near a south-west facing window. Samples were exposed to seawater and rainwater four times a day, every 6 hours, for eight days. The H samples were exposed to seawater only, by splash and spray every second time. Splash refers to one teaspoon (approx. 5 mL) exerted on each sample from 5 cm vertical distance. Spray refers to the finest spray available with a household spray bottle[3] from a 20 cm vertical distance. All M samples were exposed to seawater and rainwater, every other time: rainwater spray two times a day and seawater splashes the other two. The boxes were not fully closed and had a 2 cm slip around the edge. Temperature and RH were noted after each application.

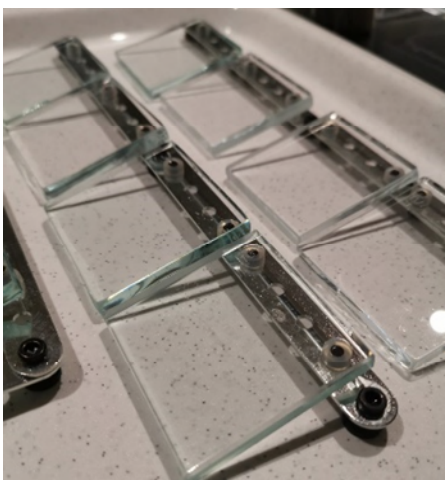

Figure 4.9: The samples placed on stages tilted approx. 15 degrees prior to seawater exposure.

[2] All L-samples and Pilk2 were glued to a metal frame that was supposed to be mounted at the floating offshore wind turbine Zefyros (see Figure 4.2). Unfortunately, they were never mounted due to the Covid-19 situation.

[3] https://www.plantasjen.no/sprayflaske-800-ml-gronn-2352216.html, spray bottle bought March 9th, 2020.

Table 4: Overview of the sample series, listing the coating material, polishing, and coating method used as well as the shade of glass substrate used.

Name	**Polishing method**	**Coating material**	**Coating method**	**Glass shade**
U1	No polishing	ODFDHN	Spin-coater	Green
U2	No polishing	TCPFOS	Spin-coater	Green
U3	No polishing	TCPFOS	Vapor coating, without a vacuum	Green
U4	No polishing	TCPFOS	Spin-coater and dried in the furnace with a vacuum	Green
U5	No polishing	ODFDHN	Casting knife	Standard
U6	No polishing	TCPFOS	Casting knife	Standard
F1	Fine abrasive with diamond suspension and polishing cloth	TCPFOS	Vapor coating, with a vacuum	Green
F2	Fine abrasive with diamond suspension and polishing cloth	ODFDHN	Casting knife	Standard
F4	Fine abrasive with polishing papers	TCPFOS	Vapor coating, without a vacuum	Standard
F5	Fine abrasive with polishing papers	TCPFOS	Spin-coater	Green
F6	Fine abrasive with polishing papers	ODFDHN	Spin-coater	Green
G3	Only coarse abrasive	TCPFOS	Vapor coating, without a vacuum	Standard
Pilk1	Pilkington **Activ™**, reference	-	-	-
Pilk2	Pilkington **Activ™** Blue, reference	-	-	-

4.3 Analysis and characterization

4.3.1 USB-microscope & AFM analysis

A reference sample (B1) along with a sample from each of the sample series G2, F1 and F4 were analyzed by USB-microscope. Four images at the same magnification at different locations for every sample were taken. In addition, two AFM measurements were done on sample F4, using tapping mode.

4.3.2 Contact angle measurements

Contact angle measurements were done on the coated surface of all samples, with both deionized water - and seawater before the exposure experiments. A custom program was chosen for this study: using sessile drop the pipette measured 2 µl water droplets before giving a signal that the droplet could be manually exerted. When exerted on the surface, measurements were done for five seconds and saved as excel-tables along with one photo per measurement. The baseline was set manually by placing a droplet on the surface before measurements to set it at the right level. As all samples had the same thickness (6 mm), the stage was only moved in x-direction during measurements. Three measurements were done per sample, spread along a horizontal line as shown in Figure 4.10.

Figure 4.10: Illustrating the locations of contact angle measurements done on the 5x5 cm^2 glass samples.

4.3.3 Transmission measurements

Transmission measurements were done prior to- and after seawater exposure, with two measurements per sample. Measurements were done in the range of 400-1100 nm, in a circular area with a radius of 0.75 cm. The center of the measured area was approximately 1.5 cm from the samples' edges on one side. The backside of the samples was washed with deionized water and isopropanol and dried with a pressured air gun prior to measurements. After seawater exposure, the measurements were done in areas with visible deposits when possible.

4.3.4 SEM and EDS analyses

The SEM and EDS analyses were done 34 days (due to Covid-19) after seawater exposure to quantitatively and qualitatively identify the precipitated compounds on the surfaces. Due to large surfaces - and many samples, only a selection of the samples was analyzed by SEM, given in Table 5. The samples were chosen with respect to clear deviations in transmission measurements, different coating materials, and roughening methods. The EDS analyses were done at 15 k, using the software Quantax 70. After analysis, the samples were rinsed thoroughly with de-ionized water until no visible precipitation was seen and left to dry in the fume hood overnight. A new analysis was done on all samples (Table 5) the next day.

Table 5: An overview of the samples analyzed with SEM after seawater exposure.

F1M
F4M
G3M
Ref H2
U1H
U2H
U5M

5. Results and discussion

The main objective of this study was to obtain a hydrophobic, self-cleaning surface by coating glass substrates with TCPFOS or ODFDHN. Characterization of the coated samples is discussed in 5.3-5.6. A summarized discussion is given in 5.7 and a scalability analysis is conducted in 5.8. Additional data are presented in 8.3-8.9 and the overview of sample series are found in Table 4.

5.1 Seawater salinity

Seawater salinity was calculated for all four samples (raw data is presented in table 8, appendix 8.3), as given in Figure 5.1. The salinities have their uncertainty since it has been calculated based on only one sample measurement per location. A larger number of samples with seawater from the different locations should be measured to obtain a smaller uncertainty. The results, however, indicate whether the samples have salinity as average seawater or large deviations in either direction. As seen in Figure 5.1, the samples from Aksnes, Bømlo and Kvalsvik all had salinities close to the average of 3.5 wt.%. The water from Karmsundet showed a large deviation from the other three. Probably this is because the sample was collected in surface water in a sheltered area of a marina. Seawater from Aksnes was chosen for further experiments as it had the highest calculated salinity, and hence assumed to represent the "harshest" seawater conditions.

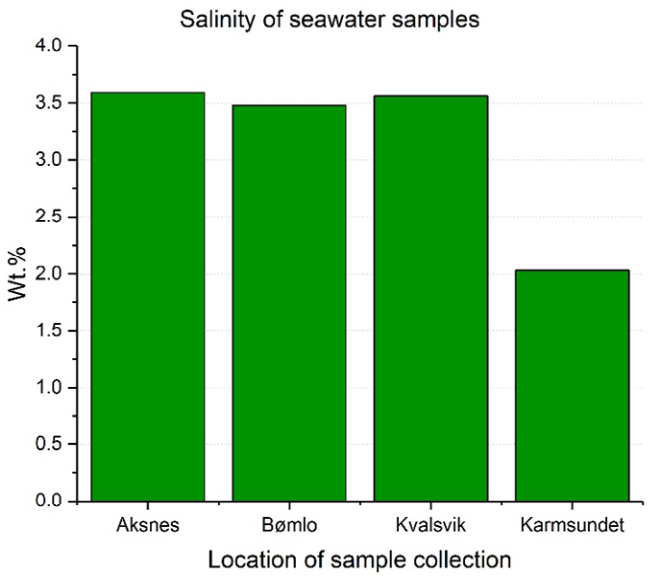

Figure 5.1: Salinity of the seawater samples in terms of weight percent of salt. No error bars due to only one measurement per water sample. The given average salinity of seawater is 3.5 wt.%.

5.2 Tuning temperature and RH

Based on the method described by Maharjan et al. [18], the coating process should be done in a vacuum furnace at 16% RH. However, due to the lack of appropriate equipment to specify RH in the furnace, an observational experiment was done to map the development of RH as a function of the temperature when heating without a vacuum. Figure 5.2 shows the development for 23 minutes of RH versus temperature in the VACUtherm furnace without vacuum (raw data is given in table 9, appendix 8.4), decreasing every minute and reaching a RH of 16% at approximately 30°C. The same experiment was initiated with a vacuum but was canceled as the RH quickly decreased and stabilized at 10% which is the sensors' lower limit. Hence, the part of the recipe stating an RH of 16% in specific, in a vacuum furnace was considered less important. However, coating with a too low water content, the hydrolysis which is one of the two coating-steps will be inhibited. In the situation of coating a surface directly by vapor, a high excess of water may be undesirable as it can form a water-layer on the sample before coating and hence inhibit the attachment of the coating to the surface. Hence, the RH in the furnace was tried kept around 16% at the beginning of the coating process. As the method is vapor coating, the flashpoint needs to be reached in terms of vaporizing the coating liquid. TCPFOS has a flashpoint of 87°C and heating the furnace to such a temperature would lead to an RH very close to zero. Based on these considerations, the coating method was further investigated in terms of both temperature, RH, and vacuum versus no vacuum. The same considerations lead to the decision of heating the vapor liquid to the flashpoint directly by using a pre-heated metal block instead of heating it in the furnace which would lead to a very low RH.

F1 was the only sample series that was coated in the furnace with a vacuum, while U3, F4, and G3 were coated in the furnace without a vacuum. The average temperatures and RH at three stages of the coating process are given in Table 6 and are in the range of 23.2-35.7°C and 20.7-10%, respectively (raw data presented in table 10, appendix 8.5). Sample series F1, F4, and G3 had an average RH of 16% or lower at the start of the coating process, while U3 had 20.7%. In other words, they were all coated at relatively low humidity. All sample series were coated for 20 minutes in the furnace. As described and discussed below (chapter 5.4 and 5.5), these variations in the coating method did not lead to any observable difference in the abilities of the resulting surfaces.

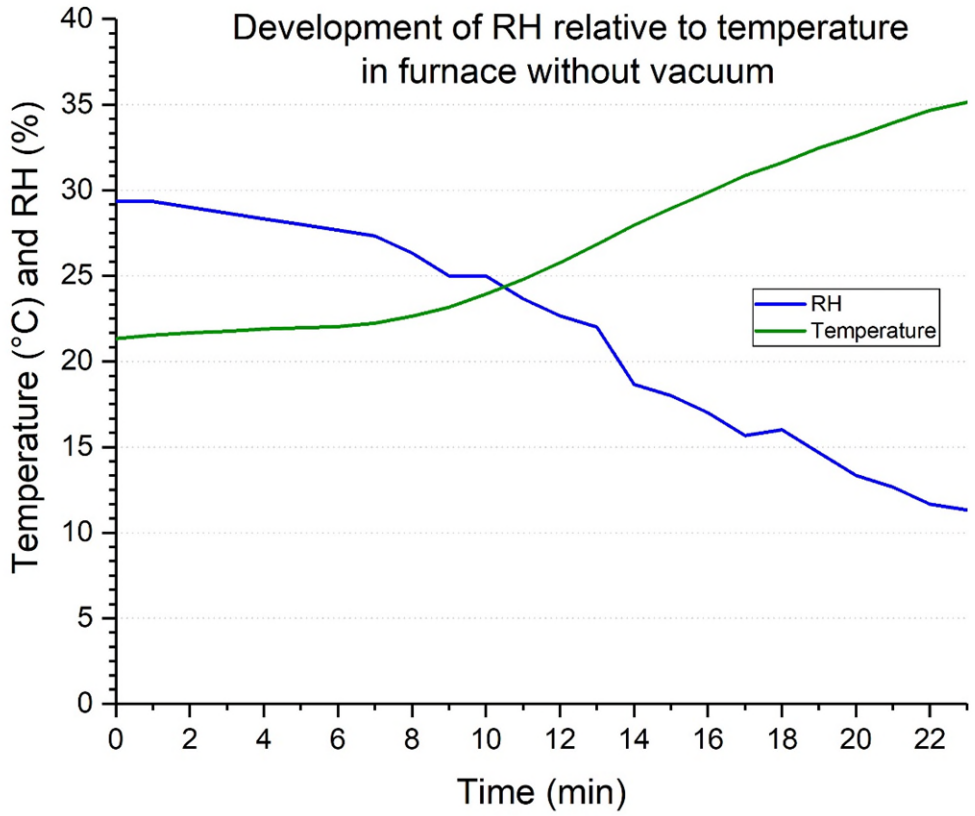

Figure 5.2: The development of relative humidity (RH) versus temperature when heating the VACUtherm furnace without vacuum for 23 minutes from ambient temperature.

Table 6: The average temperature and relative humidity (RH) in the vacuum furnace when coating started, 10 and 20 minutes in, respectively, for all sample series coated in the furnace. Sample series F1 was coated in a vacuum.

Name of sample series	The average temperature (°C) and RH (%) at start		The average temperature (°C) and RH (%) after 10 minutes		The average temperature (°C) and RH (%) after 20 minutes	
F1	23.2	14	25	10	26.9	10
F4	27.2	15	28.4	10.3	30	10
G3	24.5	16	26.4	14.3	27.2	13.3
U3	27.1	20.7	-	-	35.7	10

5.3 Characterization of the sample surfaces

The first step of preparing samples was polishing the surfaces with three different methods as described in chapter 4.2.2. Due to the fine abrasive used, it was not possible to control polishing results by the eyes. Hence samples prepared with the three different polishing methods were studied with a USB-microscope. As seen in Figure 5.3, the methods give widely different results (more images of each sample are presented in appendix 8.6). Firstly, one can see that reference sample B1 has, without being polished, some lines, spots, and cracks on its surface. Despite washing all samples according to the described washing procedure (4.2.2), sample F1L has obvious remains from the diamond suspension visible as glittering “snow” in some areas. Both samples G2L and F4H have straight lines in a random direction. However, F4H has a higher density of lines and with varying depth judging by the shade.

To further investigate the depth of these lines sample F4H was analyzed by AFM. Results are given in Figure 5.4 and show lines of varying orientation, depth, and width. The finer lines (Figure 5.4 a) are 4-6 nm deep and 50-200 nm wide. The deeper lines (Figure 5.4 b) are over 100 nm deep with a width of 2-3 µm. It is reasonable to assume that the deeper lines are a result of the coarse abrasive, and the others a result of the polishing paper. Based on the images from the USB-microscope and the AFM results from analyzing F4H, it was decided that AFM analysis of the other samples were not necessary as the surface structure of F4H was considered the one closest to ideal. The polishing method using four fine diamond polishing papers with variable grain size was used for polishing all further samples. Based on these results and literature saying that structuring in nano and micrometer scale is necessary to obtain a superhydrophobic surface [75], F4-series could in theory have superhydrophobic abilities. However, this is not the case as will be described later (section 5.4). Hence, using a too rough abrasive for the first polishing might lead to randomly oriented deep grooves which makes it hard to obtain a uniform topography using a finer abrasive afterward. This may be avoided by using a less coarse abrasive for the first polishing round or skip it and polish by the delicate abrasives at once.

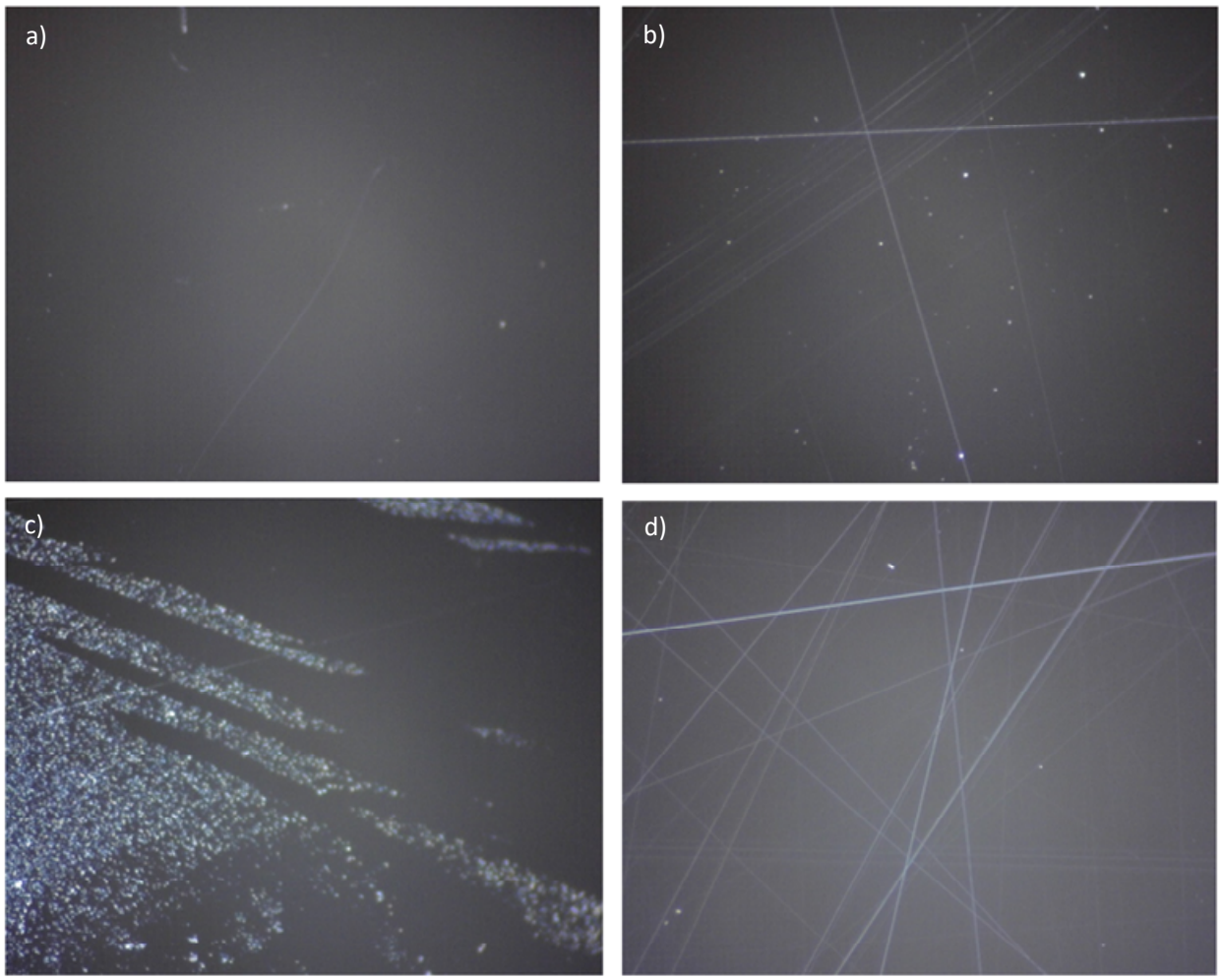

Figure 5.3: Images were taken at a magnification of 778 by a USB-microscope. a) Sample B1, untreated glass b) G2L polished with coarse abrasive only c) F1L polished with coarse abrasive then with 0.1µm diamond suspension and polishing cloth, d) F4H polished with coarse abrasive then with fine polishing papers.

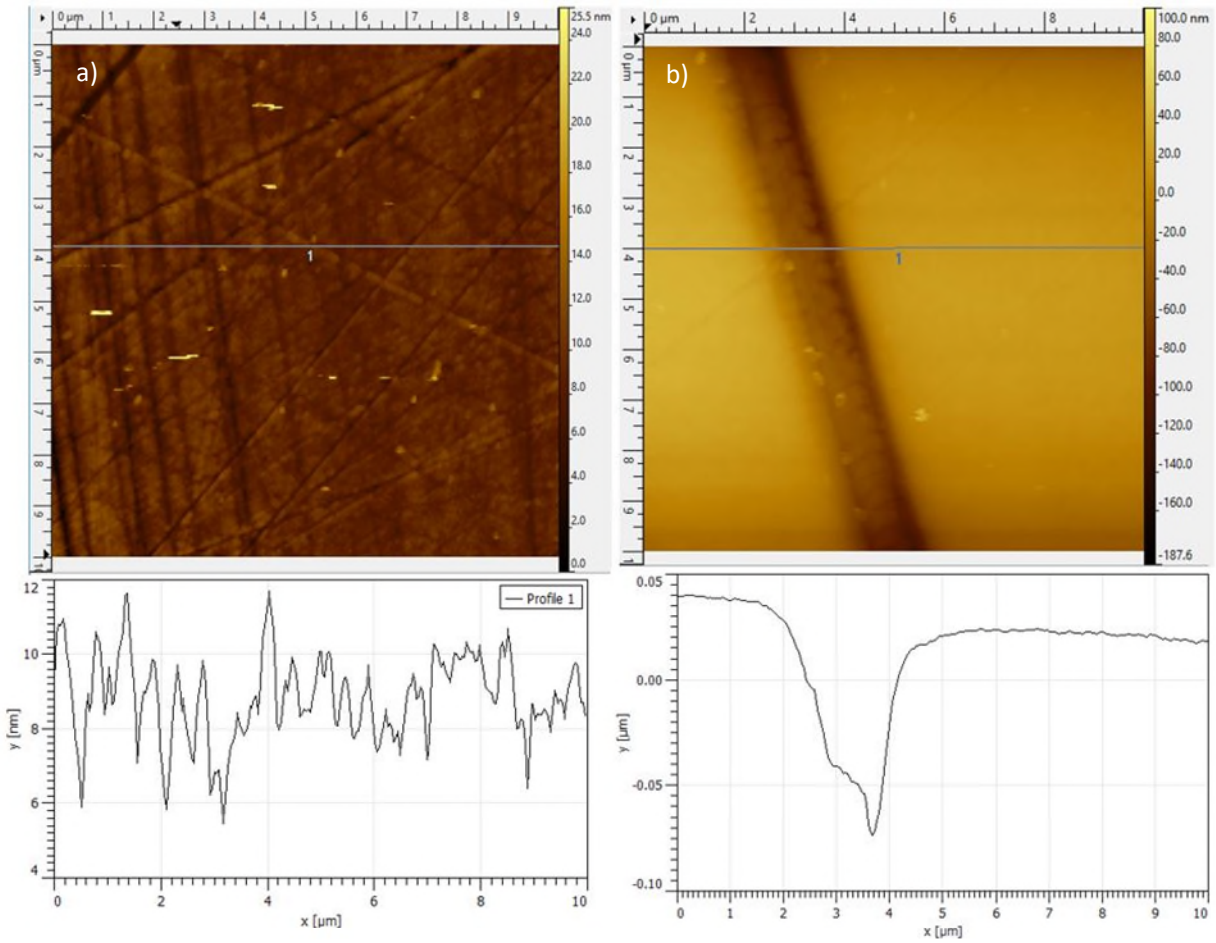

Figure 5.4: AFM measurements of sample F4H. Measurements following the horizontal line marked with 1. Graphs below photos show how the surface topography varies along the grey lines. a) Measurement of some narrower lines b) Measurement across a deeper line.

5.4 Contact angle measurements

Contact angle measurements were done to map the wetting abilities of the surfaces after roughening and coating. According to our hypothesis, hydrophobicity is the main effect to decrease seawater precipitates from forming on the surface, therefore, higher contact angle measurements are considered better results. An overview of the average contact angles of all samples and sample series along with their calculated standard deviations are presented in Table 11, (data is presented in table11, appendix 8.7). All samples coated in this study have hydrophobic contact angles except samples in the F2-series. Figure 5.5 gives an overview of the average contact angles for the hydrophilic samples and Figure 5.6 for the hydrophobic sample series. Calculations are done in Excel by using the built-in functions and specific formulas: average and Stdeva (the definition of

the standard deviation are given in appendix 8.2). The average error-bars for each sample series are calculated as the square root of the average standard deviation from each sample in the series by the combination.

All samples have higher contact angles when measuring with seawater, in accordance with the literature as the solid-liquid and liquid-vapor surface tensions are increased [44]. The difference in contact angle measured with water and seawater does vary among the sample series. However, the average increase in measured contact angle with seawater from de-ionized water among the hydrophobic sample series is 5.1°, using 0.2 µL droplets when measuring. Among the hydrophilic samples, the increase when measuring with seawater was substantially larger. Even when taking into consideration the small number of samples, a double of average increase, at 10.8° is measured. All contact angle measurements were done the first five seconds from the droplets landed on the surfaces. Exceeding this time, it was possible to observe an increase in contact angle at hydrophobic samples and decrease at the hydrophilic samples. Seawater having an increasing effect on the hydrophobicity is positive in terms of the hypothesis, as seawater will be the main source of exposure offshore.

The F2 sample series is the only one prepared in this study showing hydrophilic (near superhydrophilic range, which is < 5°) characteristics with an average contact angle of 13.5° with de-ionized water and 30.2° with seawater. The same coating method and material were used for the U5 series (casting knife w/ODFDHN), which has hydrophobic results. The U5 series was not roughened, and F2 was polished by diamond suspension and polishing cloth. As seen in Figure 5.3, this polishing method led to remains of diamond suspension on the surface, which may contribute to causing the low contact angles measured. One hypothesis is that the remains from the diamond suspension left the surface “wet” which interfered with the ODFDHN molecules during coating. As seen in Figure 5.5, F2-series shows substantially increased hydrophilic abilities compared to the samples from Pilkington. The average standard deviation indicates the uncertainty of the measuring method and/or the uniformity of the coatings. The highest standard deviation from measurements on an individual sample is 10.6° on Pilk1 with de-ionized water. The average standard deviation for measurements on the sample with both de-ionized and seawater is 2.56°. Pilk1 and Pilk2 were not in any way coated or changed and were measured as received from Pilkington. As the commercial sample Pilk1 has the highest standard deviation, deviations close to or less than this are assumed acceptable in a commercial context.

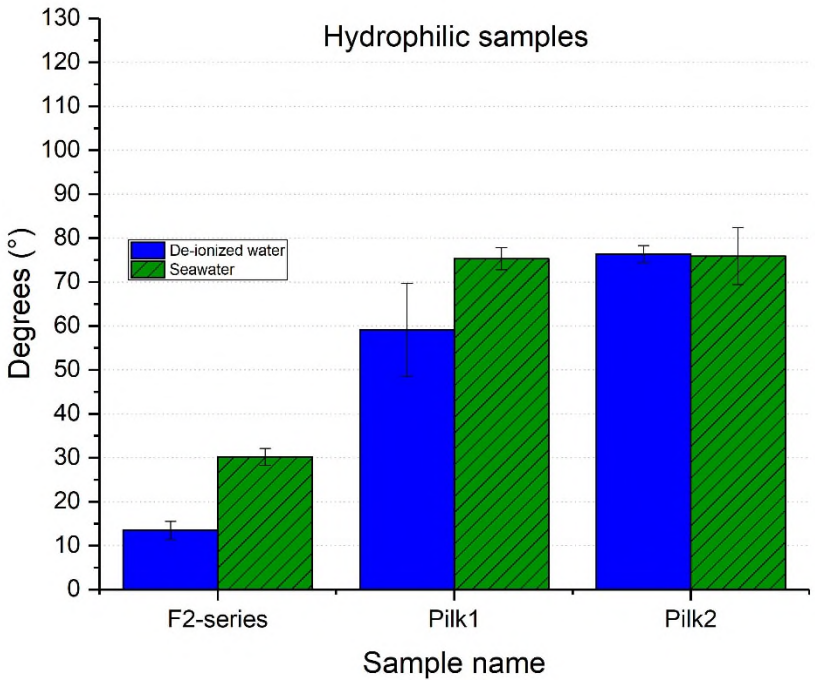

Figure 5.5: The average contact angles for the hydrophilic samples/sample series F2, Pilk1 and Pilk2 with associated error bars. Blue and green columns are calculated from measurements done with de-ionized water and seawater, respectively.

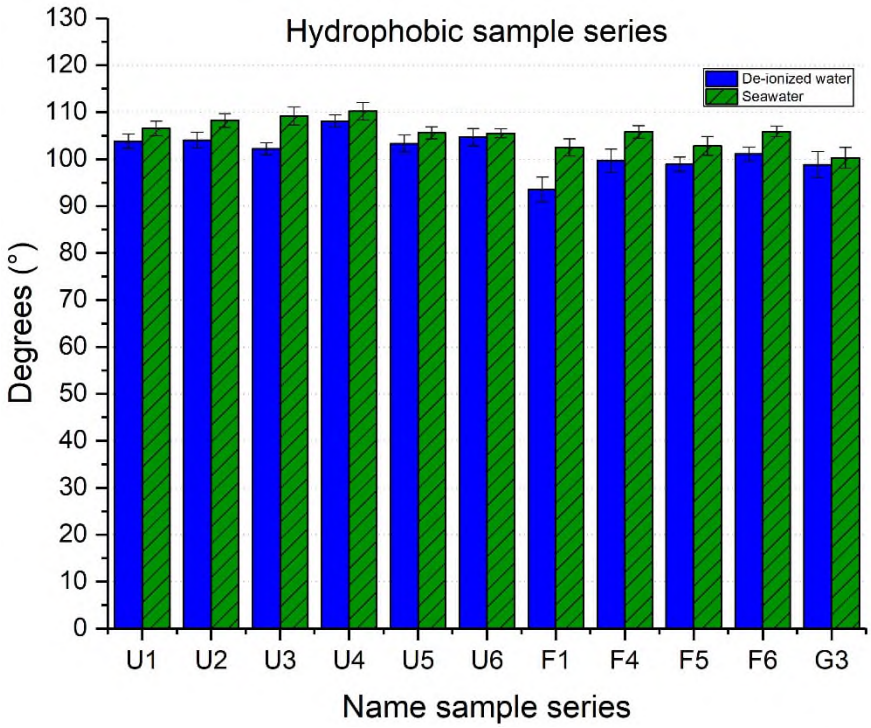

Figure 5.6: The average contact angle for the hydrophobic sample-series and associated error bars. The calculations are based on three measurements per sample. Blue and green columns are calculated from measurements done with de-ionized water and seawater, respectively.

Independent of the surface roughening, the coating method, and/or the material, all hydrophobic samples have average contact angles in the range of 93-108° with de-ionized water and 101-110° with seawater (see Figure 5.6). The average standard deviation for all series in Figure 5.6 is ± 1.4° for measurements with deionized water and ± 1.3° with seawater, which is less than 1%. Such a small standard deviation indicates uniform coatings, high reproducibility, and low uncertainty of the measuring method.

Only four sample series were coated with ODFDHN, and their average contact angles are presented in Figure 5.7. Sample series F2 is highly deviating from the others. While U1, U5, and F6 all have measurements in the hydrophobic range (98–107°), F2 shows near superhydrophilic properties with the lowest measured contact angle at 11.6° as discussed above. Average contact angles from measurements with seawater for U1, U5, and F6 are all in the small range of 105.6-106.5°, independent of the roughening- and coating method.

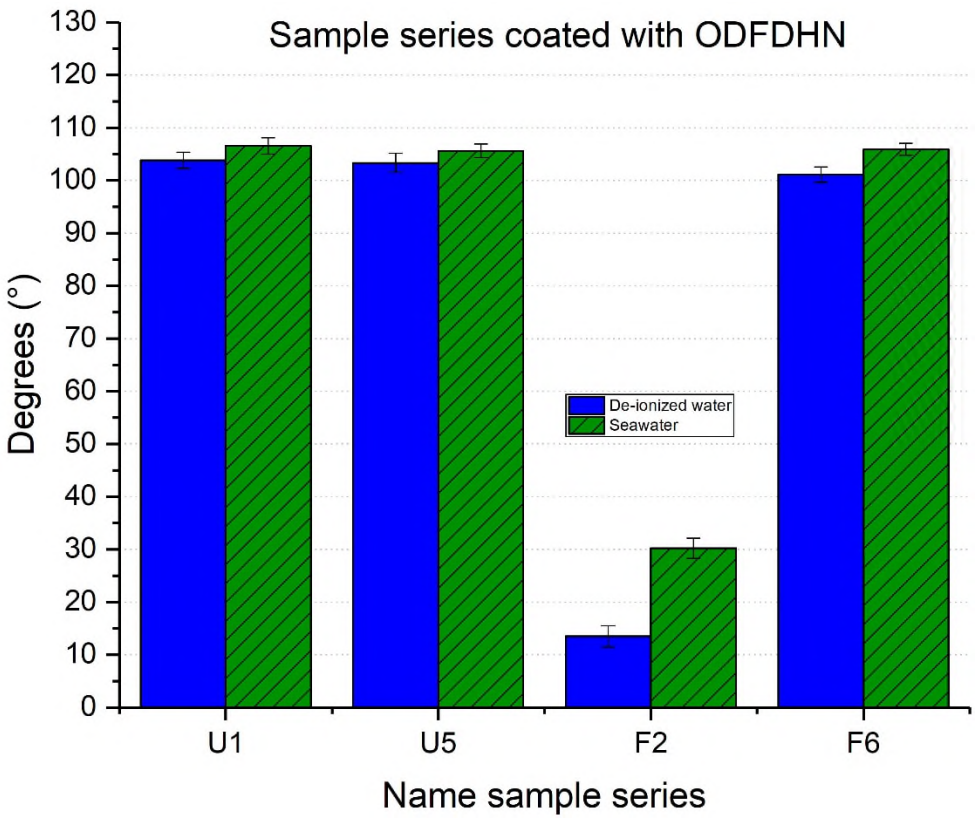

Figure 5.7: The average contact angles and associated error bars for all sample series coated with ODFDHN. Calculations are based on three measurements per sample in all sample series. Blue and green columns are calculated from measurements done with de-ionized water and seawater, respectively.

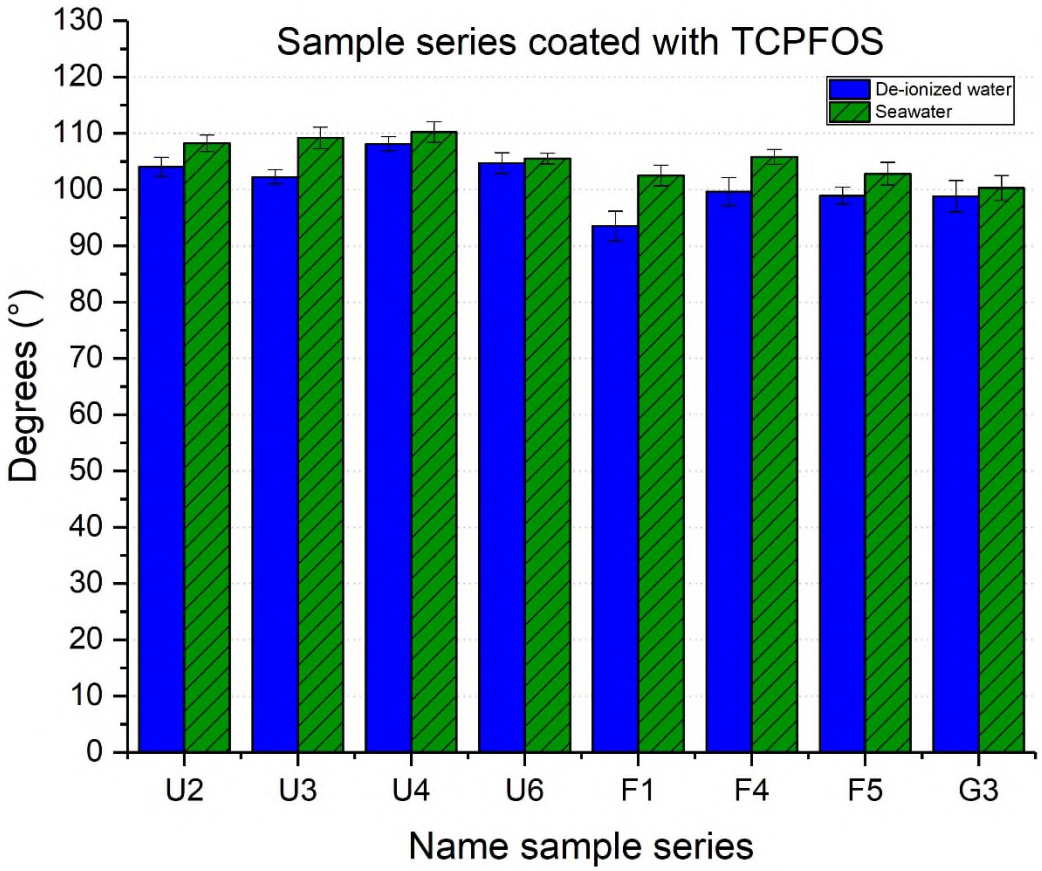

Figure 5.8: Average contact angles and associated error bars for all sample series coated with TCPFOS. Blue and green columns are calculated from measurements done with de-ionized water and seawater, respectively.

The average contact angles for the sample series coated with TCPFOS is given in Figure 5.8. All sample series and individual samples have average contact angles in the hydrophobic range. F1-series has the lowest average contact angle with de-ionized water, at 93.5°. The series was polished with diamond abrasive by hand and coated with TCPFOS in the furnace with a vacuum. If vacuum is the factor responsible for this result, inhibiting the coating process, the measurements should be even lower and equal to non-treated glass. Thus, the effect might have something to do with the observed remains of diamond suspension in Figure 5.3. Hence adding disfavor for that polishing method.

The G3-series was only polished with the coarse abrasive before coating with TCPFOS. This was done to identify any substantial differences compared to the samples polished in two steps. Such information is necessary to strip the process of any ineffective steps, hence making it

more time- and cost-efficient. U4-series had the highest contact angles and was not polished in any way prior to spin-coating with TCPFOS and drying in vacuum. All U-series have contact angles well above 100°. In other words, roughening of the surface prior to coating does not represent a clear advantage in terms of wetting abilities.

For the sample series coated with TCPFOS by vapor in the furnace (U3, F1, F4, and G3), the distance from coating liquid has a potential impact on the resulting coating and thus measured contact angles. These samples were, as described in chapter 4, marked with L, M or H depending on the distance from the coating liquid (Figure 4.8). The average contact angles for the individual samples are shown in Figure 5.9, with no clear trend correlating distance from coating liquid and measured contact angles. However, the M-samples tend to have the lowest average contact angle in their series, which may be a result of sample L partly blocking for free deposition due to the setup (Figure 4.8). Either way, based on these results, the distance from coating liquid is not considered a crucial success factor for obtaining a hydrophobic surface through vapor coating.

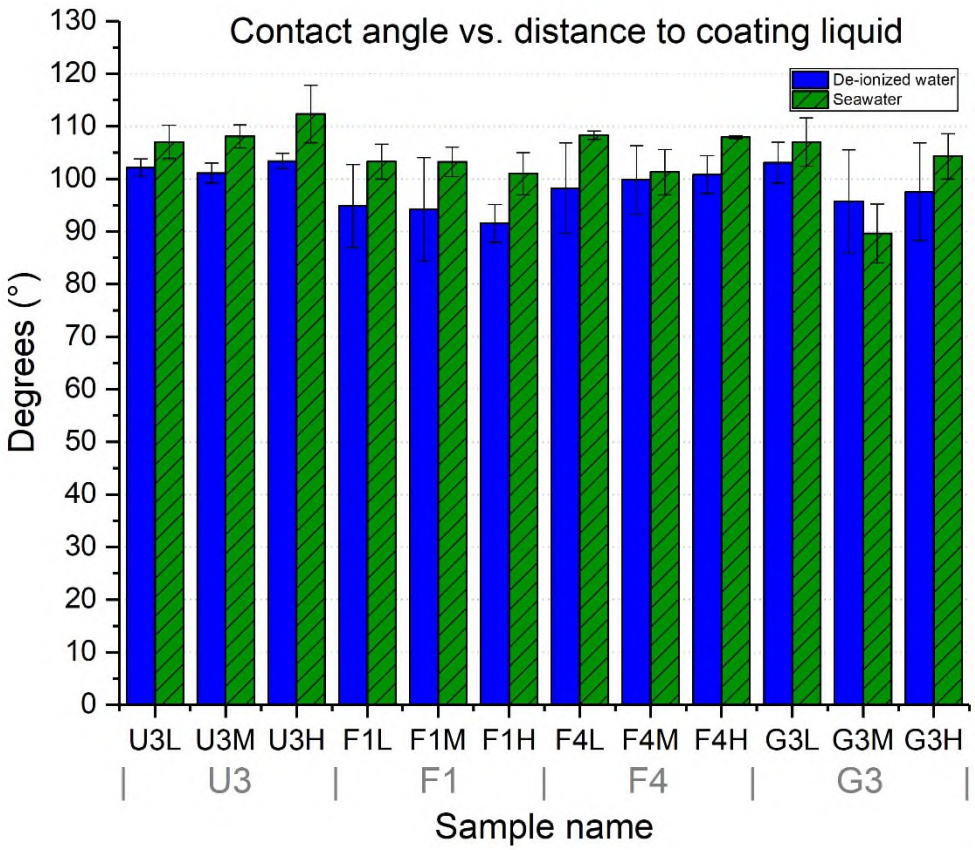

Figure 5.9: The average contact angle and associated error bars for individual samples of the four sample series coated with TCPFOS in the furnace. L denotes samples closest to coating liquid, H the furthest away, and M in between. Blue and green columns are calculated from measurements done with de-ionized water and seawater, respectively.

All coated samples, except the F2 series, have hydrophobic wetting abilities, with increased contact angles when measured with seawater. The cause of the F2 series having hydrophilic abilities is assumed to be the remains of diamond suspension on the surface after polishing, and hence a wet surface when coating with ODFDHN by casting knife. There is no obvious difference in the contact angles between samples coated with ODFDHN compared to those coated with TCPFOS. Neither when comparing roughening methods and/or coating methods. Both materials and all methods used resulted in hydrophobic coatings with relatively stable contact angle measurements. The amount of coating liquid, temperature, RH, distance from coating liquid, and vacuum/no vacuum did not result in any distinct changes in the contact angles and are thus considered non-critical success factors for obtaining a hydrophobic coating.

5.5 Transmission measurements

All samples had two transmission measurements done both before and after seawater exposure. As seen in Figure 5.10, the transmission measurements follow either of two curves; a steep or a flatter one, depending on the shade of the glass substrate. The flatter curve represents samples of standard glass and the steeper one samples of glass with a hint of green (Figure 4.1). Both start within 89-91% transmission at 400 nm and do not deviate more than 2% until reaching a wavelength of 600 nm before the deviation increases. The difference continues to increase between the curves and reaches its greatest at 1100 nm, with a 13.2% difference. The standard deviation is less than 0.2% for both reference samples. It is not surprising that the substrates of glass with the green shade have a somewhat lower transmission compared to the standard substrates. The green shaded substrates contain small amounts of ions as either dopants or impurities which absorbs certain wavelengths and hence causes a change in the color. An additive that causes green shade when used in SiO_2 glass is iron oxide, which has a broad adsorption band in the infrared area of the spectrum (700–1100 nm) depending on the amount and size of particles added [76-78]. Comparing to the green curve in Figure 5.10, it decreases in the same range of wavelengths, which implies that iron oxide may be the cause of the green shade of these glass substrates. To analyze the transmission loss caused by the coating materials and roughening methods, the coated samples must be compared with a reference sample corresponding to the same shade of substrate (shade of glass used for the different sample series is given in Table 4).

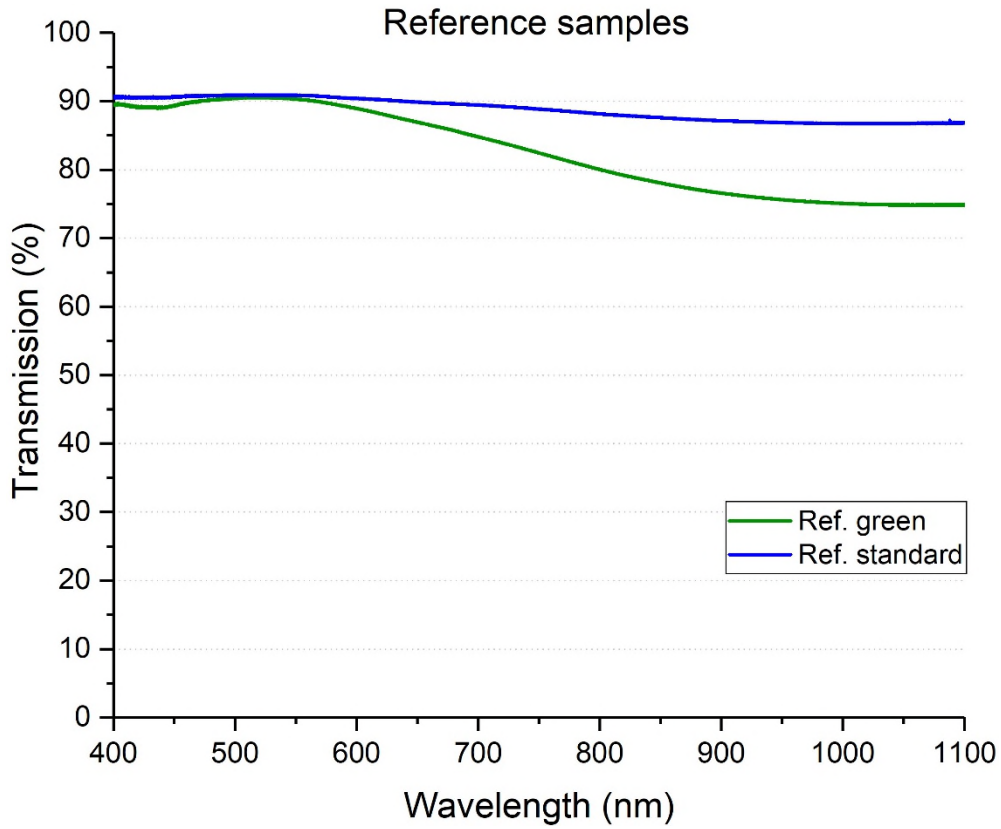

Figure 5.10: Transmission in the range of 400-1100 nm for reference glass substrates in both shades.

The average transmissions for the sample series coated on glass substrates with green shade in the range of 400-1100 nm are shown in Figure 5.11. All samples follow the reference curve closely until approximately 700 nm where the U-series 1 - 4 increasingly deviates throughout the wavelength range. At 1100 nm the deviations are largest, however, they are no more than 1.5%. This indicates that the roughening of the surfaces somewhat increases the transmission of the surfaces. Such an effect caused by surface roughening are assumed to be due to the increased surface area, and hence becoming less-reflecting surfaces.

The average transmission for sample series coated on glass substrates without any shade (standard) in the range of 400-1100 nm is plotted in Figure 5.12. All curves follow the reference closely throughout the range, and no visible deviations are observed. This weakens the basis of the assumption made above, as the unpolished samples don't deviate from the roughened samples and the reference. Thus, the effect observed in Figure 5.11 may be connected to the chemical elements present in the green shaded glass and their participation in the surface chemistry when roughened.

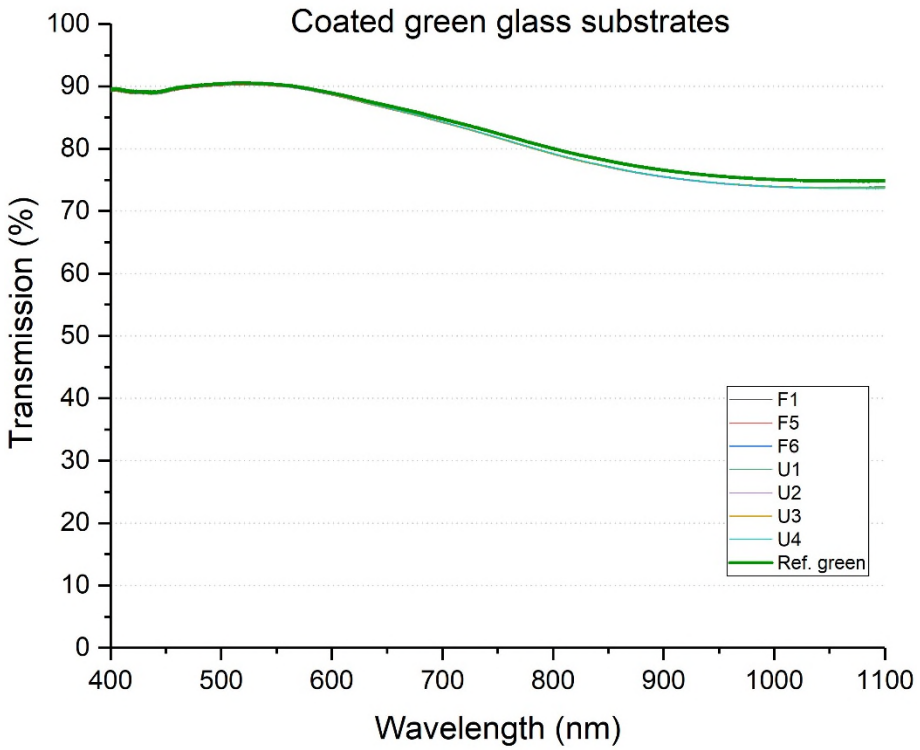

Figure 5.11: Transmission of glass samples with green shade compared to the reference sample in the range of 400 – 1100 nm.

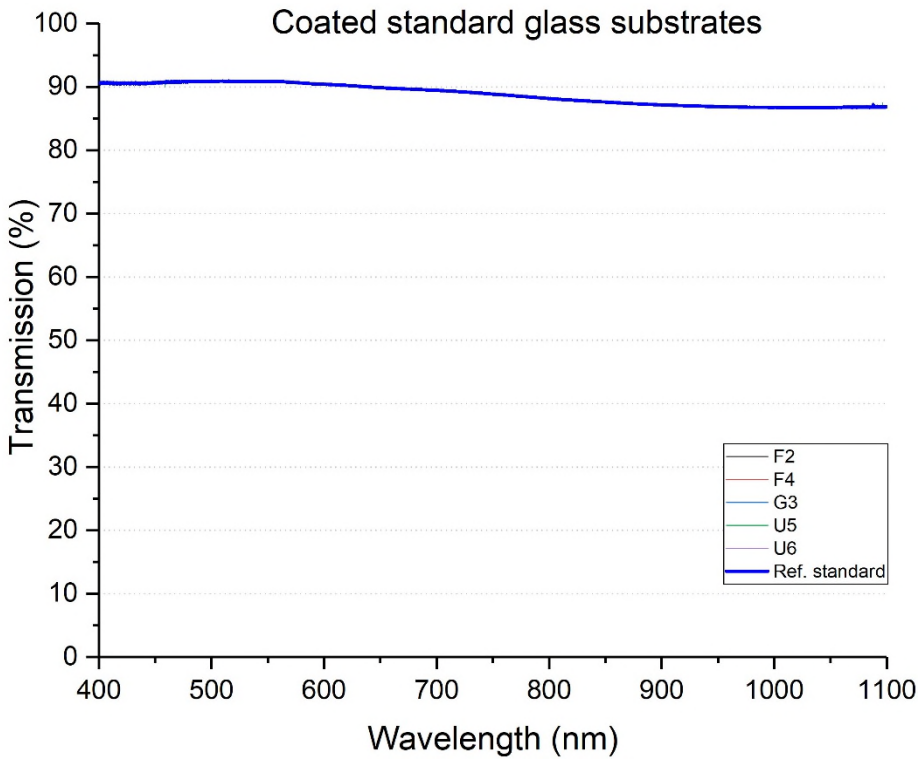

Figure 5.12: Transmission of coated samples on standard glass substrates in the range of 400 – 1100 nm, compared to the reference sample (thick blue).

It would, however, be interesting to further investigate the effect of surface roughening has on transmission, as well as the variation in the effect due to substrate thickness and chemical composition.

As seen in Figure 5.13, the hydrophilic and photocatalytic reference sample from Pilkington, Pilk2, shows a maximum transmission of 54.9% at 472 nm and a minimum transmission of 10.7% at 1100 nm. The curve is plotted as the average of two measurements with an average standard deviation of 0.13° and a median standard deviation of 0.12°. A reference measurement of the blue glass substrate is not available, so it is not possible to identify how much transmission loss is caused by the substrate itself and how much is caused by the coating. The transmission losses caused by the glass is, however, assumed to be substantial, when compared to the transmission properties of TiO_2 given in the literature (Figure 3.7). Either way, the specific combination of this glass substrate and TiO_2 coating is not suitable for the application as a protective glass for PV panels as it has a very low transmission in the visible part of the spectra.

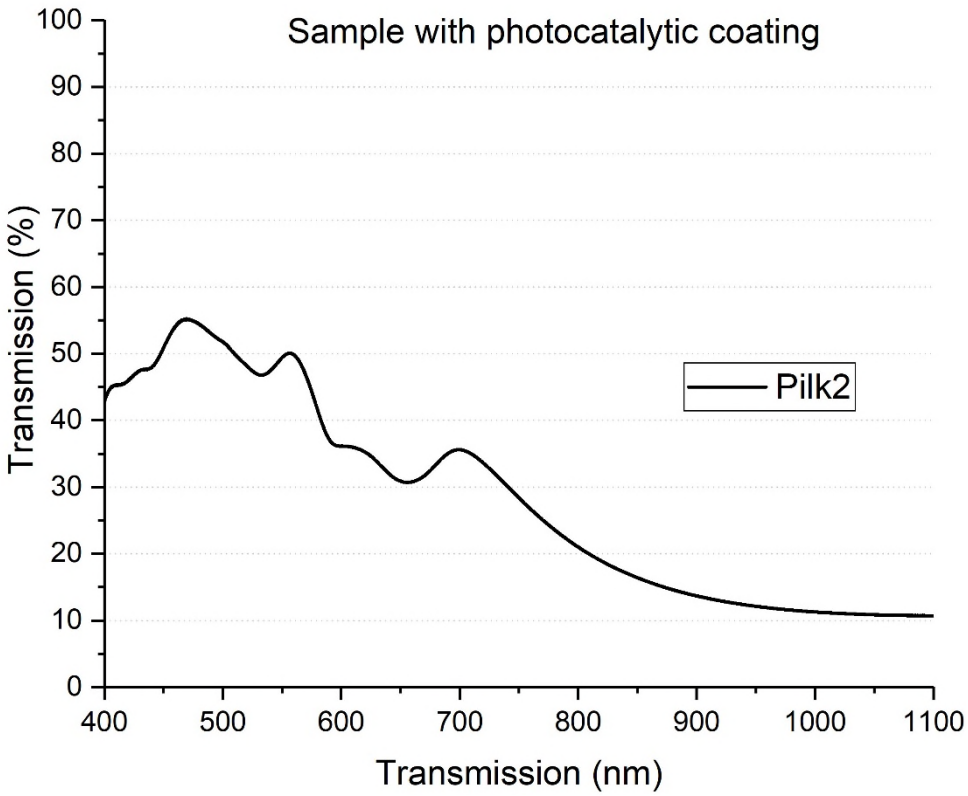

Figure 5.13: The transmission curve for Pilk 2 hydrophilic and photocatalytic reference sample from Pilkington in the range of 400-1100 nm.

When it comes to differences in transmission when comparing the two coating materials, TCPFOS and ODFDHN, there is no observable difference. In terms of H and M samples, and hence different exposure to seawater/rainwater, there are no visible differences in the amount and/or form of seawater precipitates on the surfaces, and neither in the transmission done on them after seawater exposure.

After seawater exposure, most samples had visual salt deposits which were expected to decrease the transmission of the samples due to absorbance, scattering and reflection. Transmission measurements were done in areas of visible precipitation when possible, and the measurement with the lowest transmission per substrate shade are presented in Figure 5.14, along with the reference measurements for the coatings before exposure and substrate references for comparison. Both decreases in overall transmission due to reflectance and absorbance, as well as transmission of specific wavelengths due to absorbing deposits are considered. For most samples, the measurement with maximum transmission losses done after seawater exposure differed by approximately the same percentage across the range of wavelengths compared to the reference sample. The transmission of the green substrates is deviating less from the reference sample, but this might be random as the measurements are dependent on the amount and type of seawater precipitates in the small area measured.

An instrument able to measure the transmission of the whole samples or less limited areas would be beneficial, as the measurements done after seawater exposure in this study only will be representable for a small area and not the whole sample. This is especially important to point out, as some samples had their measurements taken in areas with visible deposits while for other samples it was not possible to do due to the nature of the instrument's sample holder.

Sample U5M, showed the greatest loss in transmission after seawater exposure with an average decrease of 29.4% compared to the standard substrate, deviating most at shorter wavelengths (32.7%) and less for longer wavelengths (25.4%). A "dip" in transmission at approximately 830 nm is observed (Figure 5.14), which may be caused by absorbance by a precipitate. There is, however, not enough information to conclude whether the transmission losses are caused by a reflective, scattering and/or absorbing effect, so all three mechanisms are considered as contributing. Further information, through for example diffusive refraction is needed to conclude.

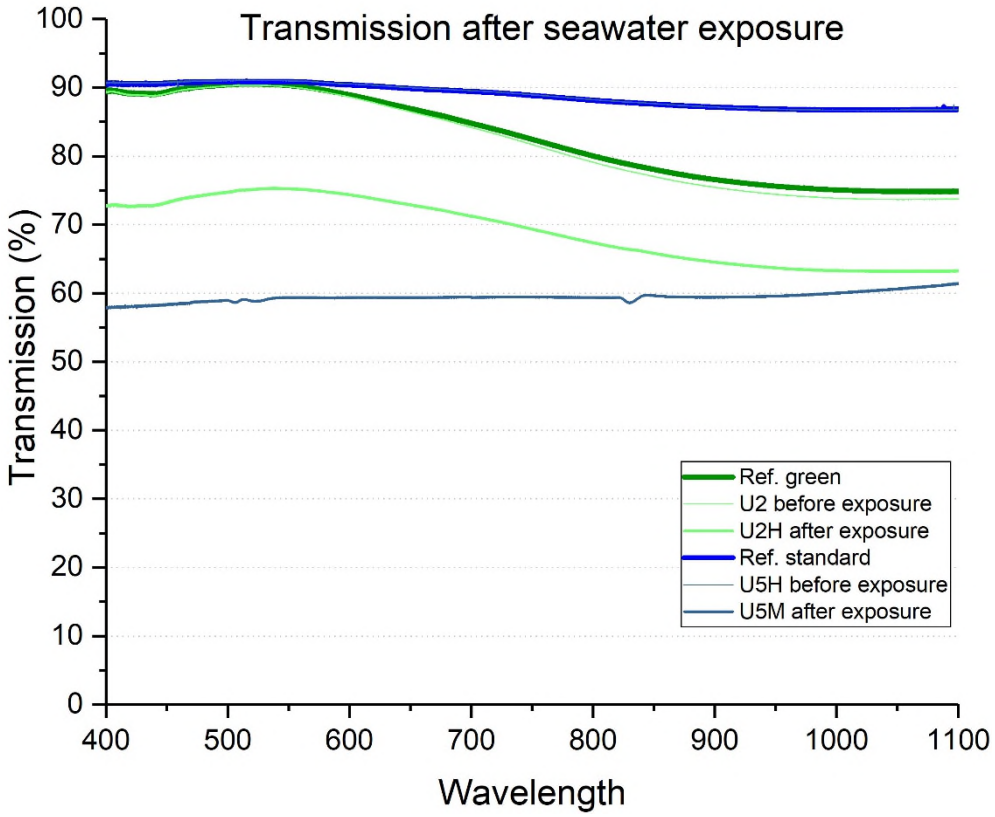

Figure 5.14: Transmission curves of green and standard shaded substrates with lowest transmission after seawater exposure compared to substrate references and measurements prior to exposure in the range of 400 - 1100 nm. Thick blue and green curves represent the standard and green reference samples, respectively. The finer blue and green lines are measurements done on U2H before exposure. The thicker dark blue curve starting at approximately 57 % represents the sample U5M and the thicker light green above represents U2H after exposure.

Transmission measurements indicated that the roughening method dominates the coating material in terms of transmission loss. Compared to the untreated references, none of the sample roughening or coating methods led to a decrease in transmission of more than 1.3% at any wavelength for any sample series prior to seawater exposure. Hence, both TCPFOS and ODFDHN can be used with a neglectable transmission loss. The samples with delicate polishing have a slightly higher transmission (1.3%) than the unpolished, hence the increased surface area causes a minimal increase in the transmission. Due to large surfaces and the small measurement area, it is inconvenient to compare the transmission losses of the M and H samples regarding the difference in seawater exposure. After seawater exposure, the transmission is in some cases decreased by as much as 30% in areas of visible seawater deposits. Thus, the hypothesis that precipitates from seawater decreases the transmission due to different surface effects is strengthened. To understand which mechanisms are responsible, more information is needed.

5.6 SEM & EDS analysis of seawater precipitates after indoor exposure

The seawater exposure was done indoors, with average temperature and relative humidity in the boxes of 20.8°C and 95.6%, respectively (raw data is presented in tables 12 and 13, appendix 8.8). These conditions do not correspond to the conditions offshore, and hence the results presented cannot be assumed as fully representable for the offshore conditions. Unfortunately, the planned exposure experiment in real conditions was not possible to do due to Covid-19. However, the results below give valuable information on general seawater precipitation on glass surfaces, but the factors of high temperature and RH must be kept in mind when drawing the longer lines. The M-samples were expected to contain more insoluble precipitates, as they were exposed to rainwater sprays every 6 hours during the exposure experiment. However, the variance in the amount and type of visible precipitation is too big within the two groups that it is inconvenient to compare the two groups. The graphs in the EDS analyses were saved with y-axis as intensity (cps/eV), without applying ZAF-corrections to obtain semi-quantitative concentrations, which makes a confident identification of the compounds somewhat hard. Hence, additional information could be gained from XRD analysis in further investigations. The two red, unlabeled peaks at 0.5 and 1.75 keV, corresponds to the substrate, hence oxygen and silicon, respectively. Measurements were done at 15 kV, which explains the mismatch in intensity for the curves compared to the ratio of SiO_2.

When it comes to surface areas without visible deposits, it is unclear whether they are covered with nanoscopic deposits or not. All samples had measurements done at x3000 in an area without visible deposits. EDS mappings (see Figure 5.15) detect a substantial heightened intensity of sodium, calcium, and magnesium. Some sulfur is detected, but not in such an intensity that all can be explained as sulfates. As hydrogen is not possible to detect and oxygen tend to be detected with smaller intensities than what is actually present, the elements may be oxides and/or hydroxides like $Ca(OH)_2$, $Mg(OH)_2$, $Na(OH)_2$. The former two are hardly soluble in water, which may explain the intensity of calcium and magnesium. However, $Na(OH)_2$ is highly soluble and should thus have been dissolved in rinsing with de-ionized water, so there is no obvious explanation of the elevated intensity of sodium as surface deposits. However, an explanation is that the substrate is lime-soda glass and not pure SiO_2 glass, and thus containing variable amounts of Na_2O, CaO, MgO, K_2O, Fe_2O_3, ZrO_2, Al_2O_3, SrO, and SO_3 [79]. Such a case explains the

somewhat uniform intensities detected in Figure 5.15, and explains the background intensities of Na, Ca and Mg detected in all EDS analysis presented below.

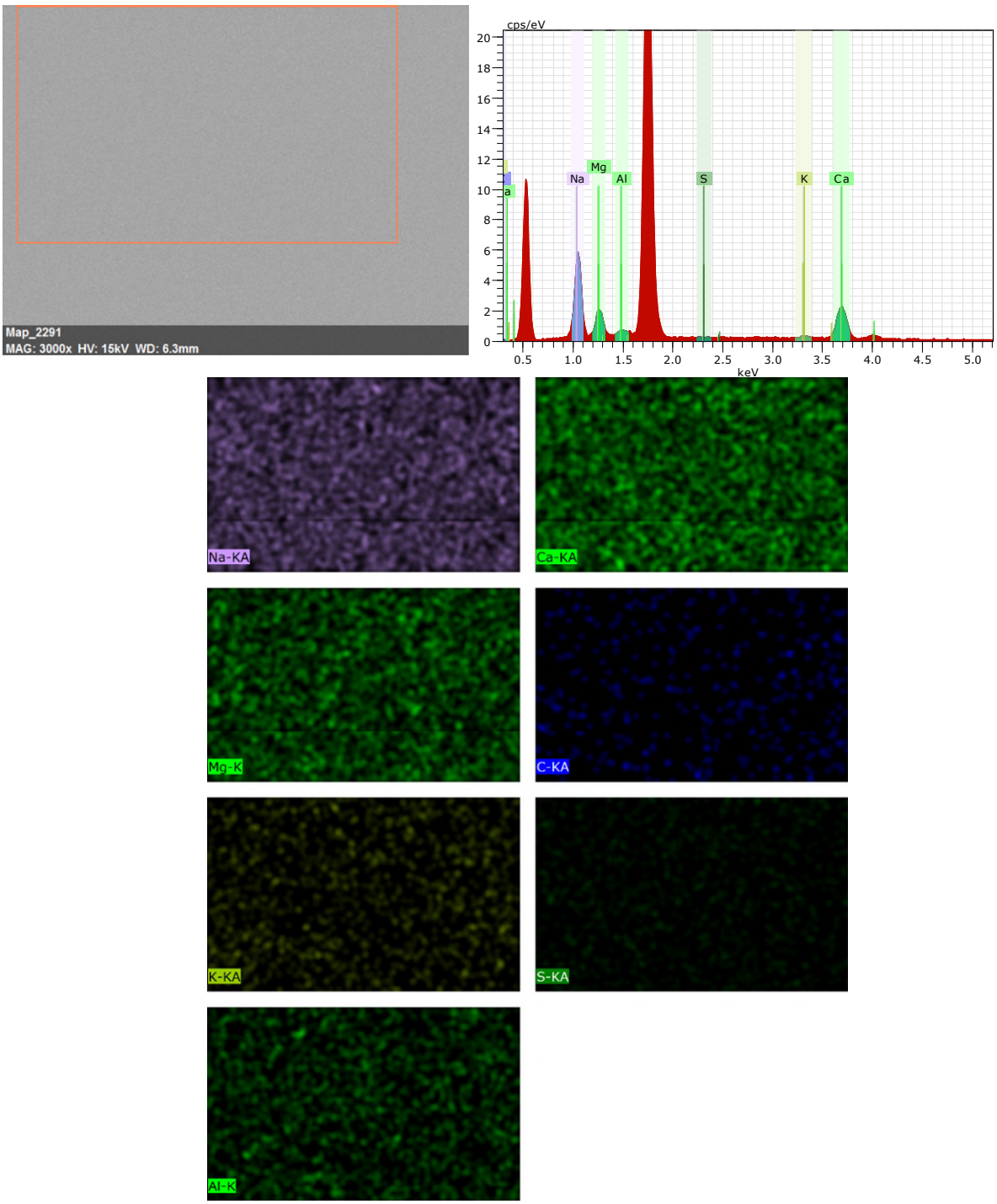

Figure 5.15: EDS analysis of U5M surface without visible deposits. The analyzed area is marked by the orange rectangular. The graph presents the intensity of the chemical elements detected in the area. Maps from EDS-analysis with brighter areas indicate a higher intensity of the given chemical element. The large red peaks represent oxygen and silicon, respectively.

Through SEM and EDS analysis of the surfaces (list of analyzed samples are given in Table 5, chapter 4.9.2) exposed to seawater, ring deposits with inner precipitation as described for hydrophobic surfaces in literature are observed [49, 51]. Ring borders as both closed- and open rings are observed. Independent of the size or location, all rings contain large, cubic NaCl crystals, visible as lighter than the other deposits (Figure 5.16). NaCl is observed with a connection to the border of the ring, so it seems that the first crystal nucleuses are formed near the border. More EDS mappings are presented in appendix 8.9.

The second most abundant compound detected on the surfaces beside NaCl, are small crystals containing elevated intensity of calcium and sulfur (Figure 5.17 and 5.18). The crystals have a distinct hexagonal structure in at least one direction and appear both with and without small center hole(s). These crystals are often accompanied by larger, darker, irregular deposits with elevated intensities for magnesium and chloride (Figure 5.17). This indicates magnesium chloride, which is a common seawater precipitate, in either anhydrous form or as a hydrate. However, based on the argumentation above, that hydrogen and oxygen are hard to detect, one must look for other information to distinguish whether the hexagonal crystals are CaS, $CaSO_4$, hydrates, anhydrates or other compounds.

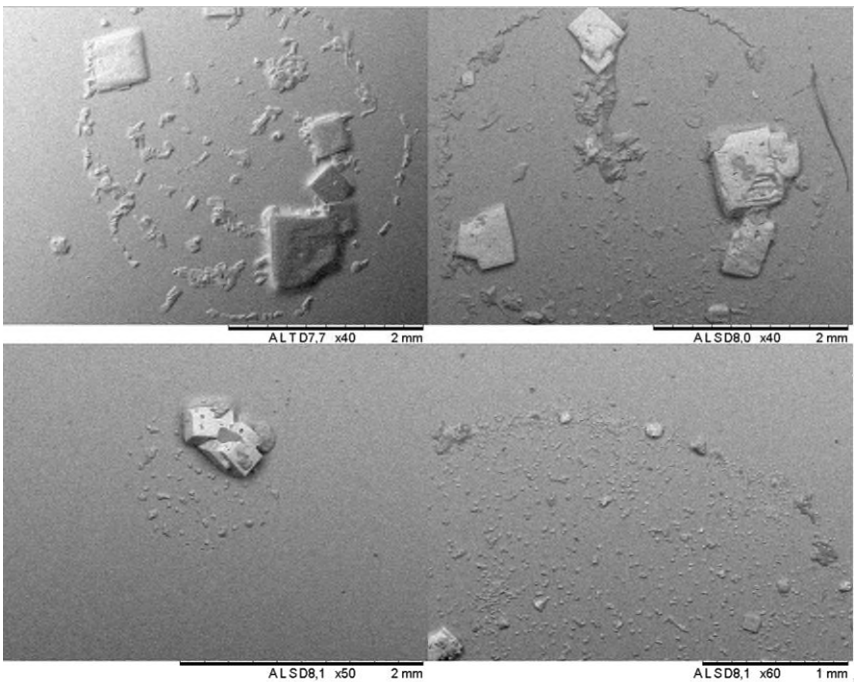

Figure 5.16: SEM images of distinct ring deposits of variable sizes with inner precipitation on hydrophobic surfaces after seawater exposure. The large, white, cubic crystals are NaCl.

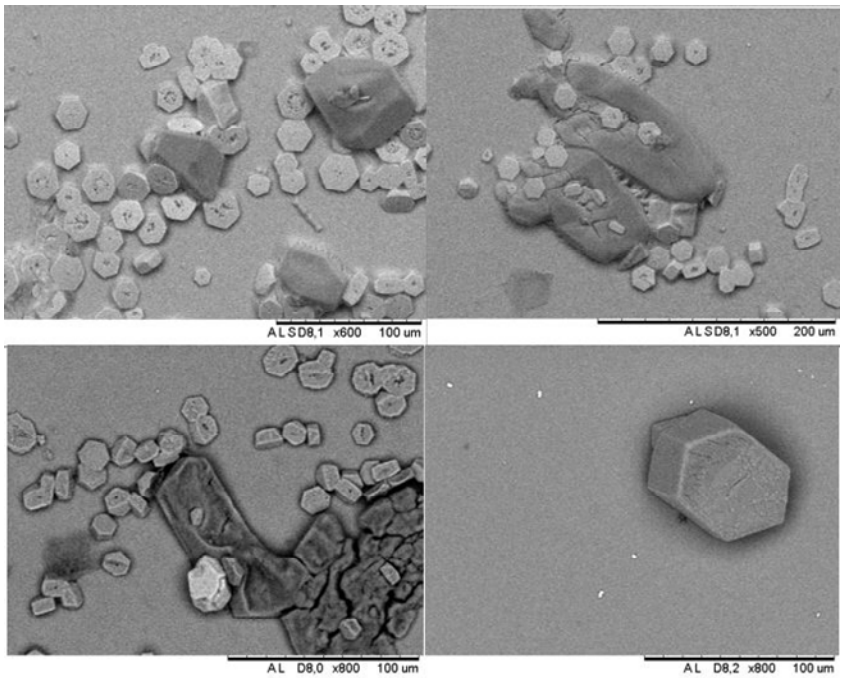

Figure 5.17: SEM images of hexagonal crystals containing sulfur and calcium with and without center hole(s). The darker and irregular precipitates contain magnesium and chloride and are assumed to be $MgCl_2$.

A range of other compounds is observed, and through EDS-analysis their composition may be suggested. In Figure 5.19, an EDS-mapping of a big cubic crystal surrounded by aggregates of small crystals is presented. Elevated intensities of calcium and sulfur are detected in the smaller crystals, as discussed above. The large cubic crystal has elevated intensities of magnesium, potassium, and chloride, which suggests a hydrate with the composition $KMgCl \cdot xH_2O$. In the EDS mapping in Figure 5.20, a large, irregular deposit are analyzed, with elevated intensities for potassium, sulfur, magnesium and chloride. The most obvious suggestion for compositions is K_2SO_4 and $MgCl_2$, however all chemical elements are detected in the same area without any clear distinctions. Thus, a hydrate containing all chemical elements are proposed: $KMgSO_4Cl \cdot xH_2O$. The EDS mapping presented in Figure 5.21 analyzes a big irregular, dark deposit with a lighter deposit attached. The latter has elevated intensities of sodium and chloride and are thus assumed to be NaCl. The big deposit has elevated intensities of magnesium and sulfur, which indicates it being a magnesium sulfate ($MgSO_4$) in anhydrous or hydrous form.

A list of suggestion for composition of the compounds observed by SEM and EDS-mappings after seawater exposure is given in Table 7. It also includes several suggested compositions for the hexagonal crystals.

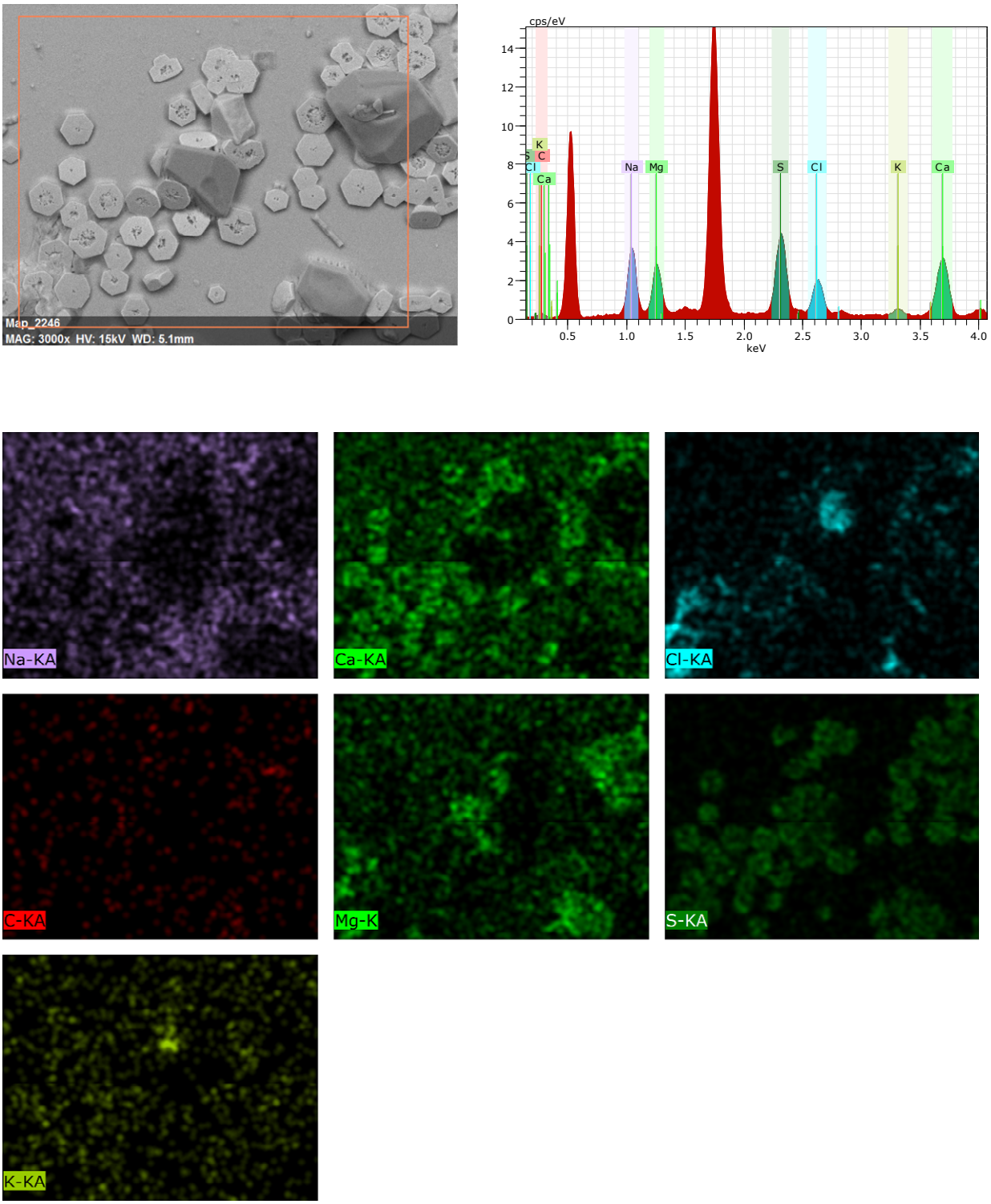

Figure 5.18: EDS analysis of hexagonal crystals containing an elevated intensity of sulfur and calcium on sample G3M. The analyzed area is marked by the orange rectangular. The graph presents the intensity of the chemical elements detected in the area. Maps from EDS-analysis with brighter areas indicate a higher intensity of the given element.

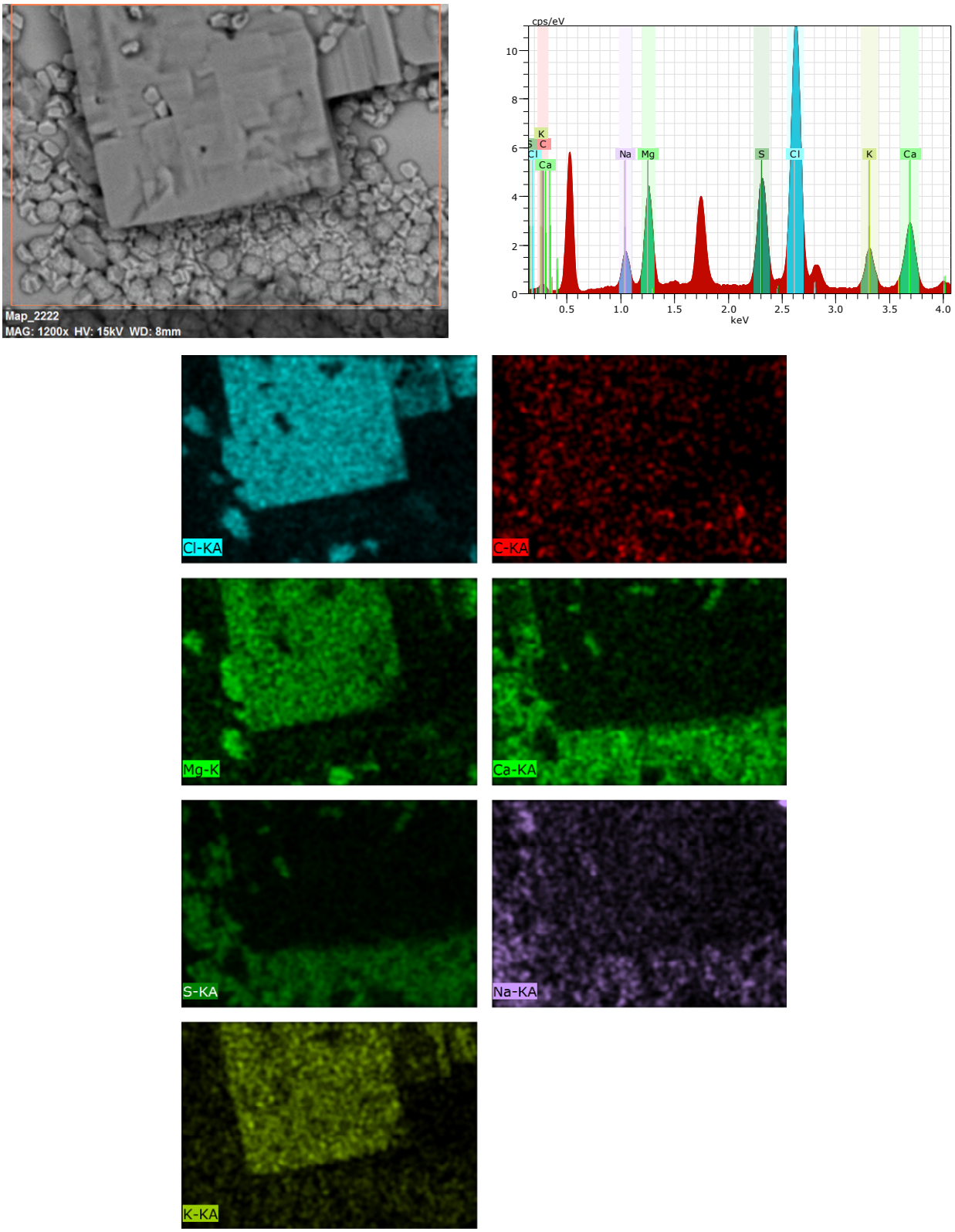

Figure 5.19: EDS analysis of F1M with an overview of the analyzed area, graph with quantities, and maps of where a higher intensity of the different elements are detected. The most prominent compounds in the cubic compound are magnesium, potassium and chloride.

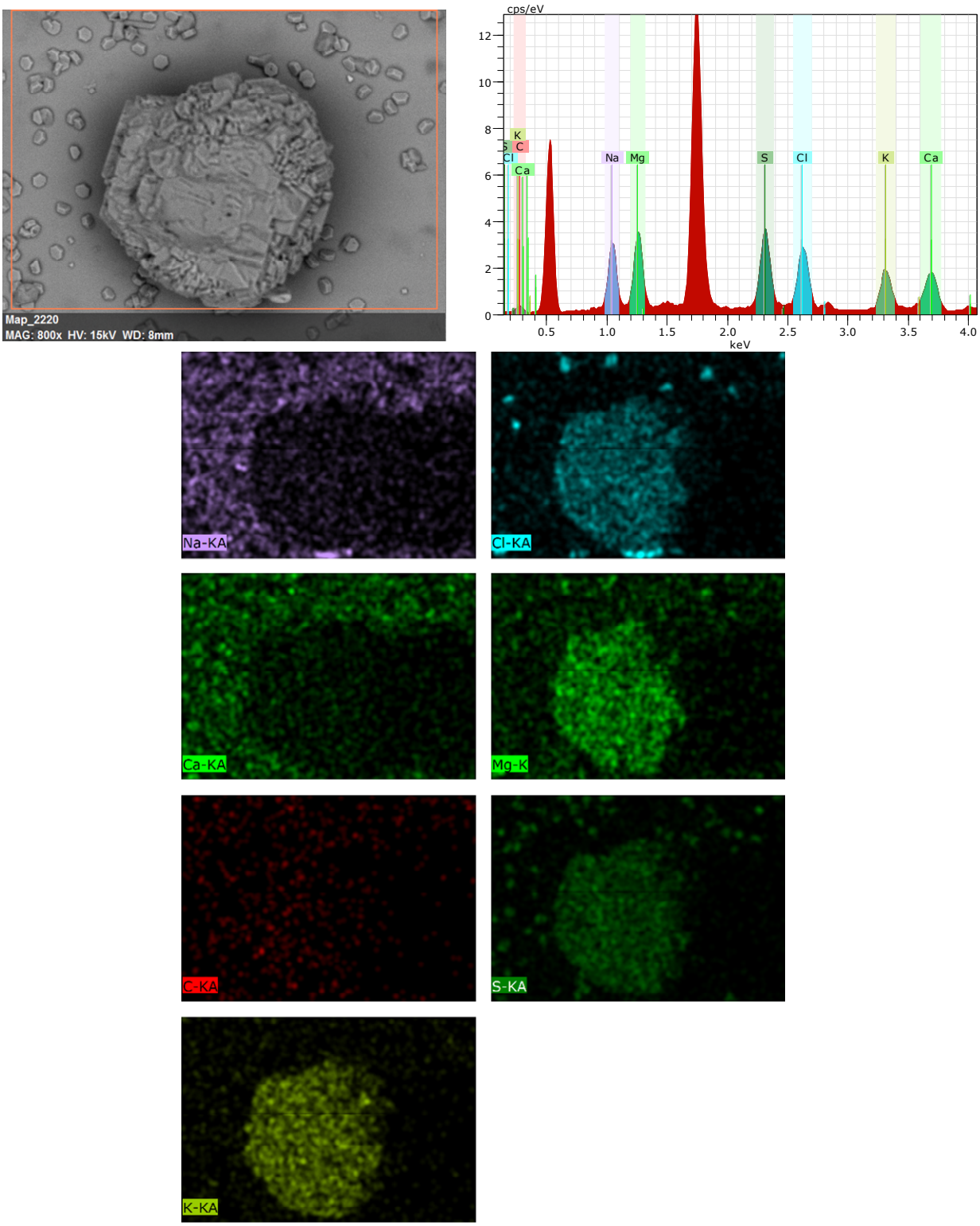

Figure 5.20: EDS analysis of F1M with an overview of the analyzed area, graph over quantities, and maps of where a higher intensity of the different elements are detected. Mappings indicate the irregular deposit to be $KMgSO_4Cl$ hydrate.

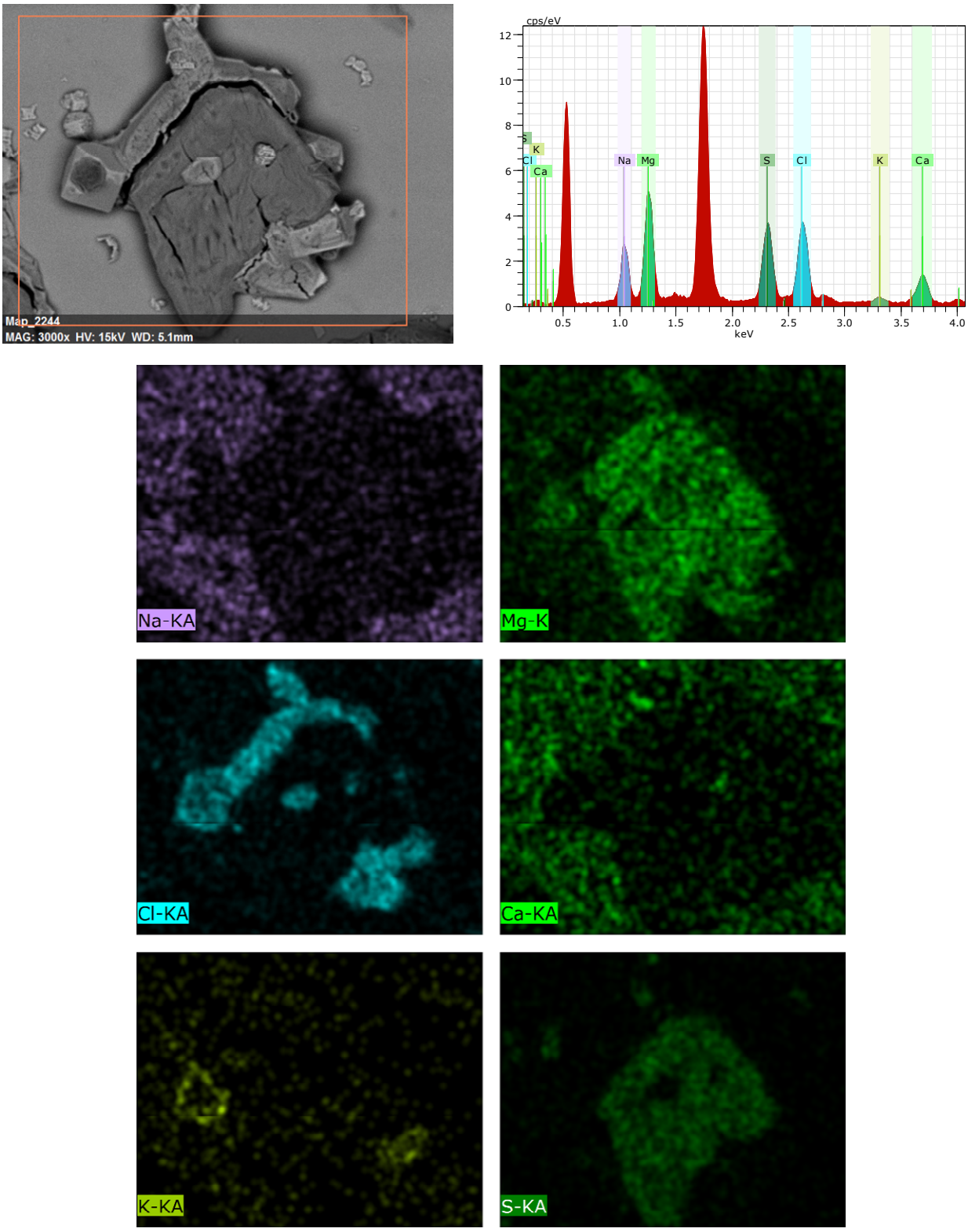

Figure 5.21: EDS analysis of U5M with an overview of the analyzed area, graph over quantities, and maps of where a higher intensity of the different elements are detected. Mappings indicate the big irregular deposit to be $MgSO_4$, surrounded by NaCl.

Table 7: Suggestions for compounds on sample surfaces exposed to seawater through SEM and EDS analysis. Rows with light-green fill are suggested composition of the small calcium- and sulfur-rich crystals observed.

Name	**Chemical formula**	**Solubility**	**Quantity**
Sodium chloride	NaCl	Soluble	All samples, in all ring deposits
Carnallite	$KMgCl_3 \cdot 6H_2O$	Soluble	Some samples only
Magnesium chloride	$MgCl_2$	Soluble	Some samples only
Gypsum (hydrate/ hemihydrate/anhydrite)	$CaSO_4 \cdot xH_2O$	semi-soluble, dependent on form	All samples, in all ring deposits
Calcium sulfide	CaS	Reacts violently with water	All samples, in all ring deposits
Calcium bisulfite	$Ca(HSO_3)_2$	Soluble	All samples, in all ring deposits
Magnesium sulfate	$MgSO_4 \cdot xH_2O$	Soluble	Some samples
Kainite	$KMgSO_4Cl \cdot xH_2O$	Soluble	Some samples

After being rinsed thoroughly with de-ionized water and dried overnight, almost all precipitates are dissolved. Only crystals consisting of calcium and sulfur and compounds containing carbon are observed, both with several different morphologies (see Figures 5.22 and 5.23). The number of small crystals observed seems to decrease, while the number of carbon-containing deposits observed seems to increase. However, there are no quantitative measures of such a change, and a conclusion cannot be made based on this perception. After rinsing, most of the small crystals have different morphology, both as flaky precipitates and small irregular crystals (Figure 5.24). Distinct hexagonal crystals are still observed to a lesser extent than before the rinsing.

As the small hexagonal crystals still are present after rinsing, further investigation through the elimination method can be done to distinguish which of the suggested composition they have. Calcium bisulfite is soluble in water, which means the crystals would dissolve during the rinsing if they had this composition, it, hence this suggestion is rejected.

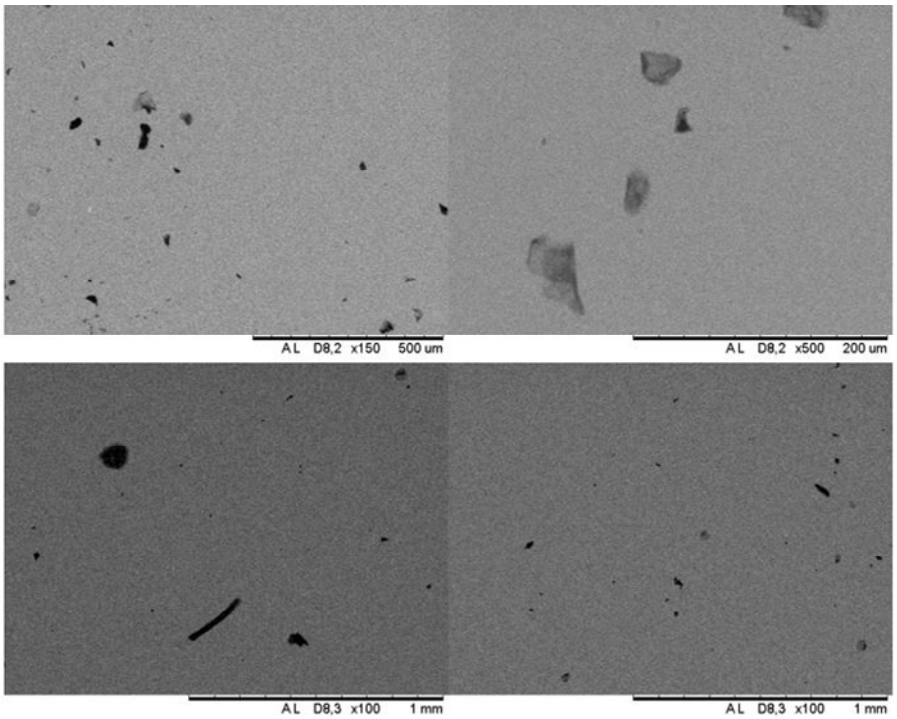

Figure 5.22: SEM images of carbon-rich deposits of different morphologies on the hydrophobic surfaces after thoroughly rinsing with de-ionized water and drying in a fume hood overnight.

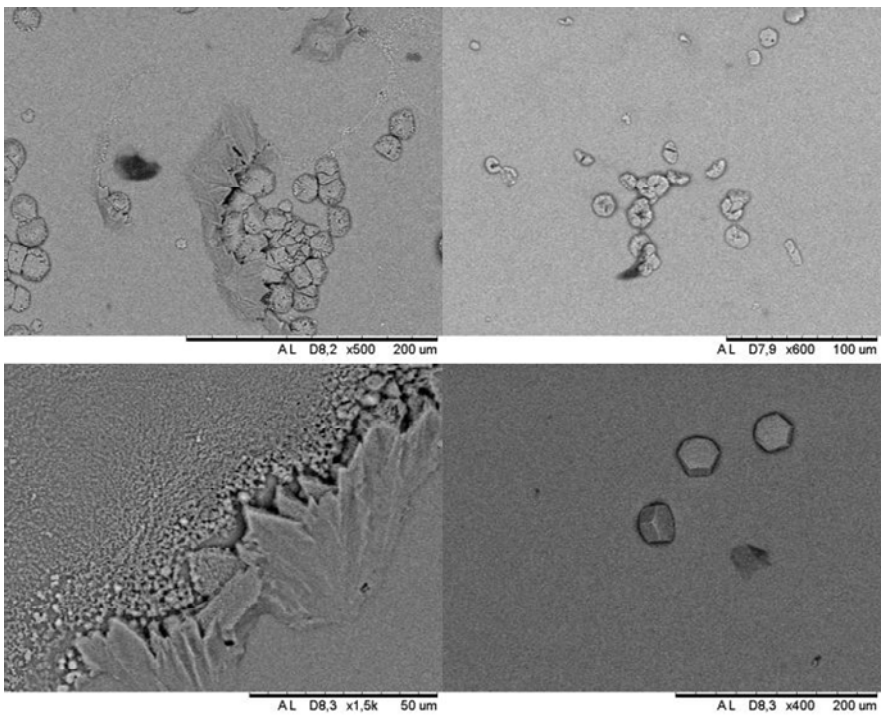

Figure 5.23: SEM images of deposits of different morphologies after rinsing thoroughly with deionized water, all with an elevated intensities of calcium and sulfur.

The same goes for calcium sulfide (CaS), as it in the presence of water, decomposes to calcium hydroxide and hydrogen sulfide (Equation 11), thus the composition of the small hexagonal crystals must be something else as they are still present after rinsing thoroughly with de-ionized water.

$$CaS(s) + 2H_2O(l) \rightarrow Ca(OH)_2(s) + H_2S(g) \quad \text{Eq.11}$$

The precipitation and transformation of the calcium sulfate phases are highly complex as they are influenced by pressure, temperature, dissolved organics, or electrolytes as well as the presence of its own or other minerals [80]. To determine which form(s) of calcium sulfate hydride/anhydrite is observed, the crystal structures must be furtherly investigated. Three crystal structures have been reported in equilibrium with water; gypsum, α-hemihydrate, and insoluble anhydrite [81]. At ambient conditions, gypsum is the most stable form. Gypsum in aqueous solution will spontaneously transform into α-hemihydrate when transition temperature is passed. It typically crystallizes in aggregates of hexagonal columns [80], as observed on the surfaces before washing in this study. As the boxes containing the samples reached over 30°C with high RH during the exposure experiment, the conditions suggest the formation of α-hemihydrate. However, after rinsing thoroughly, the $CaSO_4$ crystals have different and less distinct morphologies as seen in Figure 5.23. As of the hexagonal structuring of α-hemihydrate, the crystal lattice has room for interstitial molecules like water and thus the structure morphology easily deviates due to various impurities. Aggregates of small crystals are still observed after rinsing, however, the crystals look somewhat cracked and not as distinct as before rinsing, suggesting a phase transformation. The solubility of α-hemihydrate is higher than both anhydrite and dihydrate, but still very low (0.205 g/100 g water) and will thus induce a dissolution-precipitation reaction when exposed to water as shown in equation 12-14 [82].

$$CaSO_4 \cdot 0.5H_2O(s) \leftrightarrow Ca^{2+}(aq) + SO_4^{2-}(aq) + 0.5H_2O(l) \quad \text{Eq. 12}$$

$$CaSO_4 \cdot 2H_2O(s) \leftrightarrow Ca^{2+}(aq) + SO_4^{2-}(aq) + 2H_2O(l) \quad \text{Eq. 13}$$

$$CaSO_4 \cdot 0.5H_2O(s) + 1.5H_2O(l) \leftrightarrow CaSO_4 \cdot 2H_2O(s) \quad \text{Eq. 14}$$

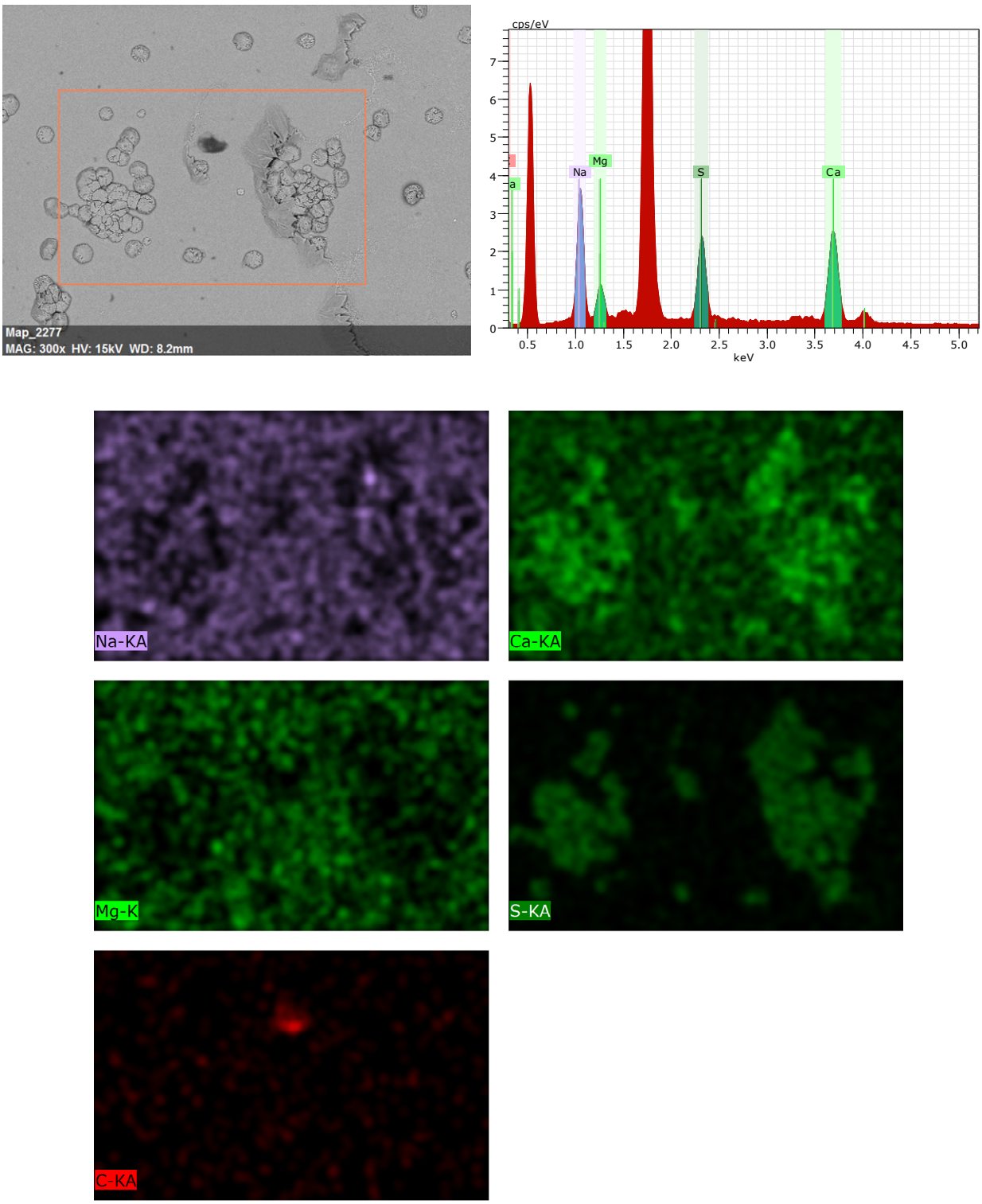

Figure 5.24: EDS analysis of seawater deposits left on the surface of F1M after a thorough rinse with de-ionized water. The analyzed area is marked by the orange rectangular. The graph presents the intensity of the chemical elements detected in the area. Maps from EDS-analysis with brighter areas indicate a higher intensity of the given chemical element. The large red peaks represent oxygen and silicon, respectively.

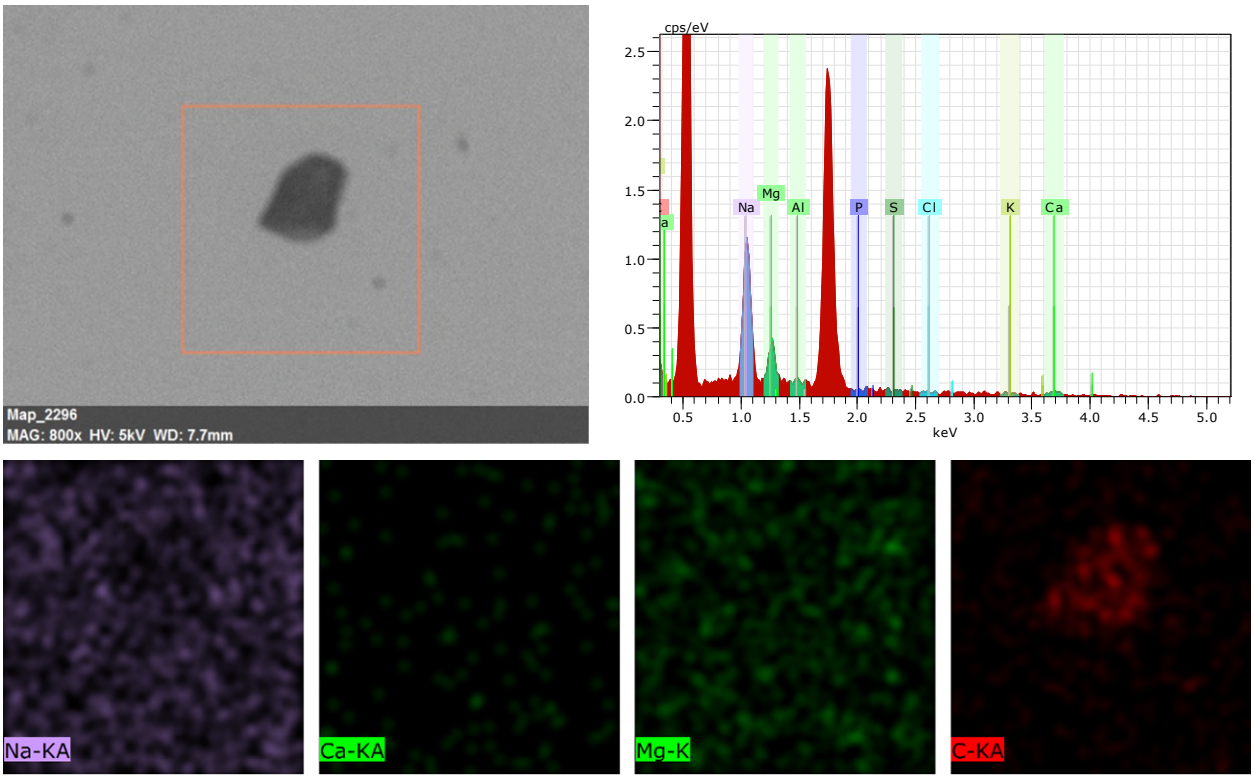

Figure 5.25: EDS analysis of an organic compound from seawater on the surface of U5M after thorough rinsing with de-ionized water. The analyzed area is marked by the orange rectangular. The graph presents the intensity of the chemical elements detected in the area. Maps from EDS-analysis with brighter areas indicate a higher intensity of the given chemical element. The large red peaks represent oxygen and silicon, respectively.

The phase transformation from α-hemihydrate to dihydrate is in line with the perception of a decrease in the amount of small crystals and an increase in bigger deposits of different morphologies containing sulfur and calcium. The transformation from distinct hexagonal aggregates to less distinct shapes are also in line with the low solubility, as only a small part of the crystals is dissolved. The center hole(s) observed before and after rinsing may be caused by substitutional impurities, resulting in irregularities in the crystal structure. A reasonable assumption considering size and charge of the ions present in seawater is magnesium. This assumption is further strengthened as the hexagonal with centered holes are only observed when they are accompanied by $MgCl_2$ as seen in Figure 5.17.

The composition of the carbon rich deposits is hard to identify as hydrogen is not detected and oxygen is present in large amounts in the substrate. However, large detected amounts of carbon in areas where the intensity of no other chemical element is detected are considered organic

deposits (Figure 5.25). As described in the literature, DOM is an effective precipitation inhibitor of the insoluble compound $CaCO_3$. No $CaCO_3$ crystals are identified in the analyzed samples, but spots with elevated calcium concentration in areas of organic deposits may indicate inhibited calcium carbonate nucleuses as described in the literature [28, 31, 36].

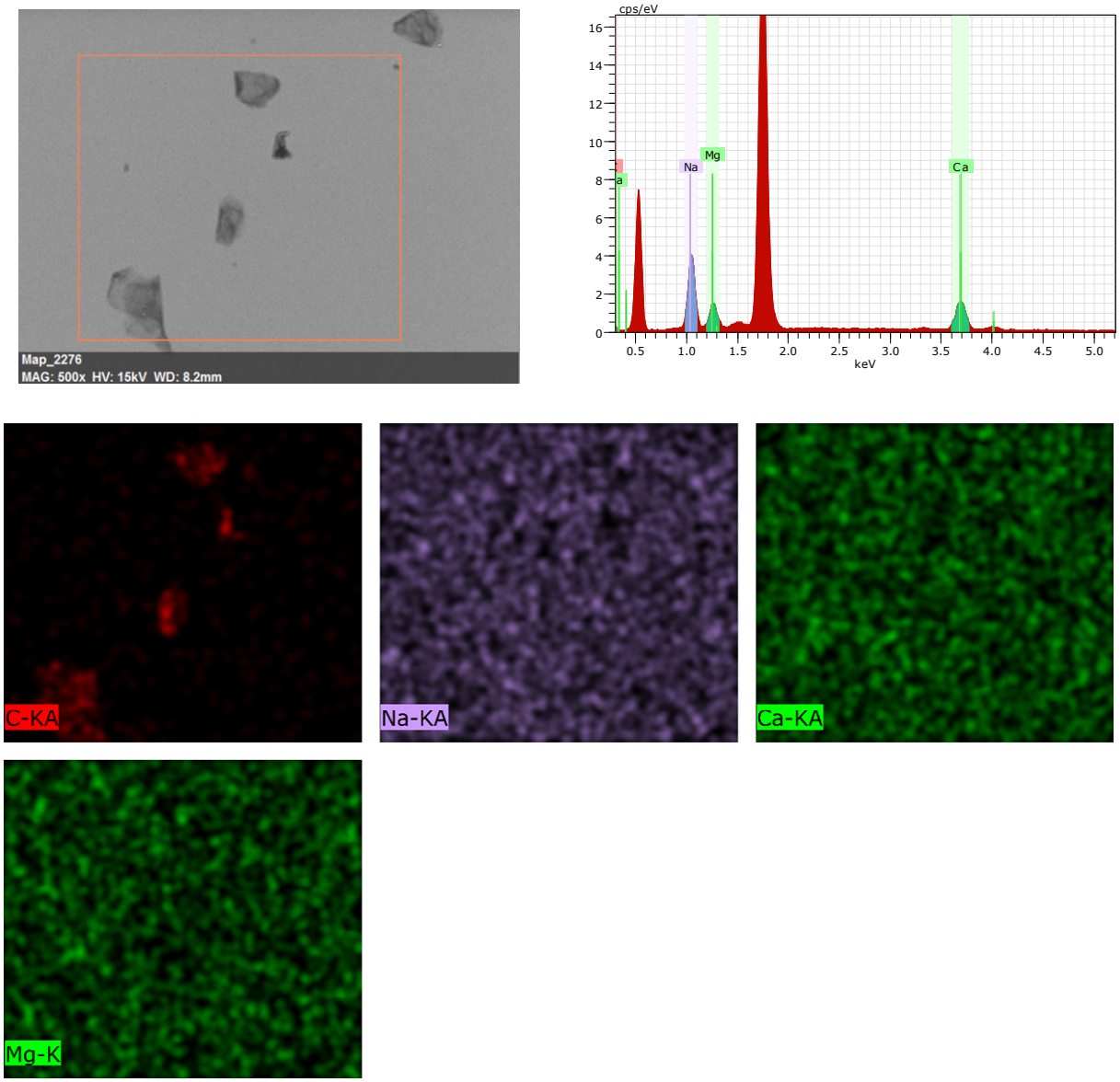

Figure 5.26: EDS analysis of an organic compound from seawater on the surface of F4M after thorough rinsing with de-ionized water. The analyzed area is marked by the orange rectangular. The graph presents the intensity of the chemical elements detected in the area. Maps from EDS-analysis with brighter areas indicate a higher intensity of the given chemical element. The large red peaks represent oxygen and silicon, respectively.

Seawater precipitates do occur on the hydrophobic samples as well as on the non-treated reference samples, and a range of deposits of different morphology are observed. At the hydrophobic surfaces, the precipitates are present as ring structures with deposits along the border and within the ring. Before rinsing with de-ionized water, cubic NaCl and hexagonal $CaSO_4$ were the most abundant compounds present. The center hole(s) in the hexagonal $CaSO_4$ crystals observed when surrounded by $MgCl_2$ are assumed to be caused by substitutional Mg^{2+} impurities. Other compounds suggested present based on the EDS analyses are: $KMgCl_3$, $MgCl_2$, $MgSO_4$, and $KMgSO_4Cl$. After thoroughly rinsing, only $CaSO_4$ and carbon-rich compounds are observed. $CaSO_4$ is still in small amounts observed as hexagonal, distinct crystals, but also as other morphologies. The hexagonal crystals are assumed to be $CaSO_4$ α-hemihydrate, which transforms into dihydrate upon rinsing with de-ionized water. The carbon-rich deposits are assumed to be organic, and thus not the insoluble calcium carbonate ($CaCO_3$). EDS analysis also indicates that the substrates with green shade are lime-soda glass and not pure silicon dioxide.

5.7 Summarizing discussion

None of the sample series were prepared and coated exactly as described by Maharjan et al. due to conflicting information in terms of a specific RH and the use of vacuum when coating and issues of roughening samples with such big surfaces. Sample series F4 and G3 were coated with TCPFOS in furnace from the same procedure and have contact angles of 99.6° ± 2.6° and 98.9° ± 2.77° measured with de-ionized water, respectively. Sample series U4, have the highest contact angle of 108.1° ± 1.3° with de-ionized water compared to the reported 105° ± 1.5° from [18]. Contact angles measured with seawater are on an average of 5.1° higher. The sample series coated with ODFDHN also led to hydrophobic surfaces with contact angles similar to those obtained for samples coated with TCPFOS. Roughening the surface to obtain microscopic torturous grooves in the micro and nanoscale does not cause increased hydrophobic abilities as assumed by Maharjan et al. On the contrary, the samples with no roughening of the surface have generally higher contact angles. One reason may be that the first abrasive used was too rough. A solution to this may be to use abrasive with smaller grains or to simply skip the first roughening step. Another possible solution is to coat the substrates with the same coating liquid several times, to ensure that the surfaces are completely coated also in the grooves.

None of the sample preparation methods or coating materials used in this study causes any substantial transmission losses (maximum 1.5%). However, salt precipitates forming on the surfaces as a result of seawater exposure greatly reduced the transmission in that specific area. The decreases occur as both uniform and wavelength-specific and vary from 1-30%. To conclude whether the decreases are caused by a reflective or absorptive effect, more information gained by for example diffuse reflectance measurements is needed.

Maharjan et al. exposed the coated surfaces to a saline solution with NaCl only. This is not directly comparable with exposure to natural seawater as it highly simplifies the precipitation chemistry. Deposits formed on the samples from seawater have a ring-like form with spots thorough the contact area as expected [53, 54]. Precipitates from seawater did form on surfaces tilted by 15 degrees, but the hydrophobic coatings restricted precipitation area to that of the droplet instead of spreading it out as for hydrophilic coatings. The complexity of the precipitation and transformation processes makes it hard to predict the potential build-up compounds, though $CaSO_4$ of different morphologies are good candidates. However, with an increased tilting of the samples, one may exceed the critical angle (not measured in this study) and reduce the number of droplets sticking to the surface and hence the number of precipitates formed.

5.8 Scalability analysis

To scale, the most cost- and time-effective method with the best results should be identified. The possibility of one method ticking all the boxes are however not likely. Firstly, the chemicals are considered. The prices per gram were on March 24th, 2020: 7.63 Euro for TCPFOS and 2.0 Euro for ODFDHN. Pricewise, one could get 4 times as much ODFDHN for the price compared to TCPFOS, and amounts used for coating are almost the same. ODFDHN is widely known in medicine as artificial blood, due to its high solute capacity for gases like oxygen and carbon dioxide as well as being both chemically and biologically inert, non-toxic and able to be transpired from the body [83-86]. However, it contains chloride, fluorine, and carbon (CFC) and is thus covered by the Kyoto Protocol and is regulated for R&D use only. TCPFOS reacts violently with water, but as this is a step of the coating process (hydrolysis) it is not a concern. Considering HSE aspects, both coatings are inert and thus assumed to pose a low risk for the environment.

In terms of roughening, the results in this study indicates a small to no difference in the hydrophobic properties of the coated surfaces as a result of the different roughening methods. Thus, the roughening step should be excluded in an up-scaled process. Below, the coating methods are evaluated in terms of scalability:

1. **Coating in furnace**

   This coating method was only done using TCPFOS as coating liquid. The use of a vacuum furnace may highly limit the sample size and will be both energy-demanding and pricy. However, a vacuum was found to not be a critical part of the process and only used for ventilation after coating. This is easily avoided by installing proper ventilation upfront. The furnace itself was only used to obtain a closed environment, which is easily obtained by other less costly and size-limiting solutions. The coating method is however not suitable for already installed windows, which highly limits the potential customer market. Timewise, the method takes about one hour, including 30min heating of the metal block, which can be streamlined.

2. **Coating with spin-coater**

   This method highly limits the sample size, and a vacuum is needed to hold the sample in place and air of 4 bar is used for ventilation. The method was used for both TCPFOS and ODFDHN and is not time-consuming with only two minutes per sample. Equipment for using this method for bigger samples as window-sizes must be custom-made and are hence costly. The method is not suitable for already installed glass without disassembly.

3. **Coating with casting knife**

   The method of coating with a casting knife is by far the cheapest and time-effective method. It can be used on both installed and non-installed samples, of all sizes. The casting knife used is appropriate for smaller sizes, but the principle is like lubricating a surface by scraping the liquid across with a flat edge. By experimenting with different tools, applied force and thickness, and uniformity of resulting coating an appropriate method should be within range.

Coating by casting knife method on unpolished glass with TCPFOS is considered the most cost- and time-effective scalable method for obtaining a hydrophobic glass surface among the methods explored in this study. The method is suitable for glass both before and after assembly.

6. Concluding remarks and future work

6.1 Conclusions

The main objective of this study was to obtain a hydrophobic self-cleaning coating for glass surfaces by coating with TCPFOS or ODFDHN.

Hydrophobic surfaces were obtained both by coating glass with TCPFOS and ODFDHN by spin coating, coating by evaporation, and by casting knife, all independent of the roughening method. Specific temperatures and RH during coating is not crucial factors in the coating processes, as all coating methods were performed in ambient conditions. The surfaces have contact angles in the range of 93-108° for de-ionized water, and averagely 5.1° higher with seawater. The transmission loss for samples coated in this work is negligible compared to pristine glass, with a maximum transmission loss of 1.5%. Unpolished samples with green shade generally had a 1% transmission loss compared to the polished samples.

However, a range of seawater precipitates formed on the hydrophobic surfaces after exposing the samples to seawater when tilted 15°, and the surfaces cannot be considered as self-cleaning. The precipitates occurred as ring-deposits, both at the border and within the ring. Temperature, RH, and presence of DOM are crucial factors for the precipitation processes of several compounds in seawater. NaCl and $CaSO_4$ of different morphologies was most abundant on the surfaces before rinsing. The latter compound and organic deposits are left on the surfaces after thoroughly rinsing with de-ionized water. Seawater precipitates decrease the transmission of the coated surfaces up to 32% by a reflective and/or absorptive effect of the incoming irradiation.

The coating method most favorable for scaling among the tested in this study is coating unpolished glass by casting knife technique with TCPFOS.

6.2 Future work

Further investigation of roughening methods to obtain superhydrophobic surfaces should be done. An investigation to identify cheaper coating materials should be conducted in terms of scaling. Known superhydrophobic materials and nanostructured surfaces should also be investigated in terms of this specific application.

Offshore exposure experiments in real conditions should be executed as temperature, RH, and irradiation all play a crucial role in the precipitation processes from seawater constituents. The exposure experiments should be done on bigger samples, and preferably on protective glass for operating PV panels offshore.

The critical tilting angle of the surfaces should be determined, and the samples should also be exposed to seawater when tilted more than this angle, to investigate the effect of precipitation formed on the surface. Methods for minimizing the critical angle should be investigated.

For a more confident identification of the seawater precipitates in terms of their morphology, more information about them is needed. The precipitates should be analyzed using XRD and other proper instruments and methods. A comprehensive study of the precipitation processes available for seawater, to see how they correlate with each other and identify their critical factors should be done.

Diffuse reflectance measurements of exposed samples should be done to conclude whether the seawater precipitates are reflecting or absorbing the incoming radiation. Such information will also be helpful to understand in which degree incoming radiation in specific ranges of wavelengths participates in the decomposition of some precipitates. Further investigation of the effect of surface roughening on transmission of different substrates should also be done.

7. References

[1] Masafumi Nakamura, S.P., Joshua Schnell and Martin Szomszor, *Navigating the Structure of Research on Sustainable Development Goals.* Web of Science Group, **(2019)**.

[2] al, N.S.L.e., *Basic Reserach Needs for Solar Energy Utilization.* **(2005)**, U.S. Department of Energy.

[3] Andersson, A., *Slik kan vindmøller til havs bli et norsk industrieventyr*, in *Sysla*. **(2019)**.

[4] Solem, B.S.,and A. Røyset, *Hvor stort areal blir berørt av vindkraftverk?* **(2019)**, Motvind Norge.

[5] Maghami, M.R., H. Hizam, C. Gomes, M.A. Radzi, M.I. Rezadad,and S. Hajighorbani, *Power loss due to soiling on solar panel: A review.* Renewable and Sustainable Energy Reviews, **(2016)**. 59: p. 1307-1316.

[6] Torres, J.P.N., S.K. Nashih, C.A.F. Fernandes,and J.C. Leite, *The effect of shading on photovoltaic solar panels.* Energy Systems, **(2018)**. 9(1): p. 195-208.

[7] Fred T. Mackenzie, A.C.D.e.a., *Seawater.* Encyclopædia Britannica, Inc. .

[8] Sisodia, A.K.,and R.k. Mathur, *Impact of bird dropping deposition on solar photovoltaic module performance: a systematic study in Western Rajasthan.* Environmental Science and Pollution Research, **(2019)**. 26(30): p. 31119-31132.

[9] Goldstein, D.L.,and E. Skadhauge, *CHAPTER 11 - Renal and Extrarenal Regulation of Body Fluid Composition*, in *Sturkie's Avian Physiology (Fifth Edition)*, G.C. Whittow, Editor. **(2000)**, Academic Press: San Diego. p. 265-297.

[10] Jensen, A., *Present and future needs for algae and algal products.* Hydrobiologia, **(1993)**. 260(1): p. 15-23.

[11] Al-Housani, M., Y. Bicer,and M. Koç, *Experimental investigations on PV cleaning of large-scale solar power plants in desert climates: Comparison of cleaning techniques for drone retrofitting.* Energy Conversion and Management, **(2019)**. 185: p. 800-815.

[12] Shafir, S., I. Halperin,and B. Rinkevich, *Toxicology of Household Detergents to Reef Corals.* Water, Air, & Soil Pollution, **(2014)**. 225(3): p. 1890.

[13] Cann, H.M.,and H.L. Verhulst, *Toxicity of Household Soap and Detergent Products and Treatment of Their Ingestion.* American Journal of Diseases of Children, **(1960)**. 100(2): p. 287-290.

[14] Mokhtarimehr, M., M. Pakshir, A. Eshaghi,and M.H. Shariat, *Super-hydrophilic property of vanadium doped TiO_2 SiO_2 solgel derived thin film.* Thin Solid Films, **(2013)**. 532: p. 123-126.

[15] Fujishima, A., X. Zhang,and D. Tryk, *TiO2 photocatalysis and related surface phenomena.* Surf. Sci. Rep., **(2008)**. 63(12): p. 515-582.

[16] Binas, V., D. Venieri, D. Kotzias,and G. Kiriakidis, *Modified TiO2 based photocatalysts for improved air and health quality.* Journal of Materiomics, **(2017)**. 3(1): p. 3-16.

[17] Ohama, Y.,and D. Van Gemert, *Application of Titanium Dioxide Photocatalysis to Construction Materials : State-of-the-Art Report of the RILEM Technical Committee 194-TDP*. **(2011)**, Springer Netherlands : Imprint: Springer: Dordrecht.

[18] Maharjan, S., K.-S. Liao, A.J. Wang, K. Barton, A. Haldar, N.J. Alley, H.J. Byrne,and S.A. Curran, *Self-cleaning hydrophobic nanocoating on glass: A scalable manufacturing process.* Materials Chemistry and Physics, **(2020)**. 239: p. 122000.

[19] Fraker, C.A., A.J. Mendez, L. Inverardi, C. Ricordi,and C.L. Stabler, *Optimization of perfluoro nano-scale emulsions: The importance of particle size for enhanced oxygen*

transfer in biomedical applications. Colloids and Surfaces B: Biointerfaces, **(2012)**. 98: p. 26-35.
[20] Solar, S. *Learning center, Theory of Operation of PV/ Solar Cell*. Available from: https://www.samlexsolar.com/learning-center/solar-cell-module-array.aspx.
[21] Chen, K.P.O.D.a.X., *Temperature dependence of semiconductor band gaps*. **(1991)**.
[22] Sarver, T., A. Al-Qaraghuli,and L.L. Kazmerski, *A comprehensive review of the impact of dust on the use of solar energy: History, investigations, results, literature, and mitigation approaches.* Renewable and Sustainable Energy Reviews, **(2013)**. 22: p. 698-733.
[23] Sayyah, A., M.N. Horenstein,and M.K. Mazumder, *Energy yield loss caused by dust deposition on photovoltaic panels.* Solar Energy, **(2014)**. 107: p. 576-604.
[24] Ramli, M.A.M., E. Prasetyono, R.W. Wicaksana, N.A. Windarko, K. Sedraoui,and Y.A. Al-Turki, *On the investigation of photovoltaic output power reduction due to dust accumulation and weather conditions.* Renewable Energy, **(2016)**. 99: p. 836-844.
[25] Amon, R.M.W., G. Budéus,and B. Meon, *Dissolved organic carbon distribution and origin in the Nordic Seas: Exchanges with the Arctic Ocean and the North Atlantic.* Journal of Geophysical Research: Oceans, **(2003)**. 108(C7): p. n/a-n/a.
[26] Dennis A. Hansell, C.A.C., *Biogeochemistry of Marine Dissolved Organic Matter*. **(2002)**, Amsterdam, Boston, London, New York, Oxford, Paris, San Diego, San Fransisco, Singapore, Sydney and Tokyo: Academic press, an Elsevier Science imprint. p. 64-65.
[27] Van Mooy, B.A.S., A. Krupke, S.T. Dyhrman, H.F. Fredricks, K.R. Frischkorn, J.E. Ossolinski, D.J. Repeta, M. Rouco, J.D. Seewald,and S.P. Sylva, *Major role of planktonic phosphate reduction in the marine phosphorus redox cycle.* Science, **(2015)**. 348(6236): p. 783-785.
[28] Chave, K.E.,and E. Suess, *Calcium carbonate saturation in seawater: effects of dissolved organic matter.* Limnology and Oceanography, **(1970)**. 15(4): p. 633-637.
[29] Babel, M.,and B. Schreiber, *9.17-Geochemistry of evaporites and evolution of seawater.* Treatise on geochemistry, **(2014)**: p. 483-560.
[30] Bock, E., *On the solubility if anhydrous calcium sulphate and of gypsum in concentrated solutions of sodium chloride at 25 C, 30 C, 40 C and 50 C.* Canadian Journal of Chemistry, **(1961)**. 39(9): p. 1746-1751.
[31] Simkiss, K., *The inhibitory effects of some metabolites on the precipitation of calcium carbonate from artificial and natural sea water.* ICES Journal of Marine Science, **(1964)**. 29(1): p. 6-18.
[32] Dean, J.A.,and N.A. Lange, *Lange's handbook of chemistry*. 14th ed. ed. **(1992)**, New York: McGraw-Hill.
[33] Donnay, J.D.H.,and A. American Crystallographic, *Crystal data : determinative tables*. 2nd edition. ed. ACA monograph. Vol. 5. **(1963)**: American Crystallographic Association.
[34] Levin, E.M., *Phase diagrams for ceramists*. **(1964)**: Columbus, Ohio: American Ceramic Society.
[35] Yang, X., V. Nedela, J. Runštuk, G. Ondrušková, J. Krausko, Ľ. Vetráková,and D. Heger, *Evaporating brine from frost flowers with electron microscopy and implications for atmospheric chemistry and sea-salt aerosol formation.* Atmospheric Chemistry and Physics, **(2017)**. 17: p. 6291-6303.
[36] Suwono, A., Y.S. Indartono, M. Irsyad,and I. Al-Afkar, *Application of calcium chloride as an additive for secondary refrigerant in the air conditioning system type chiller to*

minimized energy consumption. IOP Conference Series: Materials Science and Engineering, **(2015)**. 88: p. 012035.
[37] Hunter, R.J., *Introduction to modern colloid science.* **(1993)**, Oxford: Oxford University Press.
[38] Marchand, A., J.H. Weijs, J.H. Snoeijer,and B. Andreotti, *Why is surface tension a force parallel to the interface?(Author abstract).* American Journal of Physics, **(2011)**. 79(10): p. 999.
[39] Fowkes, F.M., *Determination of interfacial tensions, contact angles, and dispersion forces in surfaces by assuming additivity of intermolecular interactions in surfaces [5]*. Journal of Physical Chemistry, **(1962)**. 66(2): p. 382.
[40] London, F., *The general theory of molecular forces.* Transactions of the Faraday Society, **(1937)**. 33: p. 8-26.
[41] Hare, E.F., E.G. Shafrin,and W.A. Zisman, *Properties of Films of Adsorbed Fluorinated Acids.* The Journal of Physical Chemistry, **(1954)**. 58(3): p. 236-239.
[42] Nishino, T., M. Meguro, K. Nakamae, M. Matsushita,and Y. Ueda, *The Lowest Surface Free Energy Based on −CF3 Alignment.* Langmuir, **(1999)**. 15(13): p. 4321-4323.
[43] Lemal, D.M., *Perspective on Fluorocarbon Chemistry.* The Journal of Organic Chemistry, **(2004)**. 69(1): p. 1-11.
[44] Zhang, J., M.K. Borg, K. Sefiane,and J.M. Reese, *Wetting and evaporation of salt-water nanodroplets: A molecular dynamics investigation.* Physical Review E, **(2015)**. 92(5): p. 052403.
[45] Zielecka, M., *Hydrophobic and hydrophilic silicone-containing systems for external antisoiling protection of porous building materials.* **(2003)**. 86: p. 187-190.
[46] Zhang, L.,and J. Zhi, *DURABLE HYDROPHILIC-SUPER-HYDROPHOBIC BIPOLAR SELF-CLEANING COMPOSITE FILM, AND PREPARATION METHOD THEREFOR.* **(2018)**.
[47] Co., R.-H.I. *Information on Contact Angle* **(2020)**; Available from: http://www.ramehart.com/contactangle.htm.
[48] Fujishima, A., T.N. Rao,and D.A. Tryk, *Titanium dioxide photocatalysis.* Journal of Photochemistry & Photobiology, C: Photochemistry Reviews, **(2000)**. 1(1): p. 1-21.
[49] Deegan, R.D., O. Bakajin, T.F. Dupont, G. Huber, S.R. Nagel,and T.A. Witten, *Capillary flow as the cause of ring stains from dried liquid drops.* Nature, **(1997)**. 389(6653): p. 827-829.
[50] Fukai, J., H. Ishizuka, Y. Sakai, M. Kaneda, M. Morita,and A. Takahara, *Effects of droplet size and solute concentration on drying process of polymer solution droplets deposited on homogeneous surfaces.* International Journal of Heat and Mass Transfer, **(2006)**. 49(19): p. 3561-3567.
[51] Shin, D.H., S.H. Lee, J.-Y. Jung,and J.Y. Yoo, *Evaporating characteristics of sessile droplet on hydrophobic and hydrophilic surfaces.* Microelectronic Engineering, **(2009)**. 86(4): p. 1350-1353.
[52] Orejon, D., K. Sefiane,and M.E.R. Shanahan, *Stick–Slip of Evaporating Droplets: Substrate Hydrophobicity and Nanoparticle Concentration.* Langmuir, **(2011)**. 27(21): p. 12834-12843.
[53] Uno, K., K. Hayashi, T. Hayashi, K. Ito,and H. Kitano, *Particle adsorption in evaporating droplets of polymer latex dispersions on hydrophilic and hydrophobic surfaces.* Colloid and Polymer Science, **(1998)**. 276(9): p. 810-815.

[54] Nguyen, T.A.H., M.A. Hampton,and A.V. Nguyen, *Evaporation of Nanoparticle Droplets on Smooth Hydrophobic Surfaces: The Inner Coffee Ring Deposits.* The Journal of Physical Chemistry C, **(2013)**. 117(9): p. 4707-4716.

[55] Trapani, K.,and D.L. Millar, *Proposing offshore photovoltaic (PV) technology to the energy mix of the Maltese islands.* Energy Conversion and Management, **(2013)**. 67: p. 18-26.

[56] Trapani, K., D.L. Millar,and H.C.M. Smith, *Novel offshore application of photovoltaics in comparison to conventional marine renewable energy technologies.* Renewable Energy, **(2013)**. 50: p. 879-888.

[57] Sabah, K.,and S.N. Faraj, *Self-cleaning solar panels to avoid the effects of accumulated dust on solar panes transmittance.* International Journal of Science and Research, **(2013)**. 2: p. 246-247.

[58] Syafiq, A., A.K. Pandey, N.N. Adzman,and N.A. Rahim, *Advances in approaches and methods for self-cleaning of solar photovoltaic panels.* Solar Energy, **(2018)**. 162: p. 597-619.

[59] Daoud, W.A., *Self-cleaning materials and surfaces : a nanotechnology approach.* **(2013)**, Wiley: Chichester, West Sussex, United Kingdom.

[60] Asahi, R., T. Morikawa, H. Irie,and T. Ohwaki, *Nitrogen-Doped Titanium Dioxide as Visible-Light-Sensitive Photocatalyst: Designs, Developments, and Prospects.* Chem. Rev., **(2014)**. 114(19): p. 9824-9852.

[61] Kandregula, G., D. Chinthakuntla, K. Rao, C. Chakra,and V. Rajendar, *Green Synthesis of TiO 2 Nanoparticles Using Hibiscus Flower Extract*. **(2014)**.

[62] AS, P.N., *Pilkington Active™ i kystnære og marine miljøer*. **(2018)**: p. 1.

[63] Dodiuk, H., P.F. Rios, A. Dotan, S. Kenig, G. Marom,and A.J. Domb, *Hydrophobic and self-cleaning coatings.* Polymers for Advanced Technologies, **(2007)**. 18(9): p. 746-750.

[64] Han, D.,and S.Y. Moon, *Development of superhydrophobic surface on glass substrate by multi-step atmospheric pressure plasma treatment.* Thin Solid Films, **(2015)**. 587: p. 34-38.

[65] He, T., Y. Wang, Y. Zhang, Q. lv, T. Xu,and T. Liu, *Super-hydrophobic surface treatment as corrosion protection for aluminum in seawater.* Corrosion Science, **(2009)**. 51(8): p. 1757-1761.

[66] Murase, H.,and T. Fujibayashi, *Characterization of molecular interfaces in hydrophobic systems.* Prog. Org. Coat., **(1997)**. 31(1-2): p. 97-104.

[67] Liu, T., S. Chen, S. Cheng, J. Tian, X. Chang,and Y. Yin, *Corrosion behavior of super-hydrophobic surface on copper in seawater.* Electrochimica Acta, **(2007)**. 52(28): p. 8003-8007.

[68] Yu, D., J. Tian, J. Dai,and X. Wang, *Corrosion resistance of three-layer superhydrophobic composite coating on carbon steel in seawater.* Electrochimica Acta, **(2013)**. 97: p. 409-419.

[69] Kalantar-zadeh, K.,and B. Fry, *Nanotechnology-Enabled Sensors.* **(2008)**, Springer US : Imprint: Springer: New York, NY.

[70] Brandon, D.G.,and W.D. Kaplan, *Microstructural characterization of materials*. **(1999)**, Chichester: Wiley. p. Chapter 4 & 5.

[71] Carrara, S., *Towards new efficient nanostructured hybrid materials for ECL applications.* **(2017)**, Université de Strasbourg.

[72] Binnig, G., C.F. Quate,and C. Gerber, *Atomic Force Microscope.* Physical Review Letters, **(1986)**. 56(9): p. 930-933.
[73] Matthews, J.A., *Spectrophotometer*. **(2014)**. p. 1040-1040.
[74] Baker, R.W., *Membrane Technology and Applications*. **(2012)**, Chichester, UK: Chichester, UK: John Wiley & Sons, Ltd. p. 98-99.
[75] Crawford, R.J.,and E.P. Ivanova, *Chapter Three - The Design of Superhydrophobic Surfaces*, in *Superhydrophobic Surfaces*, R.J. Crawford and E.P. Ivanova, Editors. **(2015)**, Elsevier: Amsterdam. p. 27-49.
[76] Hossein, M.B.a.B.G., *Optical spectroscopy of sodium silicate glasses prepared with nano- and micro sized iron oxide particles.* Processing and Application of Ceramics, **(2013)**. 7(3).
[77] Teixeira, M.I.,and L.V.E. Caldas, *Dosimetric properties of various colored commercial glasses.* Applied Radiation and Isotopes, **(2002)**. 57(3): p. 407-413.
[78] Sakaguchi, K.,and T. Uchino, *Compositional dependence of infrared absorption of iron-doped silicate glasses.* Journal of Non-Crystalline Solids, **(2007)**. 353(52): p. 4753-4761.
[79] El Khiati, N., R. Gy,and E. Le Bourhis, *Silica-soda-lime glass compositions and their applications*. **(2009)**.
[80] Freyer, D.,and W. Voigt, *Crystallization and Phase Stability of $CaSO_4$ and $CaSO_4$-based Salts.* Monatshefte fuer Chemie/Chemical Monthly, **(2003)**. 134: p. 693-719.
[81] American, M., R. Foundry Company, D. Development,and W. United States. Office of Saline, *An investigation of the solubility of calcium sulfate in sea water concentrates at temperatures from ambient to 65©® C*. **(1966)**: Washington. D.C.: U.S. Dept. of the Interior; for sale by the Suprintendent of Documents, U.S. Govt. Print. Off.
[82] Kunio, I., *Bone Substitute Fabrication Based on Dissolution-Precipitation Reactions.* Materials, **(2010)**. 3.
[83] Rubtsov, N.M., B.S. Seplyarskii, A.G. Tarasov, G.I. Tsvetkov,and V.I. Chernysh, *Suppression of the ignition of coal powders in the presence of oxygen and natural gas with small additives of octadecafluorodecahydronaphthalene vapour.* Mendeleev Communications, **(2012)**. 22(3): p. 154-156.
[84] Afzal, J., S.R. Ashlock, B.M. Fung,and E.A. O'Rear, *Interaction between perfluoro chemicals and oxygen in phosphatidylcholine vesicles.* The Journal of Physical Chemistry, **(1986)**. 90(13): p. 3019-3022.
[85] Parhami, P.,and B.M. Fung, *Fluorine-19 relaxation study of perfluoro chemicals as oxygen carriers.* The Journal of Physical Chemistry, **(1983)**. 87(11): p. 1928-1931.
[86] Tamimi, F., P. Comeau, D. Le Nihouannen, Y.L. Zhang, D.C. Bassett, S. Khalili, U. Gbureck, S.D. Tran, S. Komarova,and J.E. Barralet, *Perfluorodecalin and bone regeneration.* European Cells and Materials, **(2012)**. 25: p. 22-36.

8. Appendix

8.1 Safety sheets chemicals

Octodecafluorodecahydronapthalene (ODFDHN)

No safety symbols.

Personal Protective Equipment: Eyeshields, faceshields, gloves,

RIDADR: NONH for all modes of transport

WGK Germany: 3

RTECS: QJ3175000

Flash Point(C): >100°C

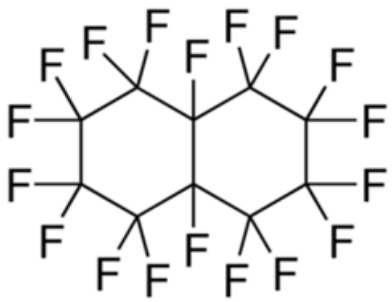

Figure 8.1: Chemical structure of ODFDHN, reproduced from Sigma-Aldrich.

Trichloro(1H,1H,2H,2H-perfluoroctyl)silane (TCPFOS)

Symbol: GHS05

Signal word: Danger

Hazard statements: H314

Precautionary statements: P280-P305 + P351 + P338-P310

Supplemental Hazard Statements: Reacts violently with water.

Personal Protective Equipment: Face shield, gloves and goggle

RIDADR: UN 2987 8 / PGII

WGK Germany: 3

Flash Point(C): 87°C

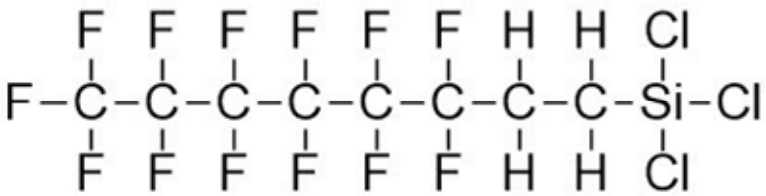

Figure 8.2: Chemical structure of TCPFOS.

8.2 Standard deviation

Calculation of standard deviation for contact angle measurements:

Standard deviations:

$$\sigma = \sqrt{\frac{1}{N}\sum_{i=1}^{N}(x_i - \bar{\mathbf{x}})^2}$$

8.3 Salinity of seawater samples

Table 8: Measured weight and data calculated for the salinity of the seawater samples.

Sample location	Weight 10mL seawater excluding plastic container (g)	Weight dry salt, excluding plastic container (g)	Weight percent salt calculated (%)
Aksnes	9.956	0.357	3.59
Bømlo	9.805	0.341	3.48
Kvalsvik	9.803	0.3488	3.56
Karmsundet	9.663	0.1958	2.03

8.4 Development of RH VS temperature over time

Table 9: Raw data and calculated average of RH and temperature development when heating the VACUtherm furnace for 23 minutes.

Time (minutes)	Sensor 1		Sensor 2		Sensor 3		Average	
	RH (%)	Temp (°C)	RH(%)	Temp (°C)	RH(%)	Temp (°C)	RH(%)	Temp (°C)
0	29	21.3	30	21.2	29	21.5	29	21.3
1	29	21.4	30	21.4	29	21.8	29	21.5
2	29	21.6	29	21.5	29	21.9	29	21.7
3	28	21.7	29	21.6	29	22.0	29	21.8
4	28	21.8	28	21.8	29	22.1	28	21.9
5	28	21.9	28	21.9	28	22.1	28	22.0
6	27	22.0	28	21.9	28	22.2	28	22.0
7	27	22.2	28	22.1	27	22.4	27	22.2
8	27	22.6	27	22.5	25	22.8	26	22.6
9	25	23.2	25	23.1	25	23.2	25	23.2
10	25	24.1	25	23.8	25	23.9	25	23.9
11	24	25.0	24	24.6	23	24.8	24	24.8
12	22	25.9	23	25.6	23	25.8	23	25.8
13	22	27.0	22	26.6	22	26.9	22	26.8
14	18	28.2	19	27.6	19	28.1	19	28.0
15	18	29.2	18	28.5	18	29.1	18	28.9
16	17	30.2	17	29.5	17	29.9	17	29.9
17	16	31.2	16	30.4	15	31.0	16	30.9
18	16	31.9	15	31.1	17	31.8	16	31.6
19	13	32.8	16	32.1	15	32.5	15	32.5
20	12	33.5	14	32.7	14	33.3	13	33.2
21	12	34.3	14	33.4	12	34.1	13	33.9
22	11	35.0	12	34.2	12	34.8	12	34.7
23	10	35.5	12	34.6	12	35.3	11	35.1

8.5 Temperatures and RH for coating by vapor in furnace

Table 10: Temperature and relative humidity in the VACUtherm furnace at the beginning of the coating process, after 10 minutes and 20 minutes respectively.

F1	Temp (°C)	RH(%)	Temp (°C)	RH (%)	Temp (°C)	RH (%)
H1	23.1	14	24.2	10	25.5	10
H2	23.1	14	24.3	10	26.2	10
H3	23.4	14	26.5	10	28.9	10
Average	23.2	14	25	10	26.9	10
F4						
H1	26.9	15	28.1	11	29.1	10
H2	27.4	14	28.6	10	29.8	10
H3	27.3	16	28.5	10	31.1	10
Average	27.2	15	28.4	10.3	30	10
G3						
H1	24.2	16	25.4	14	26.2	14
H2	24.4	16	26	14	27.1	15
H3	24.8	16	27.7	15	28.3	11
Average	24.5	16	26.4	14.3	27.2	13.3
U3						
H1	26.8	21	-	-	34.8	10
H2	27.4	21	-	-	35.9	10
H3	27.2	20	-	-	36.5	10
Average	27.1	20.7	-	-	35.7	10

8.6 USB-microscopy photos

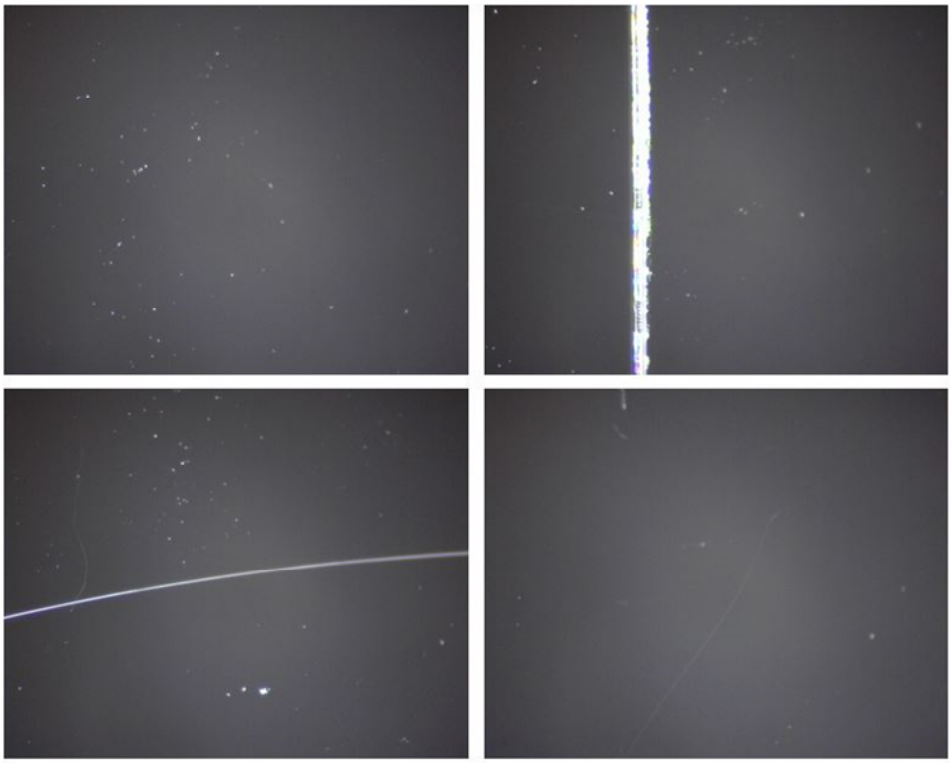

Figure 8.3: USB-microscopy photos of reference sample B2 at x778 magnification.

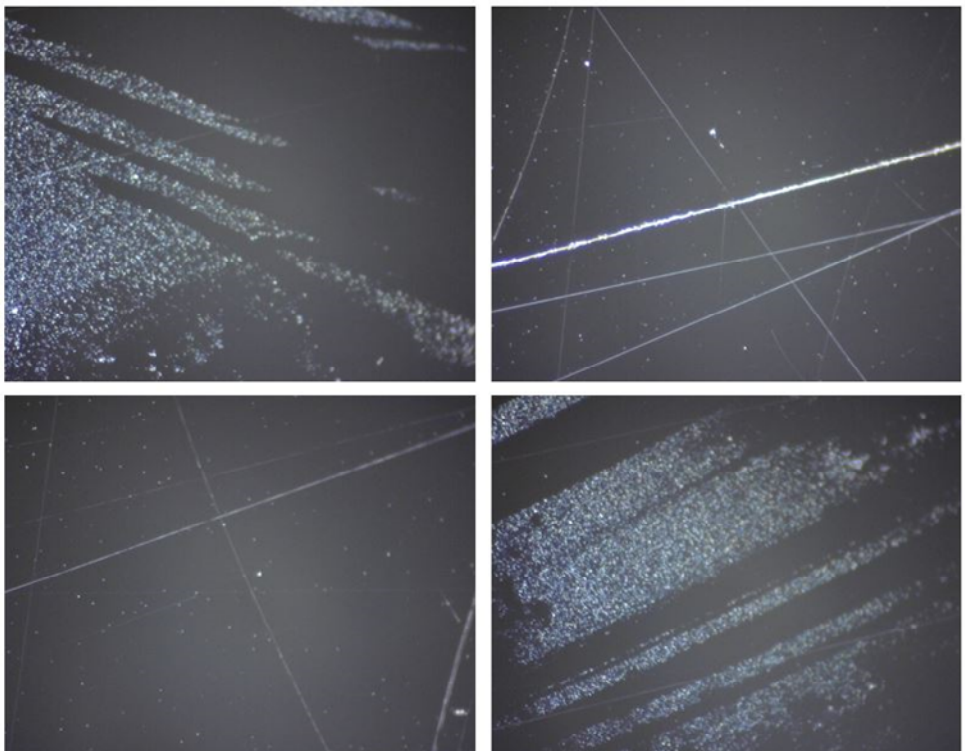

Figure 8.4: USB-microscopy photos of sample F1L, polished by hand with 0.1 µm diamond suspension with visible suspension remains at x778 magnification.

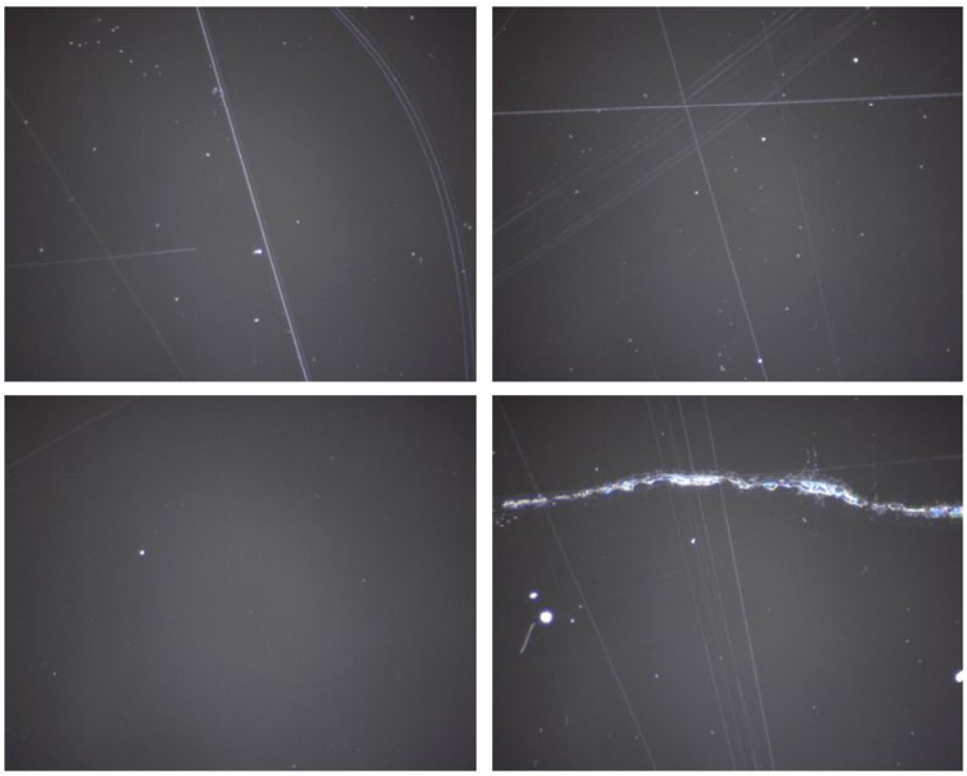

Figure 8.5: USB-microscopy photo of sample G2, roughened with coarse abrasive (5 µm), at x778 magnification.

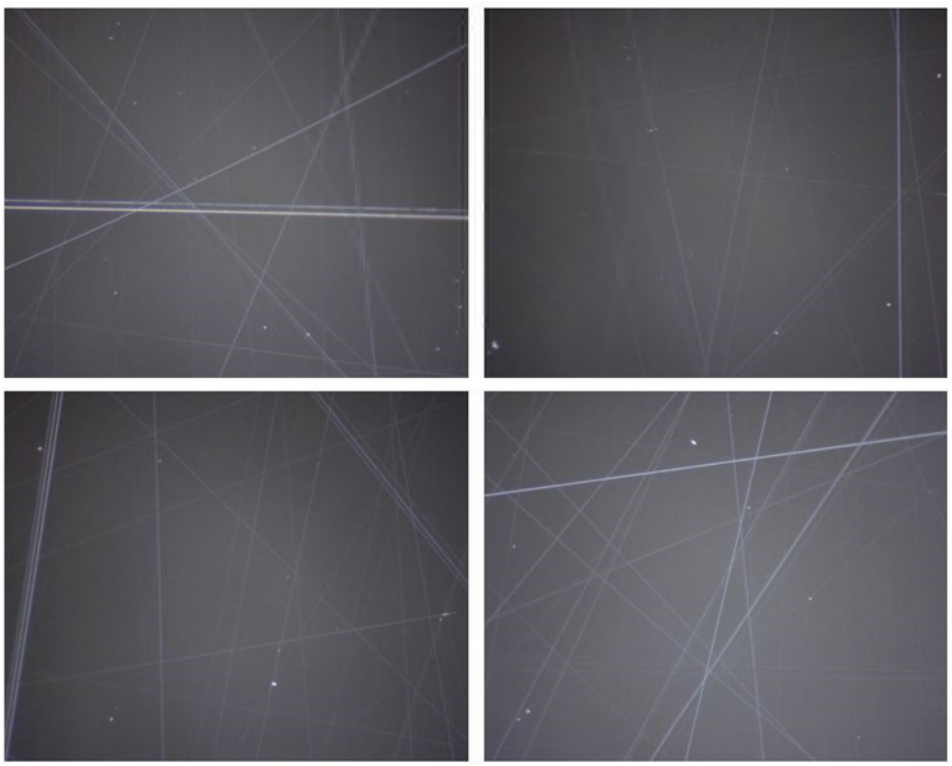

Figure 8.6: Sample F4H, roughened by polishing papers (1, 0.3, 0.1 and 0.05 µm) at x778 magnification.

8.7 Contact Angle Measurements

Table 11: Overview of measured contact angle (°) with seawater and de-ionized water for all samples and series.

Name sample series	Name sample	Average w/deionized water	Standard deviation	Average w/ seawater	Standard deviation	Series average w/deionized water	Series average w/ seawater
U1	U1L	102.7	2.5	107.6	2.1	103.8 ± 1.55	106.5 ± 1.55
	U1M	103.7	3.3	106.4	4.0		
	U1H	105.1	1.4	105.6	1.1		
U2	U2L	108.4	1.7	111.4	1.8	104.0 ± 1.69	108.2 ± 1.47
	U2M	103.0	1.9	107.4	2.5		
	U2H	100.7	5.0	105.8	2.2		
U3	U3L	102.1	1.7	107.0	3.2	102.2 ± 1.29	109.2 ± 1.91
	U3M	101.1	1.9	108.1	2.2		
	U3H	103.4	1.4	112.3	5.5		
U4	U4L	104.2	2.4	110.1	2.9	108.1 ± 1.28	110.2 ± 1.83
	U4M	109.4	0.3	107.3	0.6		
	U4H	110.7	2.2	113.1	6.6		
U5	U5L	103.3	2.3	104.6	0.7	103.3 ± 1.81	105.6 ± 1.29
	U5M	104.2	3.9	105.3	1.5		
	U5H	102.3	3.6	106.9	2.8		
U6	U6L	107.7	2.9	109.8	0.7	104.7 ± 1.85	105.5 ± 0.98
	U6M	104.0	5.4	102.6	0.5		
	U6H	102.3	2.0	104.1	1.7		
F1	F1L	94.8	7.9	103.3	3.3	93.5 ± 2.66	102.5 ± 1.83
	F1M	94.2	9.8	103.2	2.8		
	F1H	91.5	3.6	101.0	4.0		
F2	F2L	13.7	2.7	33.0	3.0	13.5 ± 2.02	30.2 ± 1.94
	F2M	15.7	4.5	34.0	5.1		
	F2H	11.6	5.1	23.7	3.2		
F4	F4L	98.2	8.6	108.3	0.8	99.6 ± 2.5	105.8 ± 1.34
	F4M	99.8	6.5	101.3	4.3		
	F4H	100.8	3.6	107.9	0.3		
F5	F5L	101	1.4	101.5	6.7	98.9 ± 1.51	102.8 ± 2.0
	F5M	97.9	4.1	106.1	4.1		
	F5H	97.8	1.3	100.8	1.2		
F6	F6L	104.6	1.7	106.6	2.2	101.1 ± 1.48	105.9 ± 1.15
	F6M	100.5	0.9	107.1	0.5		
	F6H	98.2	4.0	103.9	1.3		
G3	G3L	103.1	3.9	107.0	4.6	98.8 ± 2.77	100.3 ± 2.20
	G3M	95.7	9.8	89.6	5.6		
	G3H	97.5	9.3	104.3	4.3		
Pilk	Pilk1	59.1	10.6	75.2	2.5	67.8	75.6
	Pilk2	76.4	1.9	75.9	6.5		

8.8 Temperature and relative humidity during exposure studies

Table 12: Temperature and RH for box1 under exposure period. Containing H-samples.

Box 1	kl 05:00		kl 11:00		kl 17:00		kl 23:00	
	Temp	RH	Temp	RH	Temp	RH	Temp	RH
March 13th	19.9	73	20.8	99	30.5	94	22.2	99
March 14th	21.7	99	20.6	99	20.2	99	19.9	99
March 15th	19.8	99	20.1	99	21.9	99	21.1	99
March 16th	19.4	99	20.7	90	21.5	89	19.5	99
March 17th	19.1	99	20.2	97	20.3	99	19.8	99
March 18th	18.8	96	20	90	22.5	84	20.5	95
March 19th	19.7	96	19.8	96	21.1	95	19.7	94

Table 13: Temperature and RH for box 2 under exposure period. Containing M samples and Pilk2.

Box 2	kl 05:00		kl 11:00		kl 17:00		kl 23:00	
	Temp	RH	Temp	RH	Temp	RH	Temp	RH
March 13th	19.9	76	19.9	99	29.8	92	22.4	99
March 14th	20.8	99	20.8	99	20.4	99	20.2	99
March 15th	19.9	99	20.1	99	22.2	99	21.2	99
March 16th	19.9	99	20.9	90	21.7	90	19.9	99
March 17th	19.4	97	20.7	99	20.7	99	20	99
March 18th	19.1	95	20.4	91	22.9	81	20.8	95
March 19th	20	99	20	96	21.5	95	20	97

8.9 SEM of salt crystals from evaporated water samples

Raw material from EDS-analysis, mapping and photos. All mappings include an overview photo with an orange rectangle marking the analyzed area and a graph illustrating measured intensity of the chemical elements present in the area. Then follows a photo with all elements and their denoted color merged, sometimes quite messy. At last is a map for each chemical element present with substantial intensity, with brighter colors in areas with elevated concentrations.

8.9.1 EDS analysis of uncoated sample surfaces after seawater exposure

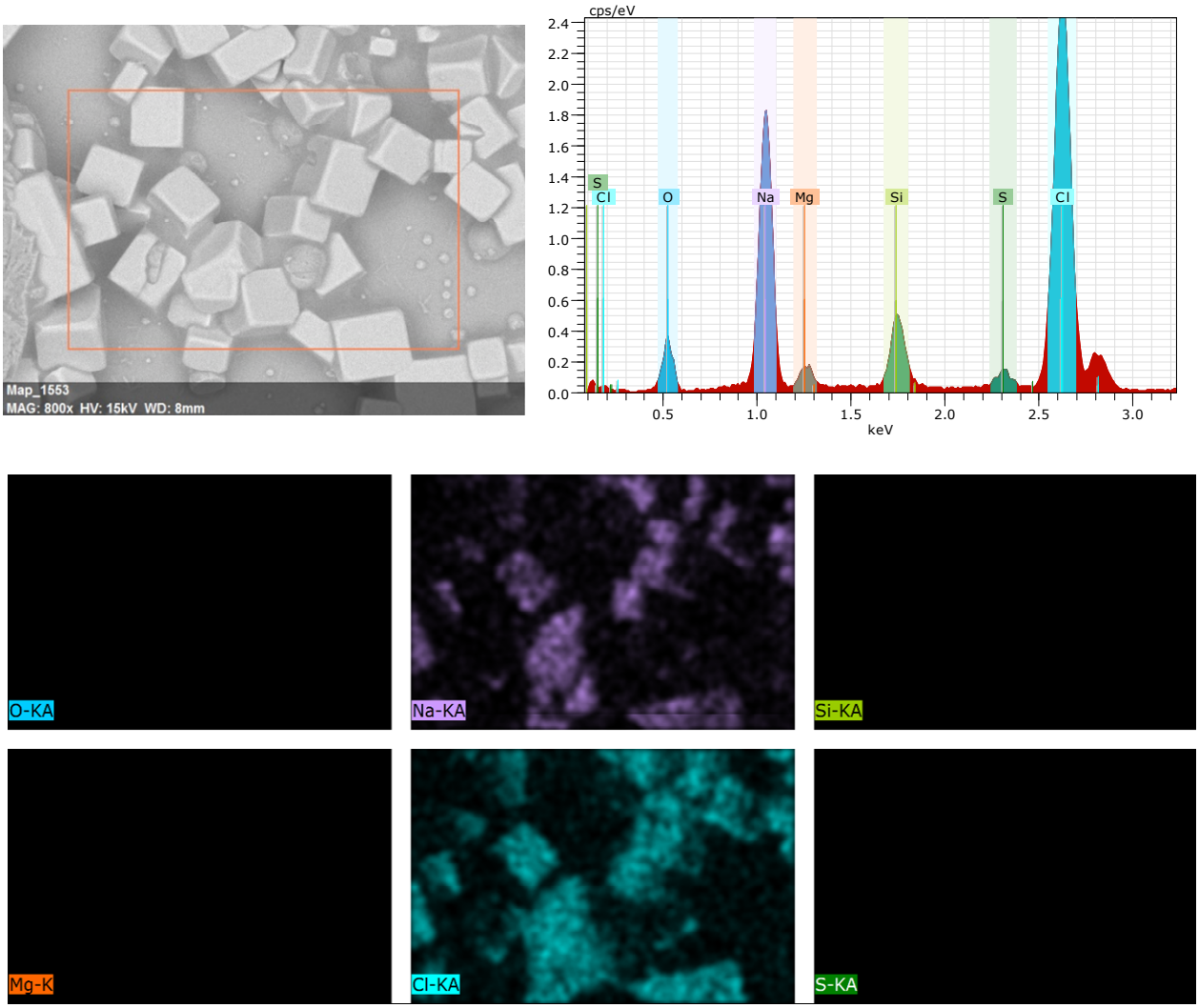

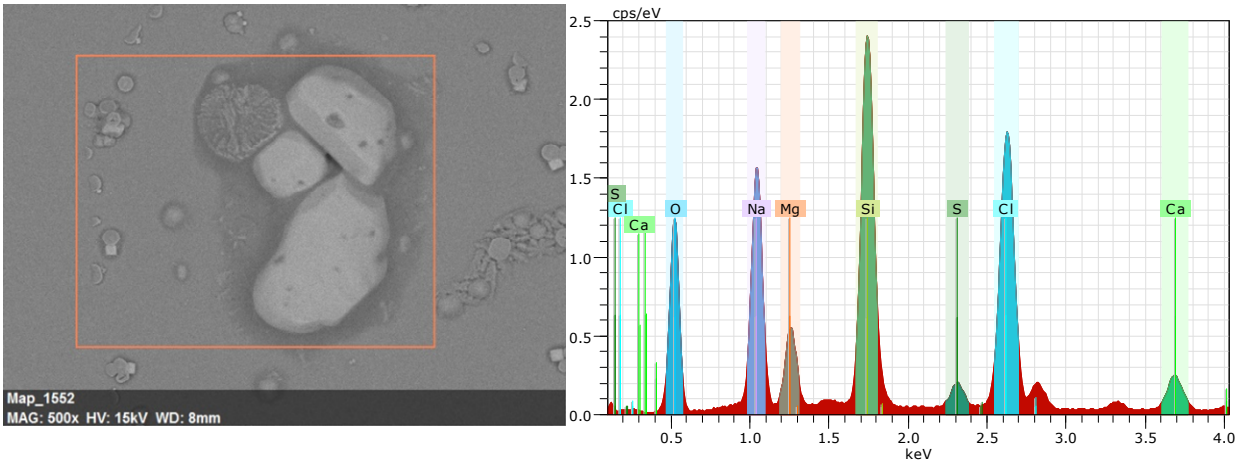
Map_1552
MAG: 500x HV: 15kV WD: 8mm
cps/eV
2.5
2.0
1.5
1.0
0.5
0.0
S
Cl
Ca
O
Na
Mg
Si
S
Cl
Ca
0.5
1.0
1.5
2.0
2.5
3.0
3.5
4.0
keV

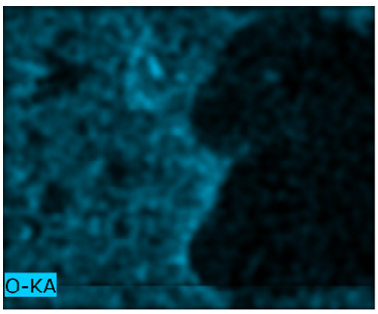
O-KA

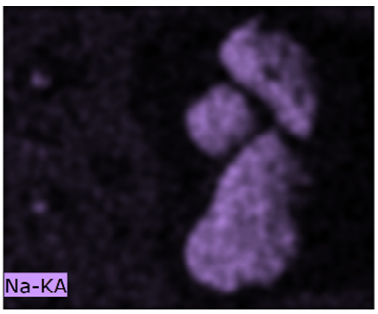
Na-KA

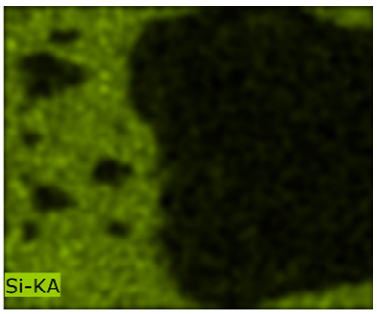
Si-KA

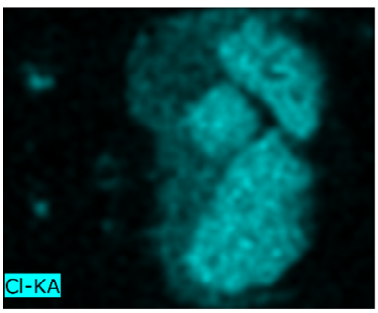
Cl-KA

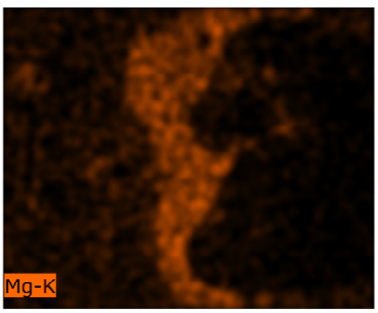
Mg-K

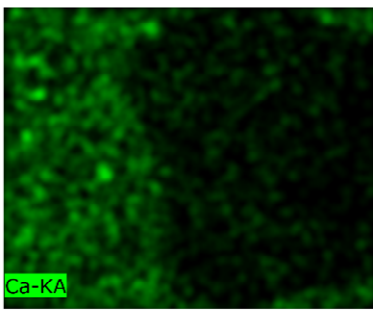
Ca-KA

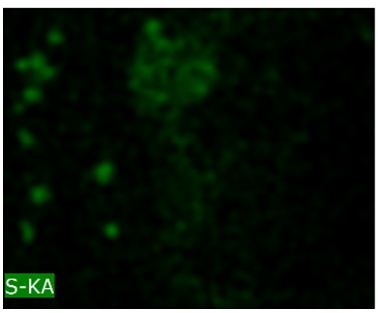
S-KA

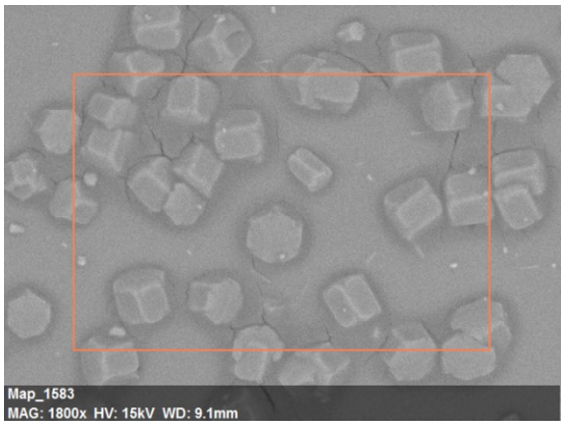
Map_1583
MAG: 1800x HV: 15kV WD: 9.1mm

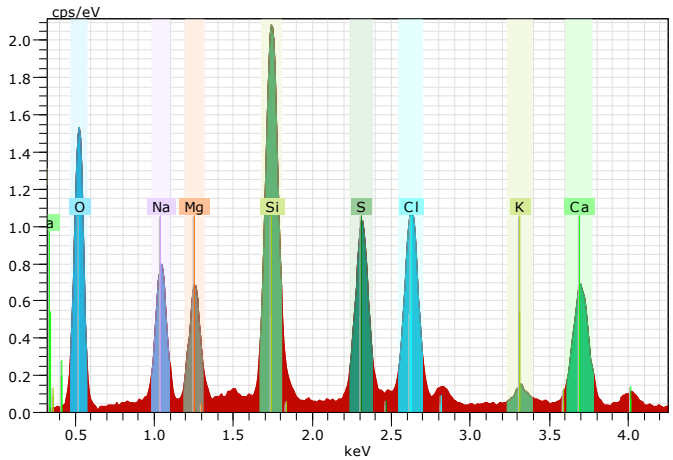
cps/eV
2.0
1.8
1.6
1.4
1.2
1.0
0.8
0.6
0.4
0.2
0.0
O
Na
Mg
Si
S
Cl
K
Ca
0.5
1.0
1.5
2.0
2.5
3.0
3.5
4.0
keV

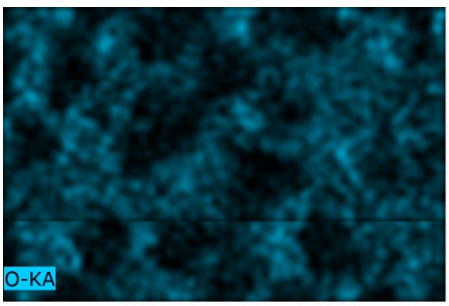
O-KA

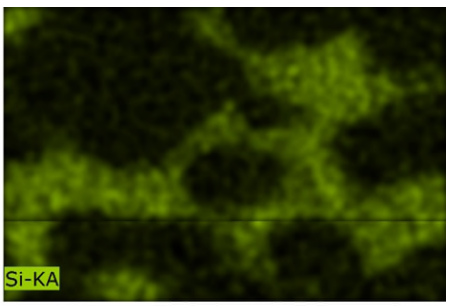
Si-KA

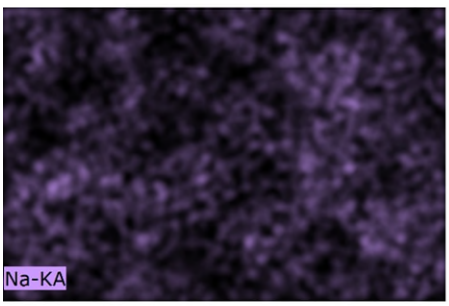
Na-KA

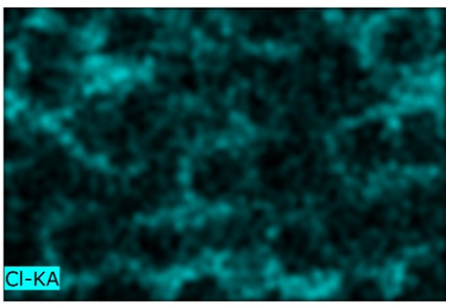
Cl-KA

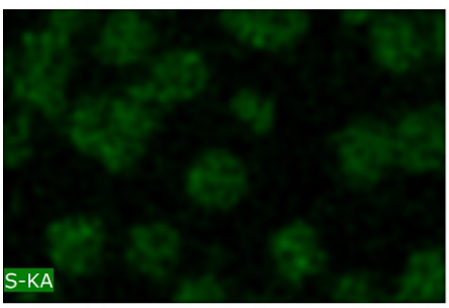
S-KA

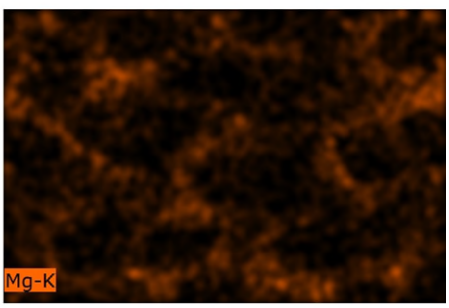
Mg-K

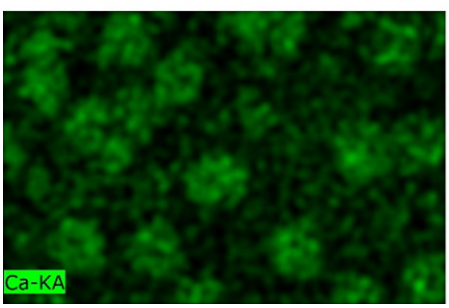
Ca-KA

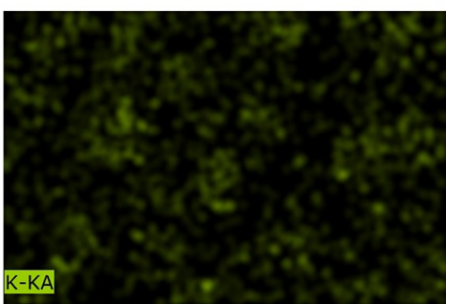
K-KA

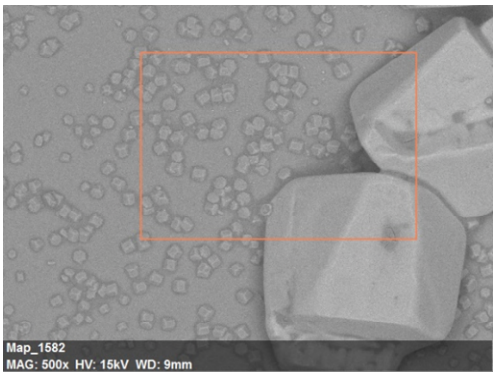
Map_1582
MAG: 500x HV: 15kV WD: 9mm

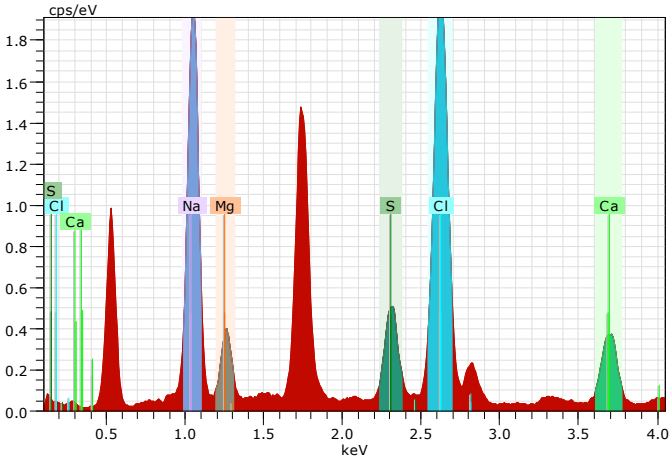
cps/eV
1.8
1.6
1.4
1.2
1.0
0.8
0.6
0.4
0.2
0.0
S
Cl
Ca
Na
Mg
S
Cl
Ca
0.5
1.0
1.5
2.0
2.5
3.0
3.5
4.0
keV

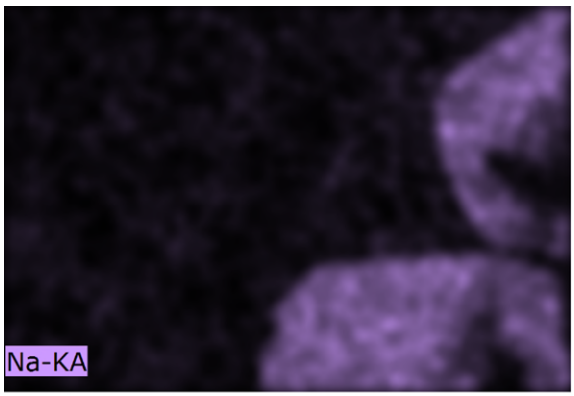
Na-KA

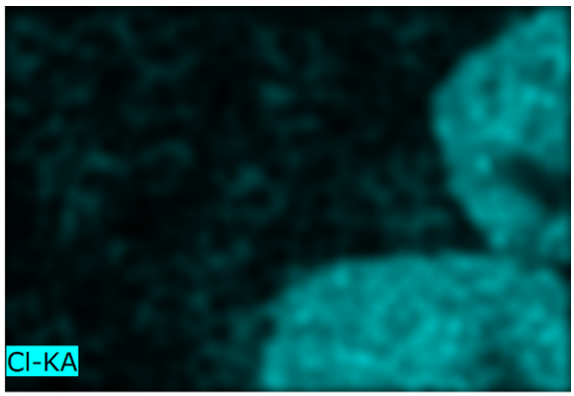
Cl-KA

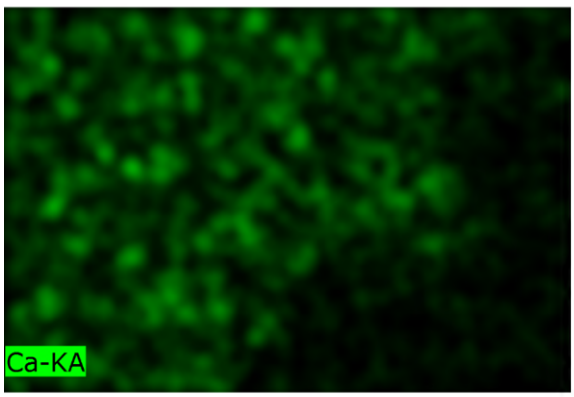
Ca-KA

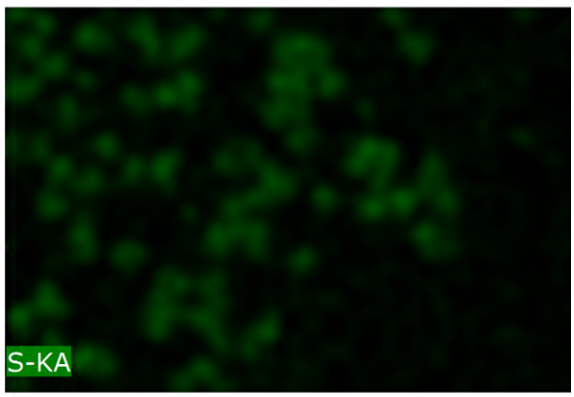
S-KA

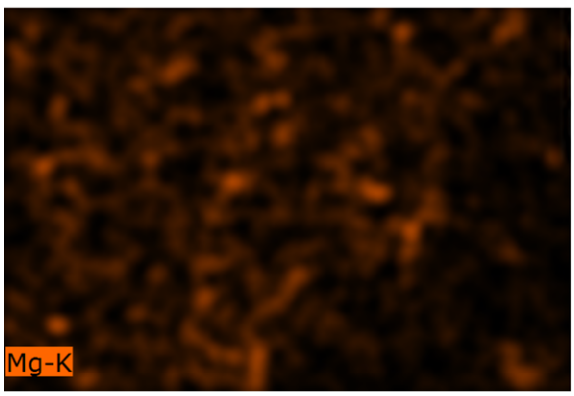
Mg-K

8.9.2 EDS analysis of hydrophobic surfaces after seawater exposure

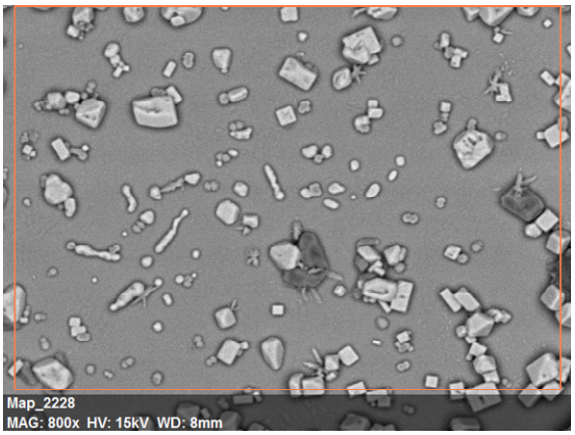

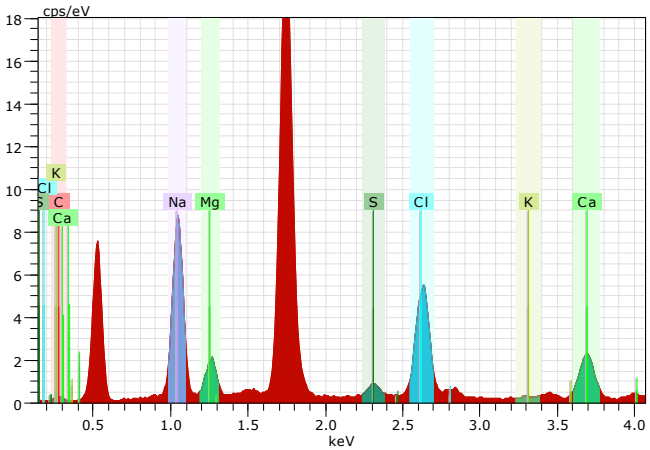

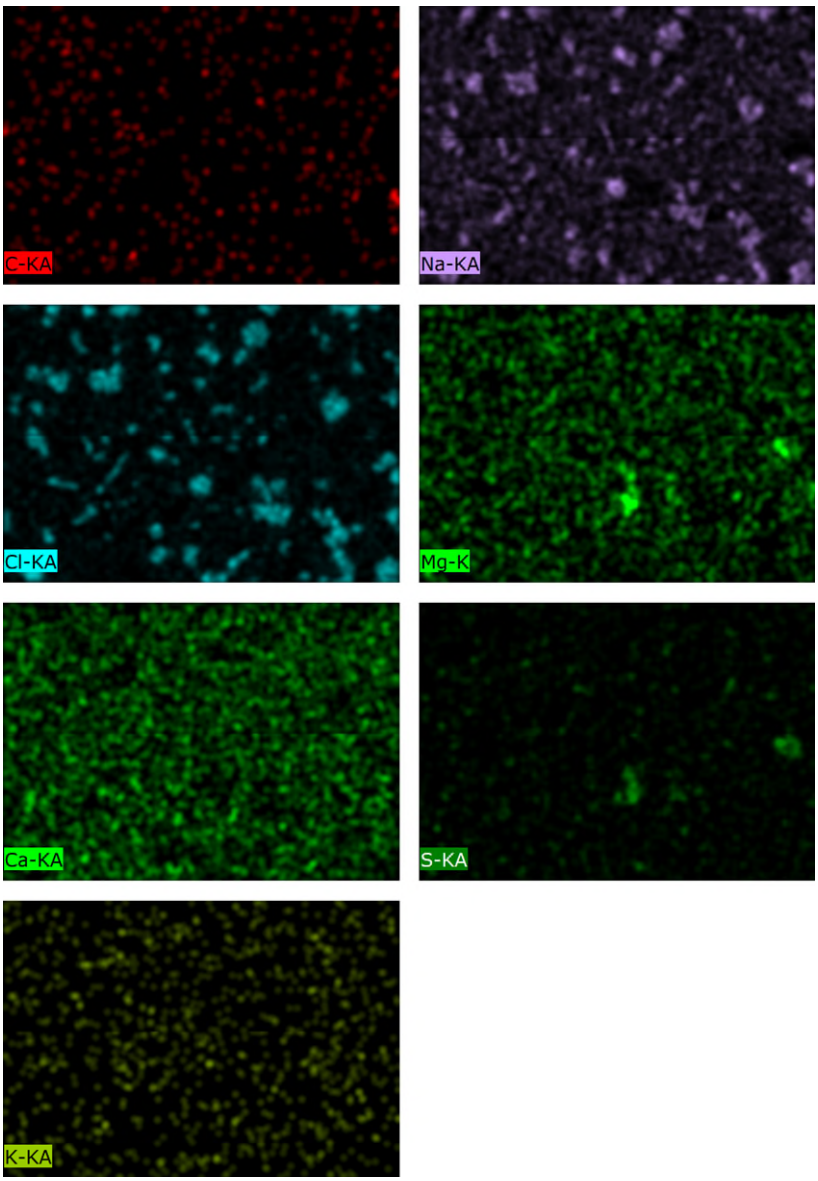

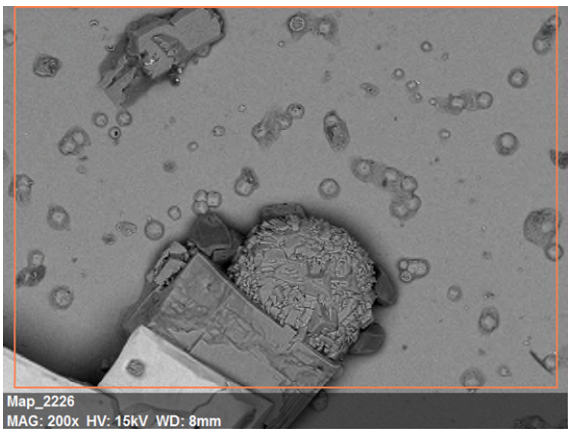
Map_2226
MAG: 200x HV: 15kV WD: 8mm

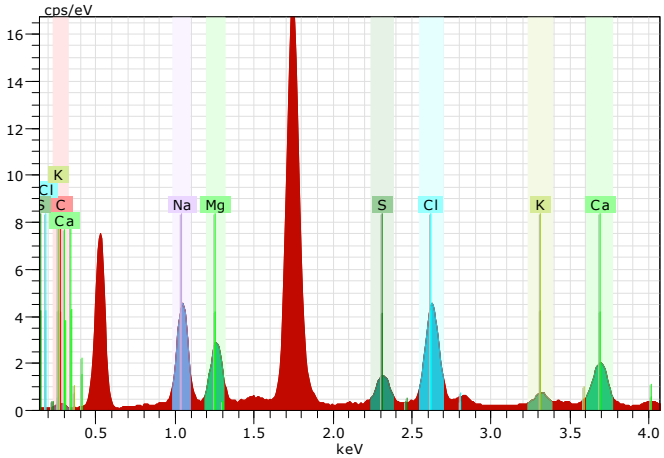
cps/eV
16
14
12
10
8
6
4
2
0
K
Cl
S
C
Ca
Na
Mg
S
Cl
K
Ca
0.5
1.0
1.5
2.0
2.5
3.0
3.5
4.0
keV

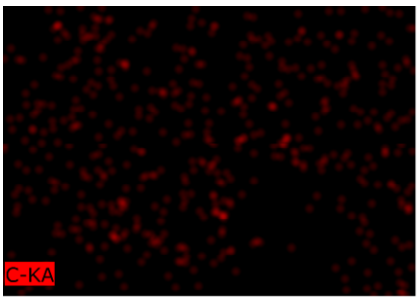
C-KA

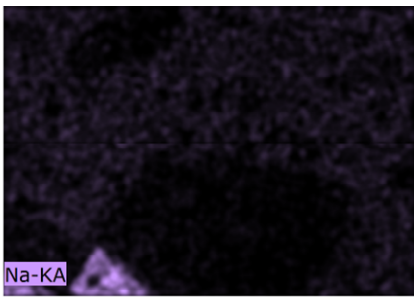
Na-KA

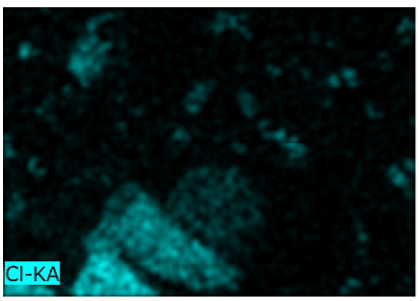
Cl-KA

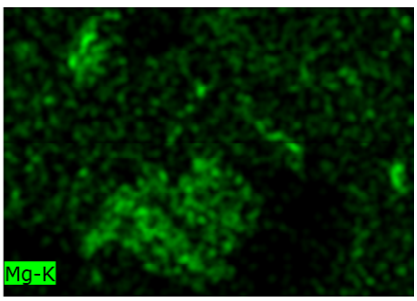
Mg-K

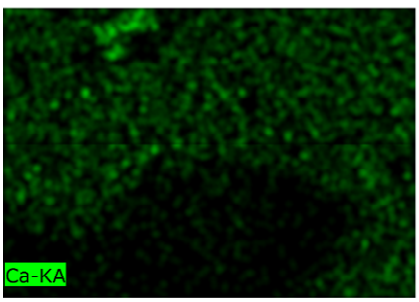
Ca-KA

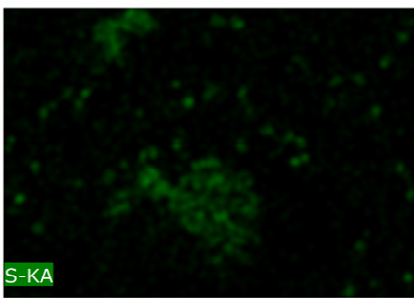
S-KA

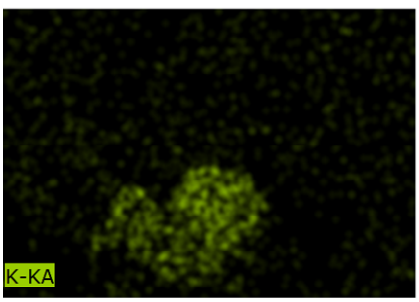
K-KA

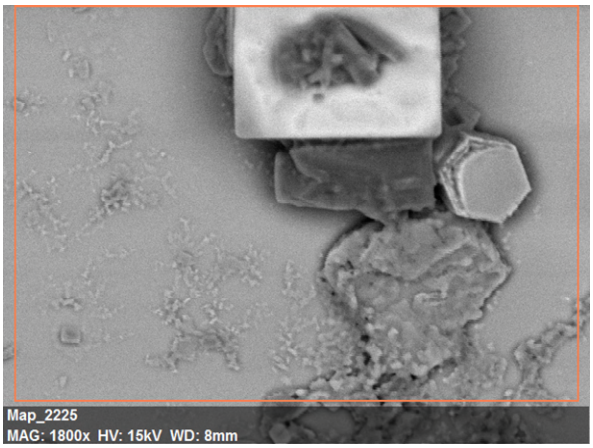
Map_2225
MAG: 1800x HV: 15kV WD: 8mm

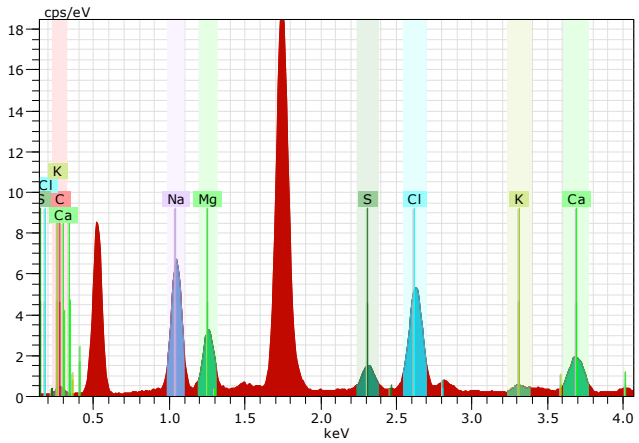
cps/eV
18
16
14
12
10
8
6
4
2
0
K
Cl
S
C
Ca
Na
Mg
S
Cl
K
Ca
0.5
1.0
1.5
2.0
2.5
3.0
3.5
4.0
keV

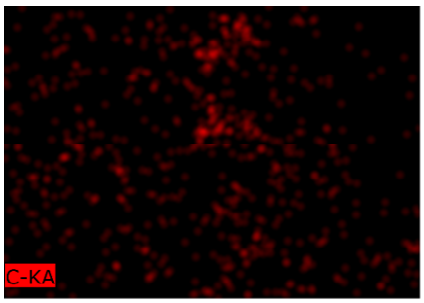
C-KA

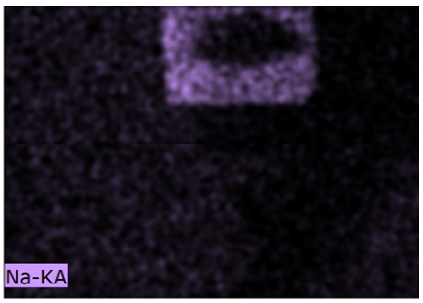
Na-KA

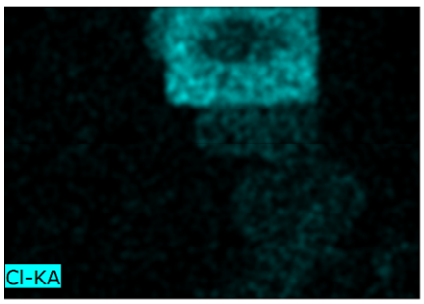
Cl-KA

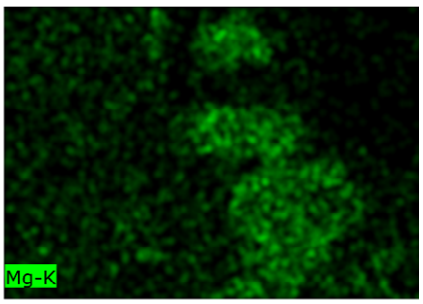
Mg-K

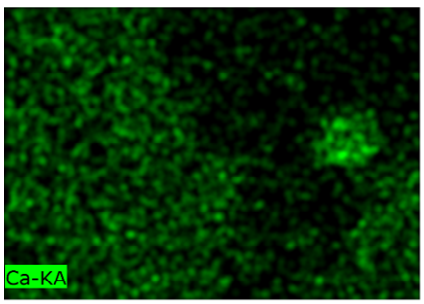
Ca-KA

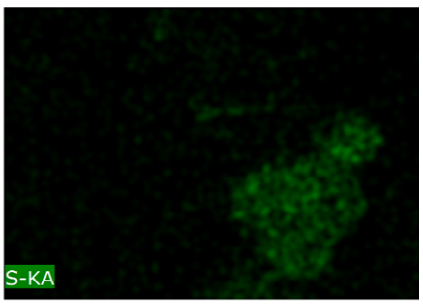
S-KA

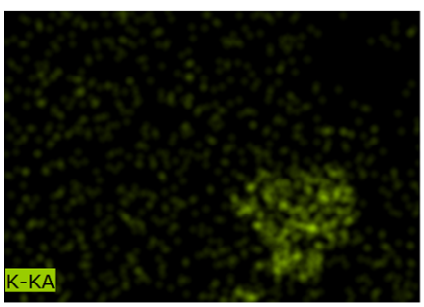
K-KA

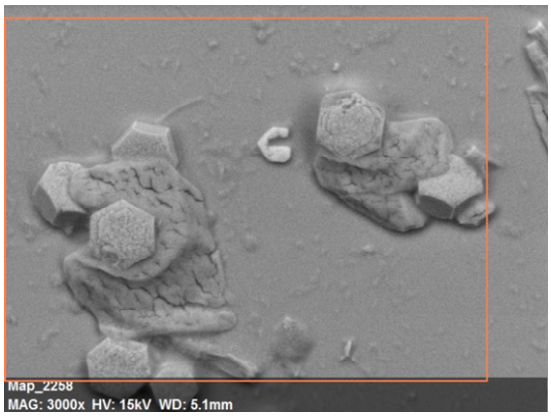
Map_2258
MAG: 3000x HV: 15kV WD: 5.1mm

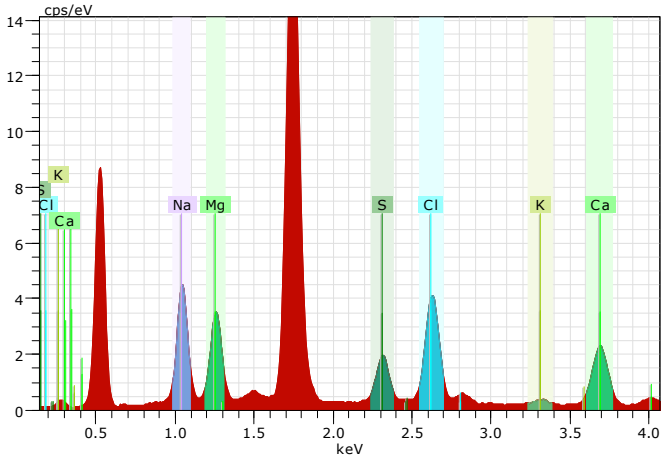
cps/eV
14
12
10
8
6
4
2
0
K
S
Cl
Ca
Na
Mg
S
Cl
K
Ca
0.5
1.0
1.5
2.0
2.5
3.0
3.5
4.0
keV

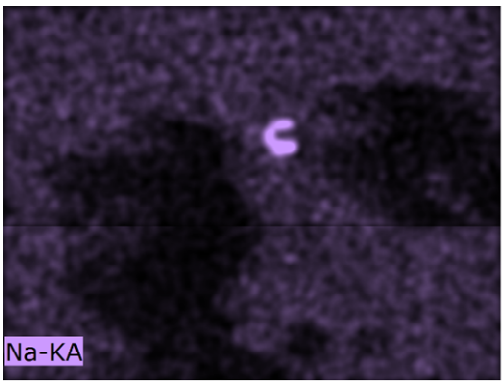
Na-KA

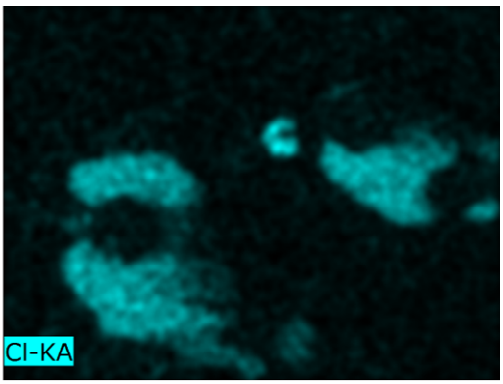
Cl-KA

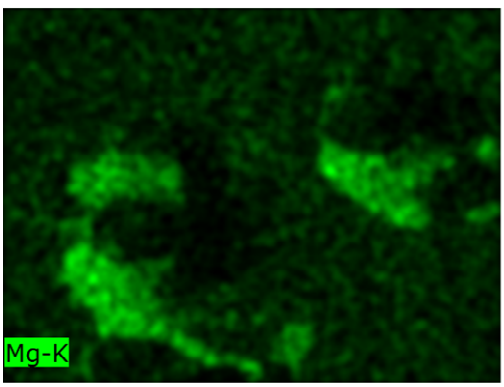
Mg-K

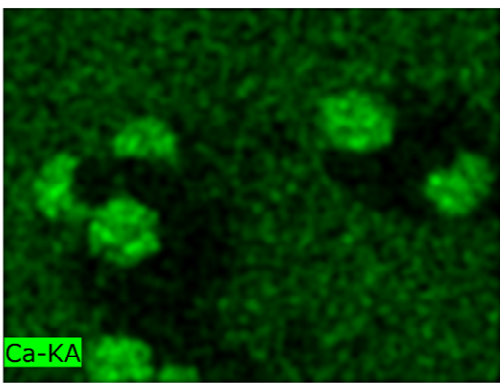
Ca-KA

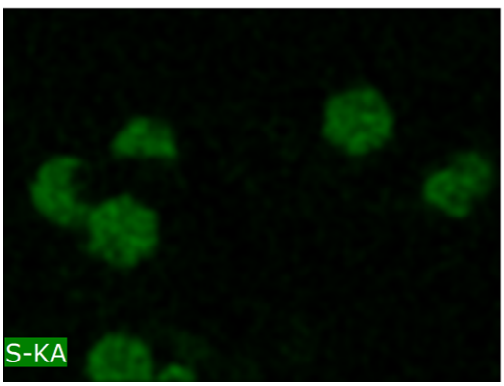
S-KA

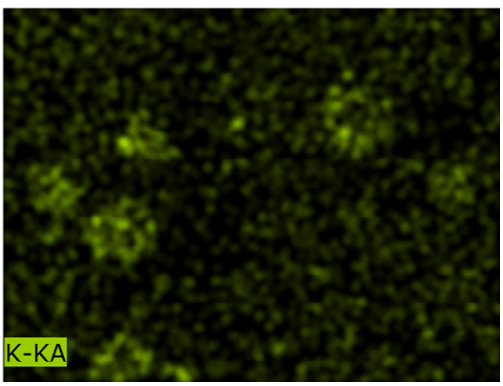
K-KA

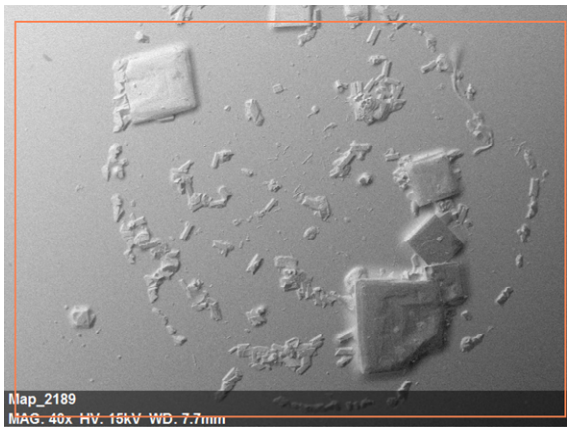
Map_2189
MAG: 40x HV: 15kV WD: 7.7mm

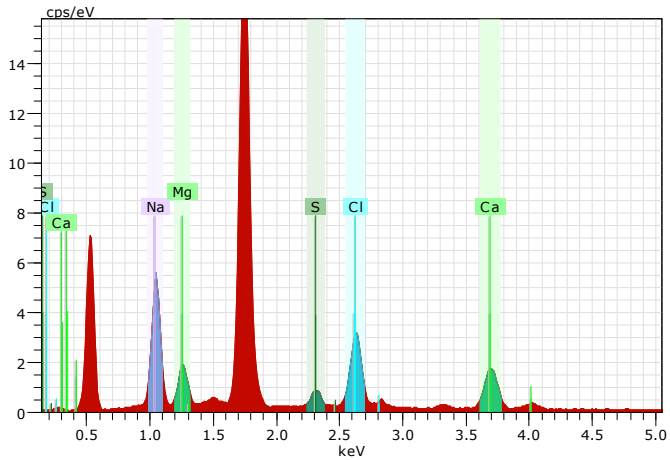
cps/eV
14
12
10
8
6
4
2
0
Cl
Ca
Na
Mg
S
Cl
Ca
0.5
1.0
1.5
2.0
2.5
3.0
3.5
4.0
4.5
5.0
keV

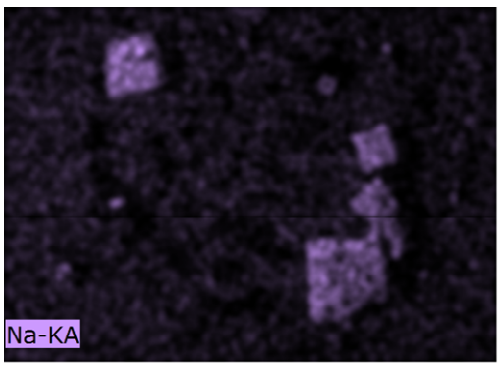
Na-KA

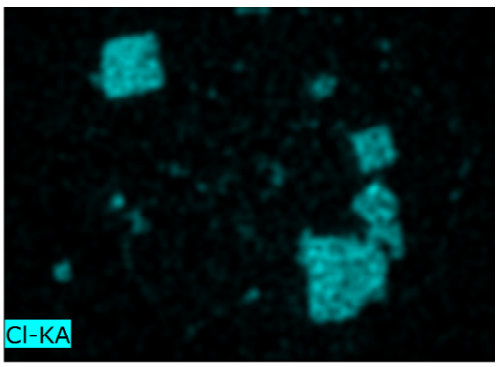
Cl-KA

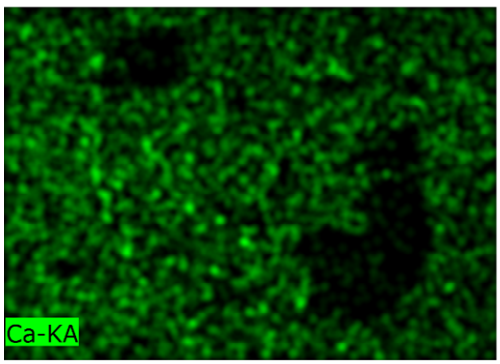
Ca-KA

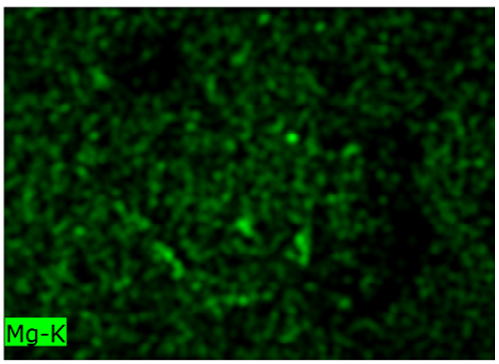
Mg-K

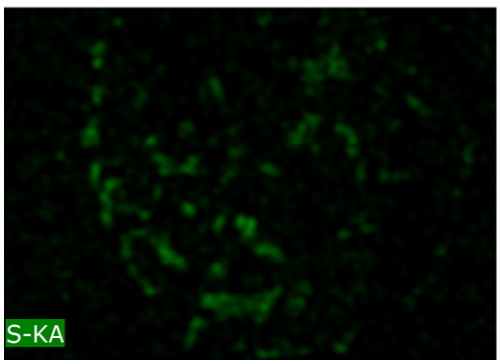
S-KA


Map_2229
MAG: 800x HV: 15kV WD: 8mm

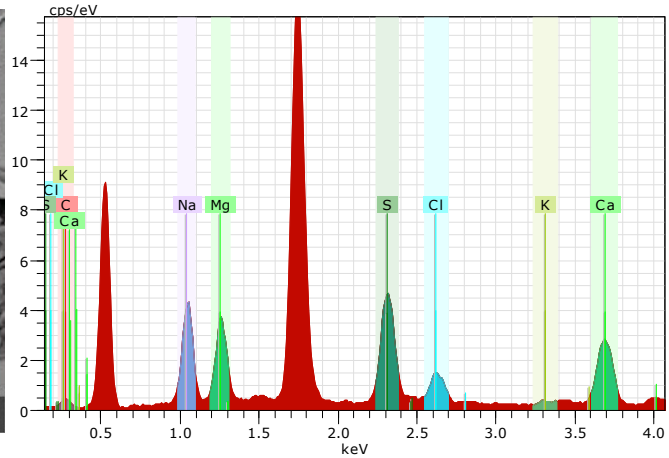
cps/eV
14
12
10
8
6
4
2
0
K
Cl
S
C
Ca
Na
Mg
S
Cl
K
Ca
0.5
1.0
1.5
2.0
2.5
3.0
3.5
4.0
keV

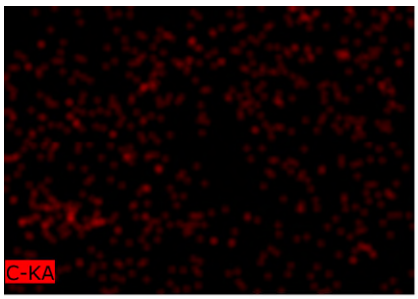
C-KA

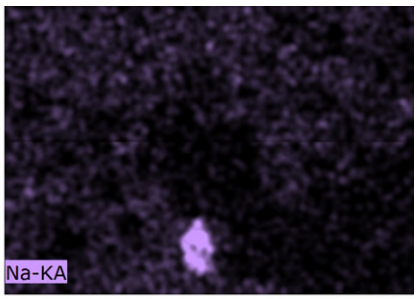
Na-KA

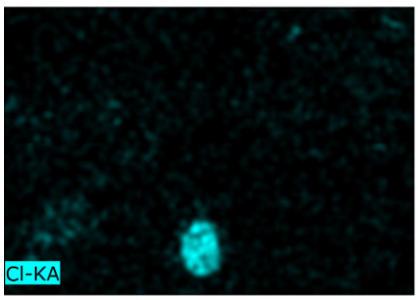
Cl-KA

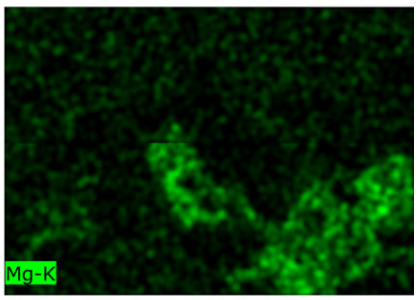
Mg-K

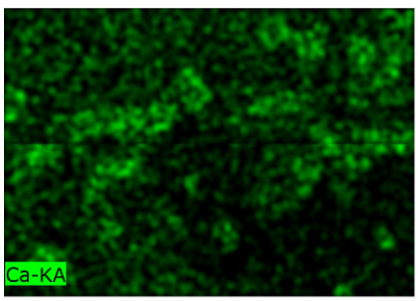
Ca-KA

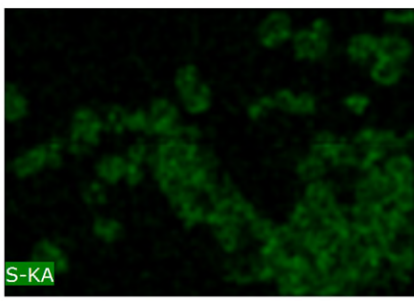
S-KA

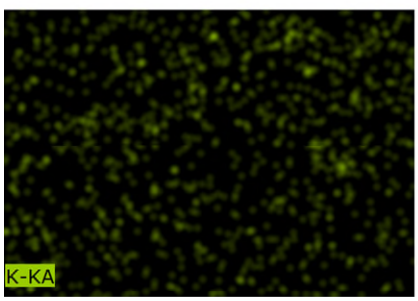
K-KA


Map_2202
MAG. 600x HV. 15kV WD. 8mm

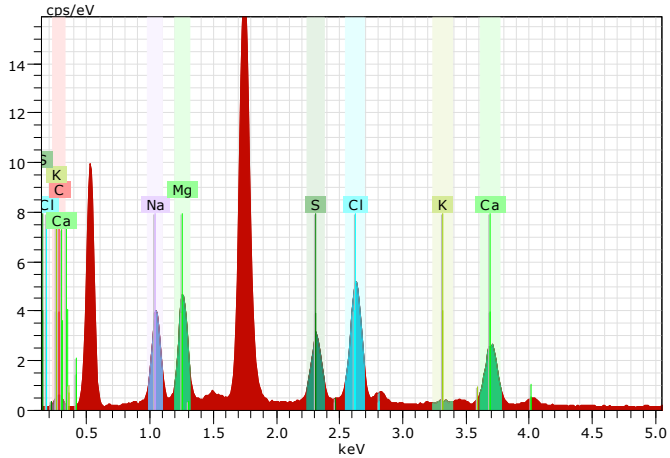
cps/eV
14
12
10
8
6
4
2
0
K
C
Cl
Ca
Na
Mg
S
Cl
K
Ca
0.5
1.0
1.5
2.0
2.5
3.0
3.5
4.0
4.5
5.0
keV

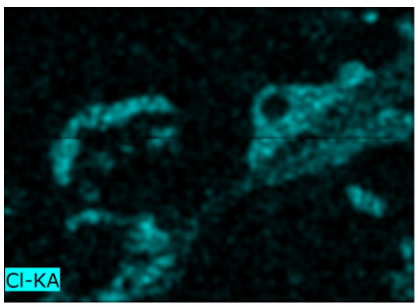
Cl-KA

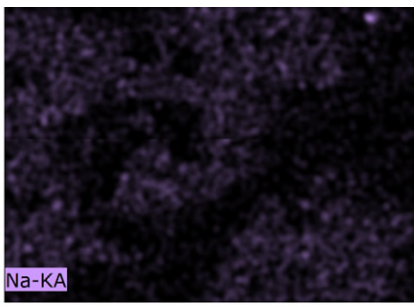
Na-KA

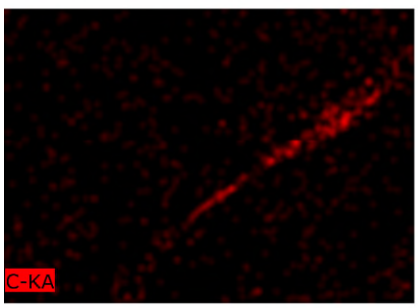
C-KA

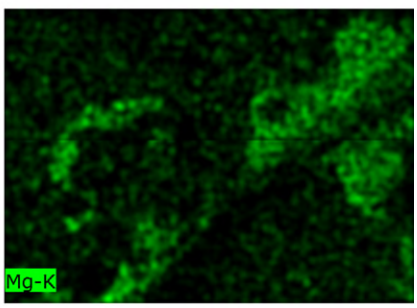
Mg-K

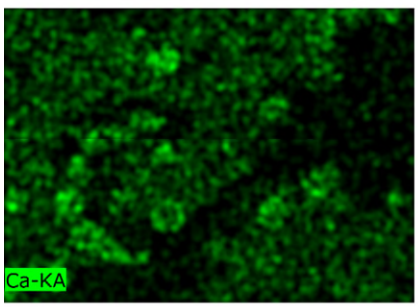
Ca-KA

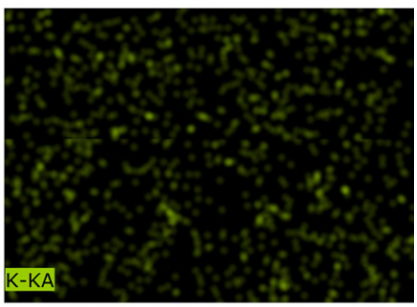
K-KA

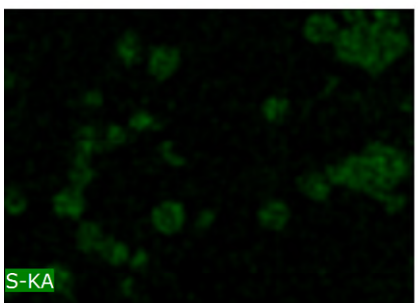
S-KA

8.9.3 EDS analysis of hydrophobic coatings after seawater exposure and thoroughly rinsing with de-ionized water

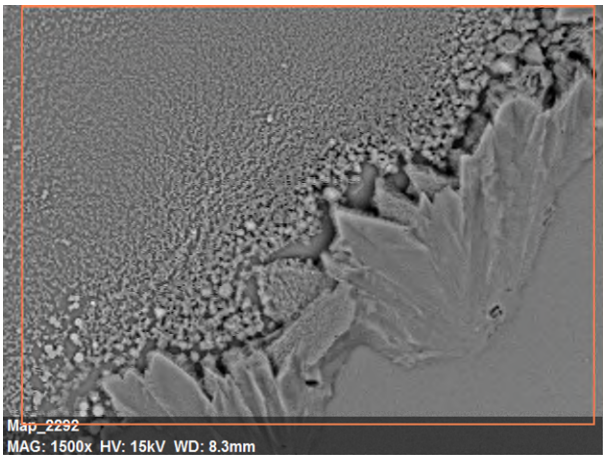

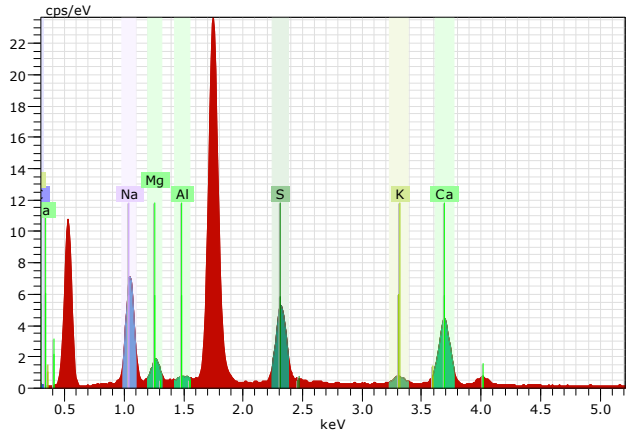

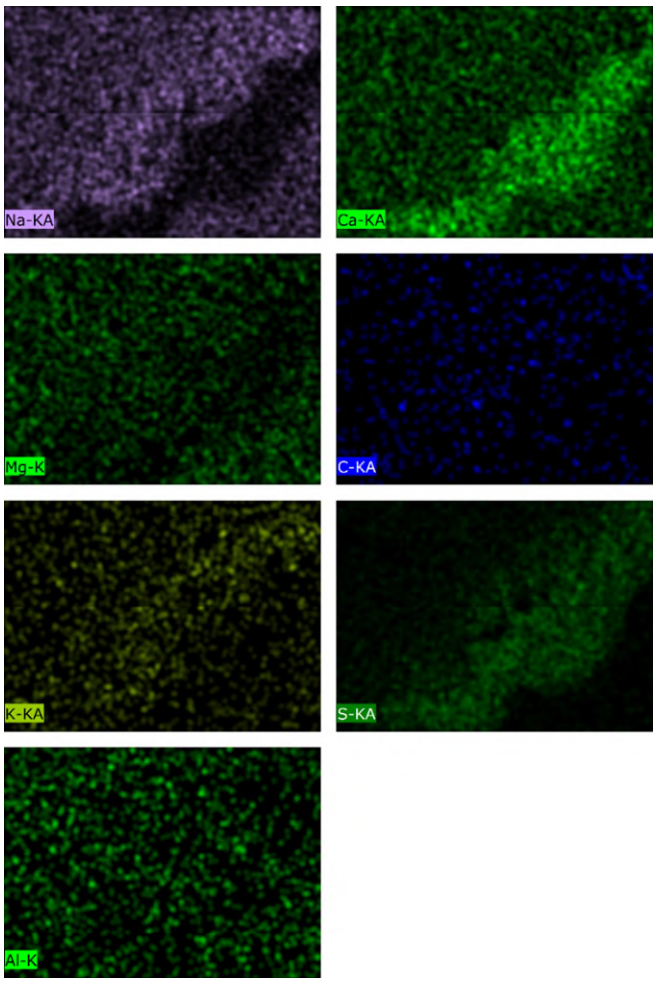

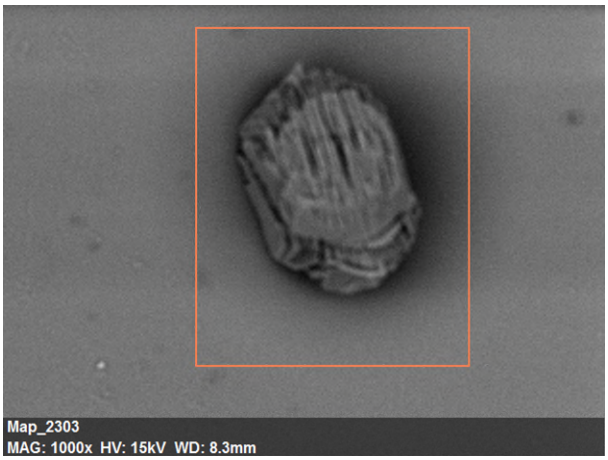
Map_2303
MAG: 1000x HV: 15kV WD: 8.3mm

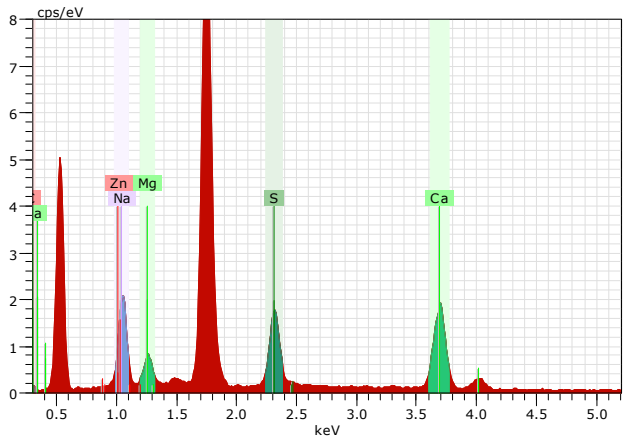
cps/eV
Zn
Mg
Na
S
Ca
keV

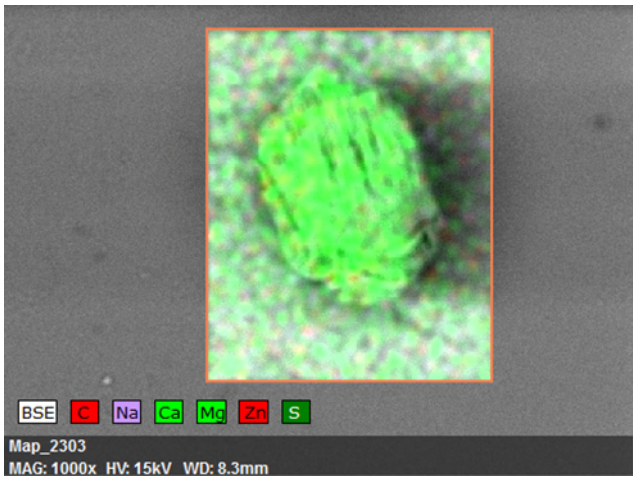
BSE
C
Na
Ca
Mg
Zn
S
Map_2303
MAG: 1000x HV: 15kV WD: 8.3mm

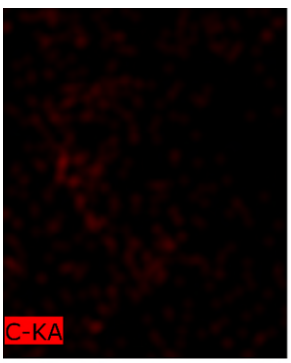
C-KA

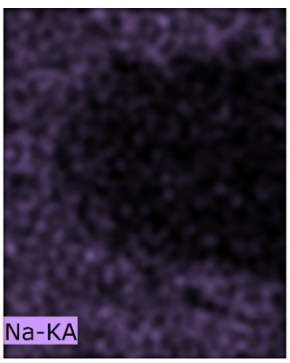
Na-KA

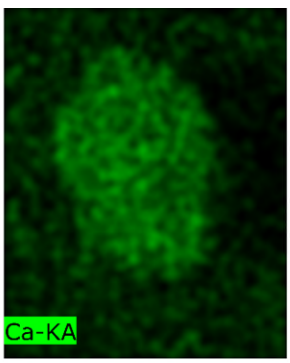
Ca-KA

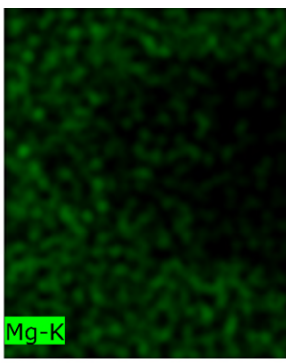
Mg-K

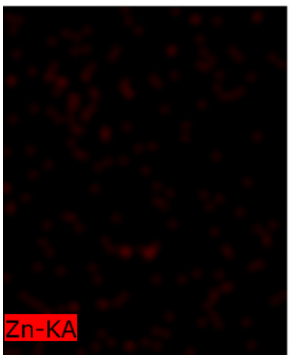
Zn-KA

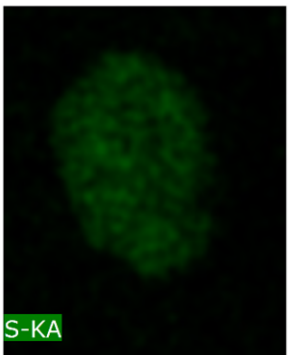
S-KA

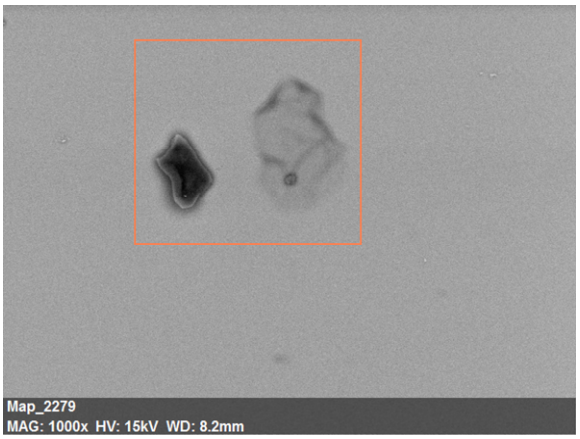
Map_2279
MAG: 1000x HV: 15kV WD: 8.2mm

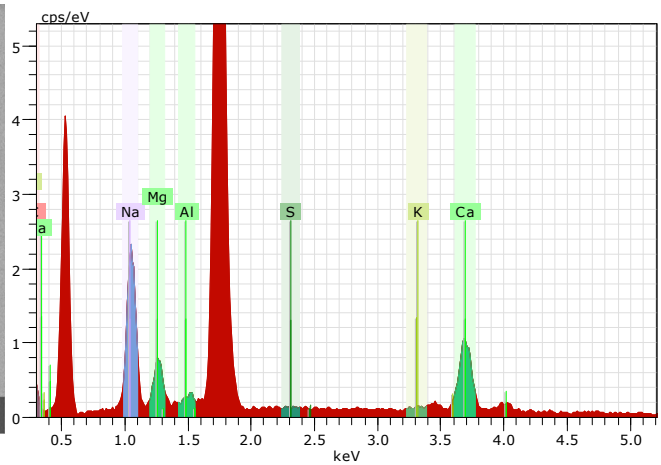
cps/eV
5
4
3
2
1
0
a
Na
Mg
Al
S
K
Ca
0.5
1.0
1.5
2.0
2.5
3.0
3.5
4.0
4.5
5.0
keV

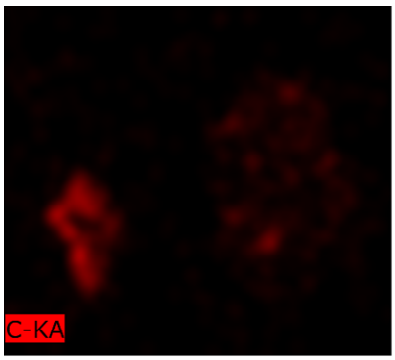
C-KA

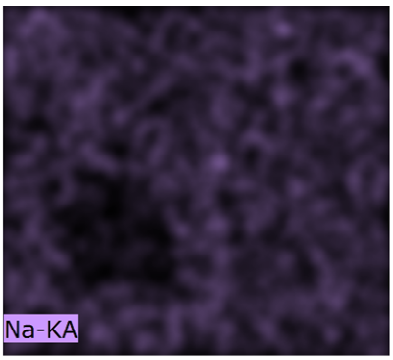
Na-KA

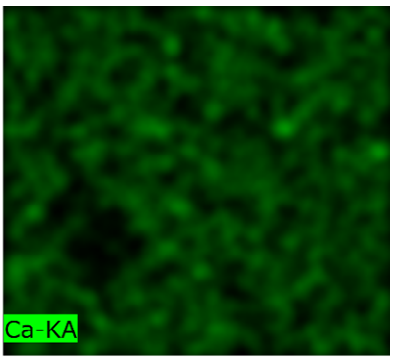
Ca-KA

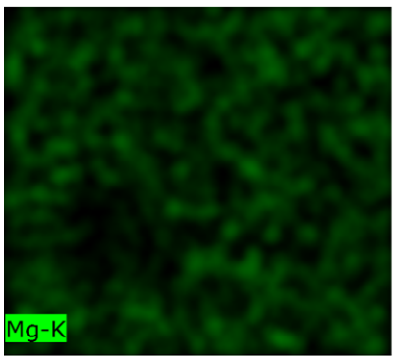
Mg-K

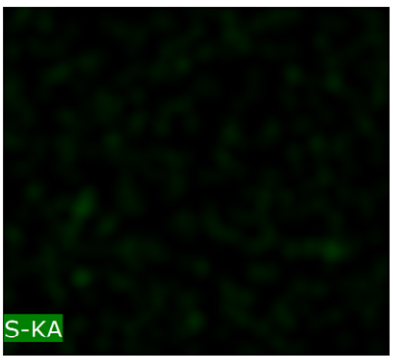
S-KA

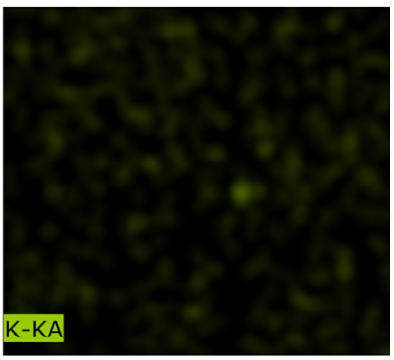
K-KA

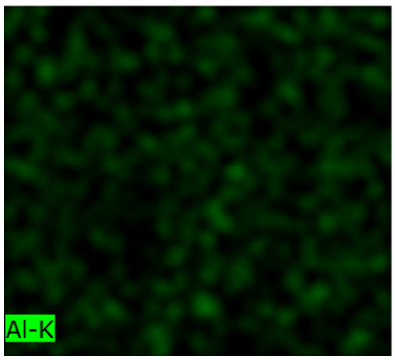
Al-K

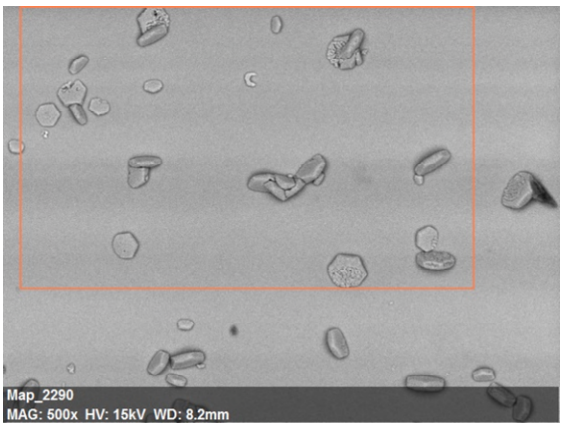
Map_2290
MAG: 500x HV: 15kV WD: 8.2mm

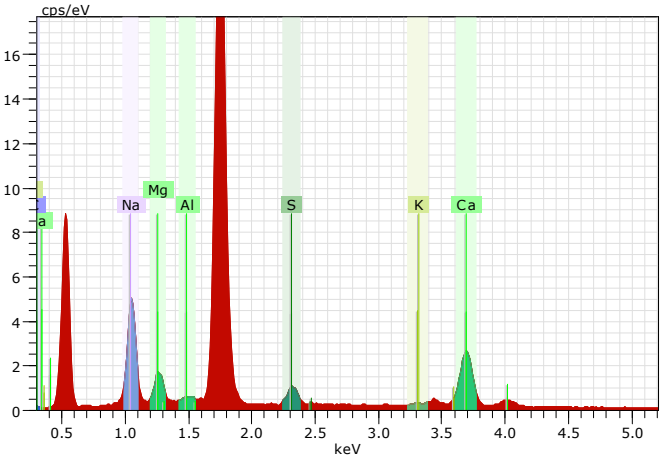
cps/eV
16
14
12
10
8
6
4
2
0
a
Na
Mg
Al
S
K
Ca
0.5
1.0
1.5
2.0
2.5
3.0
3.5
4.0
4.5
5.0
keV

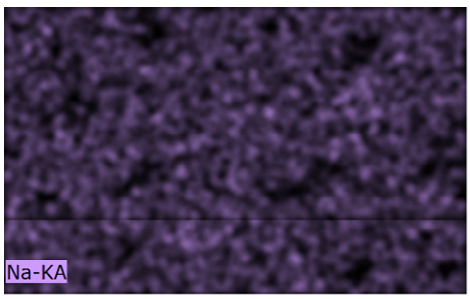
Na-KA

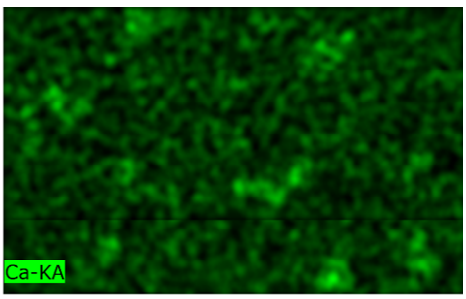
Ca-KA

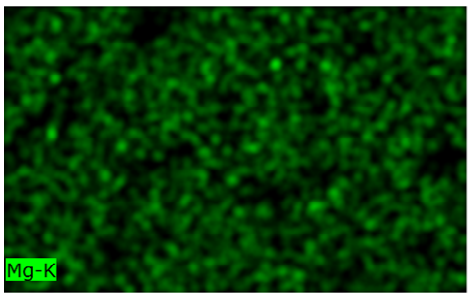
Mg-K

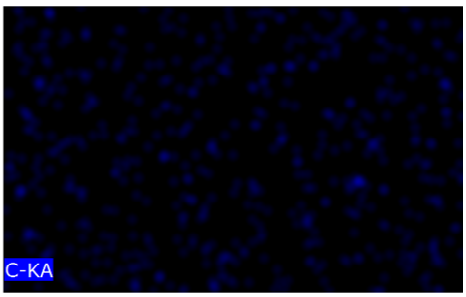
C-KA

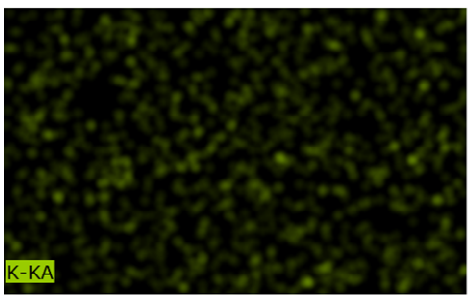
K-KA

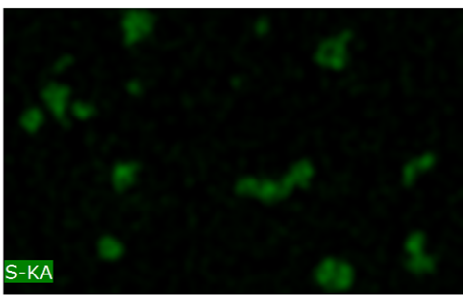
S-KA

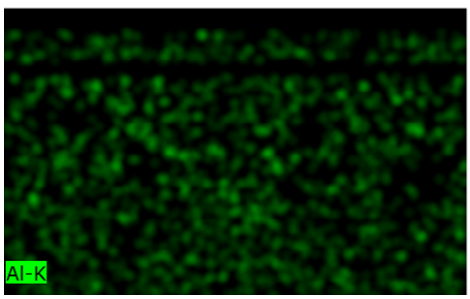
Al-K

8.10 Test box

In an early phase of this study a test box was designed, constructed and programmed (Figure 8.7 and 8.8). Unfortunately, it was never used due to unforeseen events as abrupt stock moving and internal lock down (Covid-19). The goal of the test box was to simulate somewhat similar conditions to which the PV panels will be exposed to in the marine environment. To do so, it was equipped with a seawater diffuser, a LED-lamp and a fan. Shell is made from 30mm plexiglass, reused from an aquarium used for lice research. All equipment is controlled to best simulate the actual conditions, done by a RaspberryPi with Python master code.

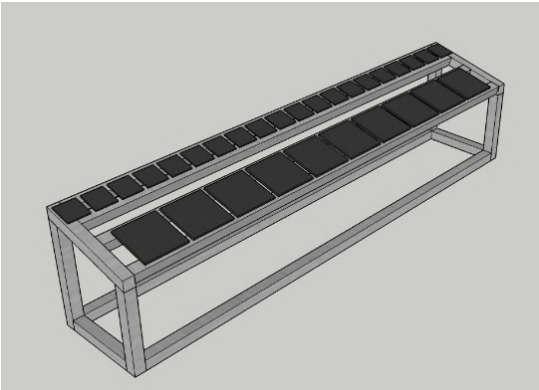

Figure 8.7: A sketch of sample rack for the test box. Made in aluminum with a 15 degrees inclination.

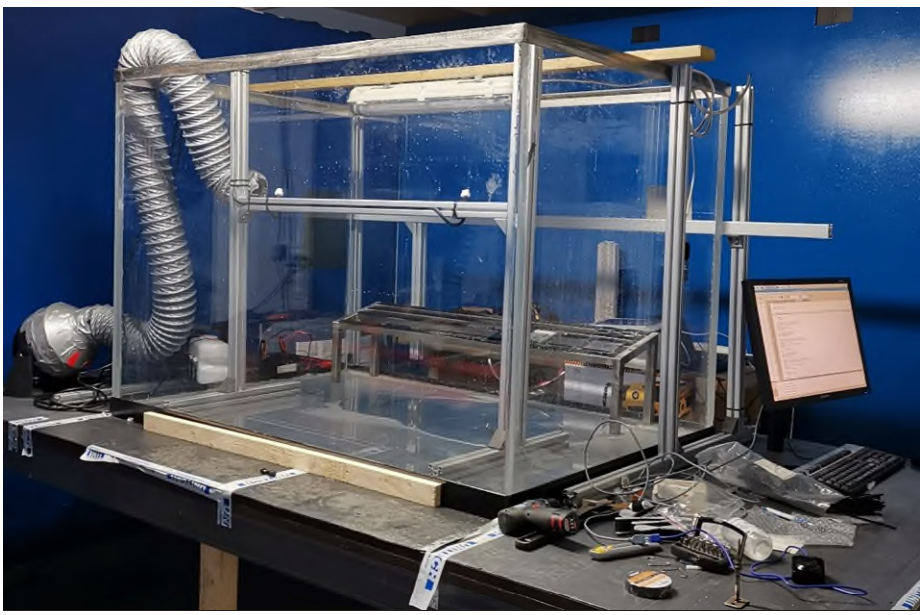

Figure 8.8: Custom-made test box, made for exposure experiments of seawater. Was not used due to external circumstances.